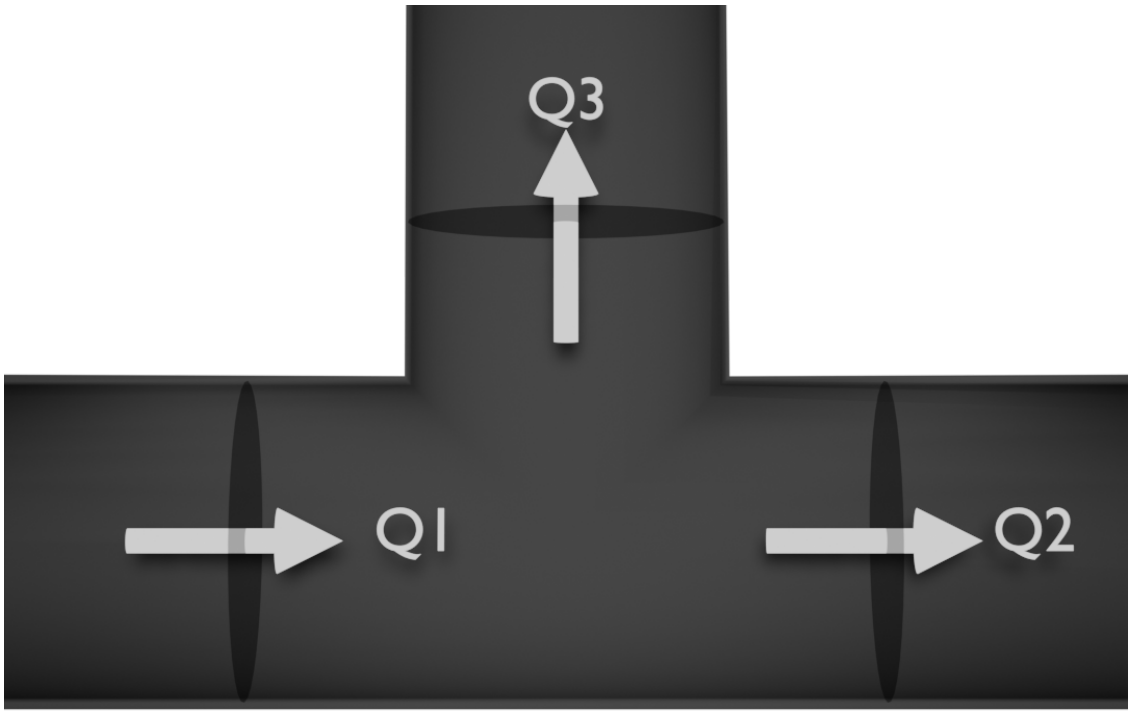

Complex Ventilation of Multiple Electrical Enclosure Systems

Development and comparision of 1D pipe-flow models

Master's thesis in Engineering mathematics and computational science

CARL ANDERSSON

DEPARTMENT OF MATHEMATICAL SCIENCES

CHALMERS UNIVERSITY OF TECHNOLOGY
Gothenburg, Sweden 2022
www.chalmers.se

Master's thesis 2022

Complex Ventilation of Multiple Electrical Enclosure Systems

Development and comparision of 1D pipe-flow models

Carl Andersson

CHALMERS
UNIVERSITY OF TECHNOLOGY

Department of Mathematical Sciences
Chalmers University of Technology
Gothenburg, Sweden 2022

Complex Ventilation of Multiple Electrical Enclosure Systems
Development and comparision of 1D pipe-flow models
Carl Andersson

Supervisor: Ulf Sand, Hitachi Energy, Hitachi Energy Research
Examiner: Lars Davidson, Department of Fluid Dynamics

Master's Thesis 2022
Department of Mathematical Sciences
Chalmers University of Technology
SE-412 96 Gothenburg

Cover: Illustrative image of flows through a t-junction, reused in figure in in figure 2.1

Typeset in LaTeX
Printed by Chalmers Reproservice
Gothenburg, Sweden 2022

Complex Ventilation of Multiple Electrical Enclosure systems
Development and comparision of 1D Pipe-flow models
CARL ANDERSSON
Department of Mathematical Sciences
Chalmers University of Technology

Abstract

The nature of fluid flows in pipes is highly relevant to planning and constructing cooling systems. Although general, conventional computational fluid dynamics solutions such as ANSYS FLUENT, OpenFOAM or similar software exists, these solutions are computationally expensive and require hours, if not days, to give results. This study aims to explore and compare implicit solutions for complex pipe networks that can be generated in a much quicker fashion. In this context, implicit solutions refer to 1D-implementations which solve the entire pipe network as a set of simultaneous equations, or in other words, a matrix.

In order to evaluate the accuracy of any such implicit solver, the results that the solver produces are validated against a simulation run in ANSYS FLUENT using, to the extent that it is possible, identical settings. A set of different cases are run through this validation procedure in order to observe how the implicit flow rate solver compares across a number of cases. The results show that while the implicit flow rate solver manages to mimic the fluid flow of the ANSYS FLUENT simulations with only small errors that arise primarily from observed asymmetries in the ANSYS FLUENT simulation. The implicit flow rate solver does however produce significant errors in temperature prediction when cooling systems that have heat sources approximating $2 \cdot 10^5$ W/m^3 applied at smaller regions. Additionally, the results show an extreme benefit in terms of run-time, on the order of 10^3 compared to ANSYS FLUENT.

These results suggest that the implicit solver fails to capture a variety of phenomena, particularly related to cases applying larger additional heat sources. These phenomena would need to be captured if it is to act as a predictor of the behavior of such cases. For cases without the previously mentioned large heat source however, the results suggest that the implicit solver can serve as a semi-accurate run-time efficient predictor. Additionally, the results suggest that the usage of minor loss coefficients or length-equivalents for estimating the pressure drop over a pipe bend, T-junction or similar structures is insufficient to capture combined effects of said structures in more complex pipe networks. Finally, observation of the errors in temperature prediction suggest an approximately linear behavior. On this basis, the implicit solver or a variant of it could very well serve as an early predictor when iterating through system design in order to quickly find designs that will fail to fulfill certain criteria.

Keywords: CFD, Pipe flow, fluid dynamics, ventilation, MATLAB, ANSYS FLUENT

Acknowledgements

I would first like to thank my supervisor, Ulf Sand at Hitachi Energy, Hitatchi Energy Research. He has been available whenever there has been a lack of clarity and direction in my work, my research and my writing. He has consistently served as a guide when I needed one, while letting this paper to be my own work in entirety.

I would also like to acknowledge Lars Davidson of the department of fluid dynamics at Chalmers University of Technology as the second reader of this thesis.

Finally, I wish to express my gratitude to my parents for continued support, encouragement and occasional spur throughout the process of writing this thesis as well as during my years of study leading up to it. This thesis would not have been possible without them.

Thank you.

Carl Andersson, Västerås, 09 2021

Nomenclature

Below is the nomenclature of indices, sets, parameters, and variables that have been used throughout this thesis.

Sets

Set symbol	**Set Descriptor**	**Set element symbol**
$\mathcal{N}$	Set of nodes	n
$\mathcal{C}$	Set of connections between nodes	c
$\mathcal{P}$	Set of paths	p
$\mathcal{D}$	Set of path differentials	δp

Parameters

Parameter symbol	**Parameter descriptor**	**Parameter unit**
ρ	Density	$\frac{kg}{m^3}$
t	Time	s
Δt	Size of time-step	s
$\mathbf{u}$	Velocity vector field	$\frac{m}{s}$
V	Volume	m^3
S	Surface area of an associated volume V	m^2
A	A discrete surface area	m^2
Q	Volumetric flow rate	$\frac{m^3}{s}$
p	Pressure	$Pa\left(\frac{kg}{ms^2}\right)$
Δp	Pressure drop	Pa
f_D	Darcy Friction Factor	none
L	Length of pipe	m
D	Diameter of pipe	m
K	Minor loss coefficient	none

v	Cross-section average of velocity	$\frac{m}{s}$
g	Gravitational constant	$\frac{m}{s^2}$
δh	Height difference of pipe	m
J_u	Unsteady friction term.	Pa
k_3	Unsteady friction coefficient	none
a	Wave propagation velocity	$\frac{m}{s}$
Re	Reynolds number	none
μ	Dynamic viscosity	Pas
Z	Compressibility	none
h	Specific Enthalpy	$\frac{J}{kg}$
c_p	Specific heat capacity	$\frac{J}{kgK}$
c_v	Specific volumetric heat capacity	$\frac{J}{kgK}$
T	Temperature	K
k	Thermal conductivity	$\frac{W}{mK}$
S_h	Thermal heat source	$\frac{W}{m^3}$
β	Heat interface interpolation factor	none
h_*	Heat transfer coefficient	$\frac{W}{m^2K}$
Nu_L	Nusselt number	none
Pr	Prandtl number	none
Ra_L	Rayleigh number	none
Gr	Grashof number	none

Matrices

Matrix symbol	**Matrix descriptor**	**Matrix size**
A	Adjacency matrix	$\|\mathcal{N}\|x\|\mathcal{N}\|$
F	Flow matrix	$(\|\mathcal{N}\|-1)x\|\mathcal{C}\|$
D	Pressure drop matrix	$(\|\mathcal{C}\|-\|\mathcal{N}\|+1)x\|\mathcal{C}\|$
Θ	Pressure drop coefficient matrix	$(\|\mathcal{C}\|-\|\mathcal{N}\|+1)x\|\mathcal{C}\|$
P	Pressure sum matrix	$\|\mathcal{N}\|x\|\mathcal{C}\|$
H	Heat matrix	$\|\mathcal{N}\|x\|\mathcal{N}\|$

Contents

List of Figures

List of Tables

1
Introduction

The ventilation of high energy systems is of vital importance to maintaining the safe operation of any electric grid, hence modeling and understanding it is an essential part of any project to construct infrastructure for such systems. Although there exists a variety of tools and software to conduct such modeling today, most such software require hours, if not days of dedicated simulation time for each model. As such, it is of great interest to have tools and algorithms that can quickly provide at least an approximate overview of a system or many, such that designs can be iterated over and those that fail to fulfill necessary criteria can quickly be discarded and only those who managed to fulfill said criteria are actually invested with a more full-scale simulation. This paper lays out the construction of a flow rate based solver that aims to do just that, provide quick and approximate solutions to large scale complex piping systems for the air-based ventilation of, among other things, electrical enclosures.

The aim of the flow rate solver is to provide predictions for the air volumetric flow rate, pressure and temperature in both steady and transient conditions. The target of this construction is to find systems that provide even flow division to multiple cooling locations for equal cooling effect. Additionally, a fast run time is considered a vital part of the flow rate solver.

The flow rate solver does not aim to capture local flow field phenomena, such as eddies or in-pipe radial distributions of flow or temperature. The chosen framework for the implementation of the flow rate solver is MATLAB.

2

Theory

In the following sections, the mathematical basis upon which the flow and thermal solver is built is explained.

2.1 Continuity Equation

In order to provide a basis upon which a flow rate solver is built, we start with the continuity equation for fluid dynamics, which in its differential form is listed as follows [13]:

$$\frac{\partial \rho}{\partial t} + \nabla \cdot (\rho \mathbf{u}) = 0 \qquad \left[\frac{kg}{sm^3}\right] \tag{2.1}$$

where ρ is the density field of the fluid in question, t is time and $\mathbf{u}$ is the velocity field. Transforming this into it's integral form over a control volume V yields:

$$\frac{\partial}{\partial t} \iiint\limits_{V} \rho dV + \iiint\limits_{V} \nabla \cdot (\rho \mathbf{u})\, dV = 0 \qquad \left[\frac{kg}{s}\right] \tag{2.2}$$

Gauss theorem [11][12] can then be applied to the second term of the equation, forming the more familiar variant:

$$\frac{\partial}{\partial t} \iiint\limits_{V} \rho dV + \oiint\limits_{S(V)} (\rho \mathbf{u} \cdot \hat{n})\, dS = 0 \qquad \left[\frac{kg}{s}\right] \tag{2.3}$$

where $S(V)$ is the surface of the control volume V. Then, it is assumed that within the confines of the control volume V, the density field ρ is constant inside of the volume, although not necessarily so across the surface of the volume. Leading to the simplified form:

$$\frac{\partial}{\partial t} \rho V + \oiint\limits_{S(V)} (\rho \mathbf{u} \cdot \hat{n})\, dS = 0 \qquad \left[\frac{kg}{s}\right] \tag{2.4}$$

since $\iiint\limits_{V} dV$ is simply V.

Then, the surface S is replaced by a set of discrete surfaces $A = \{A_1, A_2, \ldots, A_n\}$ with the set of subscripts $i = \{1, 2, \ldots, n\}$ and the surface integral is replaced by the sum of discrete surfaces

$$\oiint\limits_{S} x(s) dS = \sum_{i} \oiint\limits_{A_i} x(A_i) dA_i \qquad \sum_{i} A_i = \oiint\limits_{S} dS \tag{2.5}$$

since **u** is not guaranteed to be constant over any of these discrete areas however, as it is by definition a continuous field, it is replaced by the mean velocity across that area times the area, also know as the flow rate.

$$Q_i = \oiint_{A_i} (\mathbf{u} \cdot \hat{n})\, dA_i \tag{2.6}$$

similarly to the simplification done to achieve equation 2.4, it is then assumed that the density field ρ remains constant over each A_i. This transforms equation 2.4 into:

$$\frac{\partial}{\partial t}\rho V + \sum_i \rho_i Q_i = 0 \qquad \left[\frac{kg}{s}\right] \tag{2.7}$$

which, finally, when concerning oneself with only steady-state solutions, can be further reduced to:

$$\sum_i \rho_i Q_i = 0 \qquad \left[\frac{kg}{s}\right] \tag{2.8}$$

which can then be used to produce one equation per control volume in the system of interest. For an example of such a control volume, see figure 2.1. Alternatively, if a transient implementation is desired, the time derivative is retained and discretized according to:

$$\frac{\partial \rho_V}{\partial t} V + \sum_i \rho_i Q_i = 0 \qquad \left[\frac{kg}{s}\right] \tag{2.9}$$

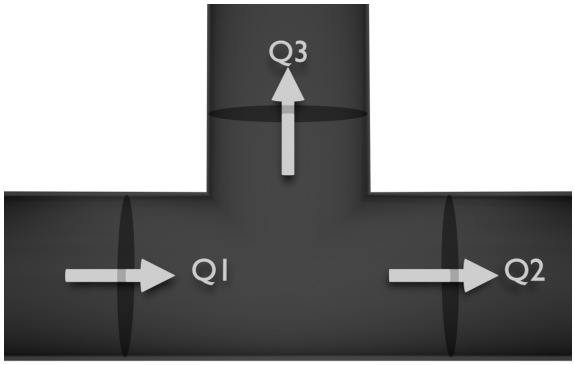

Figure 2.1: Example of a control volume with three different flow rates: Q1, Q2 and Q3 on which equation 2.8 can be applied

2.2 Pressure Drop

With the continuity equation providing one equation per control volume, it, together with a single velocity boundary condition, would only be sufficient to describe the flow rate throughout a system if there were an equal number of control volumes

as there were interfaces between them. This would be the case with a singular, straight pipe with the surfaces over which the balance is established defined as a set of planes in normal directions of the pipe. For any system that includes any form of split in the pipes however, there is a need for additional equations in order to sufficiently describe the flow rate throughout the system. The number of these equations is equal to the number of surfaces minus the number of control volumes. In order to find these equations, the state variable Pressure is utilized, as its value and by extension its change in value is independent of the path taken. Hence, for any two paths 1 and 2 that begin at some identical point a and end at some other identical point b it can be stated that the total pressure drop along those paths must be equal:

$$\sum_{\text{Path 1}} \partial p - \sum_{\text{Path 2}} \partial p = 0 \tag{2.10}$$

for an example of these paths, see figure 2.2.

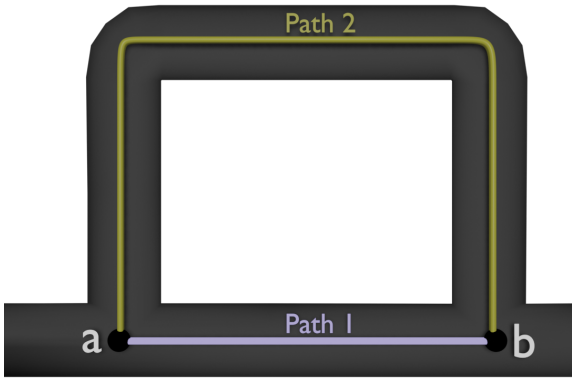

Figure 2.2: Example of two different paths: 1 and 2 from point a to b in a pipe network on which equation 2.10 can be applied

Using this, an additional equation can be generated for every possible 'path' through control volumes from one point to another. When a pipe splits in two, meaning there exists one incoming surface and two outgoing ones from some choice of direction, this will generate one additional equation. If the pipe splits into more than two at any point, such as having one incoming pipe and three outgoing, there exists $\sum_i^{n-1} i$ possible selections of two paths for an n-split pipe. However, many of these will be redundant, as for the threefold split, the equations are as follows:

$$\sum_{\text{Path 1}} \partial p - \sum_{\text{Path 2}} \partial p = 0 \tag{2.11}$$

$$\sum_{\text{Path 1}} \partial p - \sum_{\text{Path 3}} \partial p = 0 \tag{2.12}$$

$$\sum_{\text{Path 2}} \partial p - \sum_{\text{Path 3}} \partial p = 0 \tag{2.13}$$

however, equation 2.11 and 2.12 together imply equation 2.13, hence it is redundant and not needed. Similarly for $n = 4$ there exists a total of 6 equations, out of which 3 are redundant, and so on. Hence, for a pipe split of degree n we have $n - 1$ non-redundant equations. This is exactly sufficient to account for the equations needed to sufficiently describe the pipe system when combined with equation 2.8.

2.2.1 Darcy-Weisbach and Minor Losses

Since the objective of this system of equations is to solve the volumetric flow rates Q, there is a need to establish the relationship between ∂p and Q. To do this, the Darcy-Weisbach equation is utilized. With two additions however, one for minor losses that arise from pipe bends, T-junctions and the like is utilized, and one for height differences. [2]:

$$\partial p = \rho \left(f_D \frac{L}{D} + K \right) \frac{v^2}{2} + \rho g \partial h \tag{2.14}$$

where f_D is known as the Darcy Friction Factor, L is the length of the pipe, D is the diameter of the pipe, K is the effective minor loss coefficient for the pipe (if any) which will be explained in section 2.2.3. v is the average velocity, equal to the flow Q divided by the area A. In order to attain a transient version of the Darcy-Weisbach formula, the momentum inertia needs to be accounted for, which can be represented by adding an unsteady friction term J_u [9]

$$\partial p = \rho \left(f_D \frac{L}{D} + K \right) \frac{v^2}{2} + \rho g \partial h + J_u \tag{2.15}$$

where J_u and it's significant components are descriped in equations 2.16 and equations 2.17

$$J_u = \rho k_3 \left(\frac{\partial \mathbf{u}}{\partial t} - a \nabla \cdot \mathbf{u} \right) \tag{2.16}$$

$$k_3 = 2\sqrt{C^*} \qquad C^* = \frac{7.41}{\mathrm{Re}^{\kappa}} \qquad \kappa = \log_{10}\left(\frac{14.3}{\mathrm{Re}^{0.05}} \right) \tag{2.17}$$

where a is the wave propagation velocity, which for air is roughly 330 meters per second and Re is the Reynolds number. In order to implement this equation into the larger system, we also need values for K and an expression for the Darcy friction factor f_D.

2.2.2 Darcy Friction Factor

In order to determine f_D, it is assumed that the pipes through which the fluid flows are mostly smooth. This then gives an expression for f_D for laminar flows that follows from Poiseuille's law:

$$f_D = \frac{64}{\mathrm{Re}} = \frac{64 \mu A}{\rho Q D} \tag{2.18}$$

for the turbulent, due to the assumed smoothness of the pipe, the Kármán–Prandtl resistance equation can be used to model the friction factor [14]:

$$\frac{1}{\sqrt{f_D}} = 1.930 \log\left(\mathrm{Re}\sqrt{f_D} \right) - 0.537 \approx 0.838 W\left(0.629 \mathrm{Re}\right) \tag{2.19}$$

or, isolating f_D:

$$f_D = \left(\frac{1}{0.838 W\left(0.629 \mathrm{Re}\right)} \right)^2 \tag{2.20}$$

where W is the Lambert W function.

2.2.3 Minor Loss Coefficient

For determining the minor loss coefficient K in equation 2.14, the system in question concerns itself primarily with three types of minor losses. These three types are Minor losses in bends, minor losses in t-junctions and minor losses of an unknown 'box'. The bends in the system are assumed to be of the flanged variant, thus having an associated minor loss coefficient of 0.3. The unknown box was estimated using a comparison to ANSYS FLUENT (see methodology) to have a value somewhere in the range of 200, see table 2.1 for a summary of these coefficients. For the minor loss coefficient in t-junctions, formulas from Andrew Vazsonyi's work is used as follows [15].

$$K_{0,1} = \lambda_1 + (2\lambda_2 - \lambda_1)\left(\frac{v_1}{v_0}\right)^2 - 2\lambda_2\left(\frac{v_1}{v_0}\right)\cos\alpha' \tag{2.21}$$

for t-junctions where there is one incoming flow and two outgoing, also known as dividing flows. Where $K_{0,1}$ represents the minor loss coefficient for the incoming flow 0 to the outgoing flow 1. v_0 is the velocity of the incoming fluid and v_1 is the velocity of the outgoing fluid in the chosen direction. For the factors λ_1 and λ_2 as well as α', they are calculated as follows:

$$\lambda_1 = 0.0712\alpha^{0.7141} + 0.37 \qquad \alpha < \frac{\pi}{8} \tag{2.22}$$

$$\lambda_1 = 1 \qquad \alpha \geq \frac{\pi}{8} \tag{2.23}$$

$$\lambda_2 = 0.0592\alpha^{0.7029} + 0.37 \qquad \alpha < \frac{\pi}{8} \tag{2.24}$$

$$\lambda_2 = 0.9 \qquad \alpha \geq \frac{\pi}{8} \tag{2.25}$$

$$\alpha' = 1.41\alpha - 0.00594\alpha^2 \tag{2.26}$$

where α is the angle by which the t-junction diverts. For combining flows, where there are two incoming flows and one outgoing, equation 2.27 is utilized:

$$K_{0,1} = \lambda_3\left(\frac{v_1}{v_0}\right)^2 + 1 - 2\left(\left(\frac{v_1}{v_0}\right)\left(\frac{Q_1}{Q_0}\right)\cos\beta' + \left(\frac{v_2}{v_0}\right)\left(\frac{Q_2}{Q_0}\right)\cos\alpha'\right) \tag{2.27}$$

where λ_3 is dependent on β, the angle of of the opposite flow (2), with important values being $\lambda_3(0) \approx 1$ and $\lambda_3\left(\frac{pi}{2}\right) \approx 0.6$. Q_i is the volumetric flow rate across the respective junction and β' is calculated as per equation 2.26, although using β rather than α.

Table 2.1: Gathered reference table for minor loss coefficients

Minor loss type	Minor loss coefficient K
Threaded Bend	1.5
T-junction	Equation 2.21 & 2.27
Unknown box	200

2.3 Material Properties

Since we are dealing with a compressible fluid in the form of air, it's density will vary based on both pressure and temperature according to:

$$\rho = \frac{PM}{RTZ(P,T)} \qquad \left[\frac{kg}{m^3}\right] \tag{2.28}$$

where P is the pressure, M is the molar mass, T is the temperature, R is the gas constant and Z is the compressibility, which varies by both P and T respectively. An approximation for how this compressibility varies is given below [10]:

$$Z(P,T) \approx 1 + \begin{bmatrix} 5.56e-11 \\ -2.07e-8 \\ 2.71e-6 \\ -6.37e-8 \\ 1.26e-6 \\ -5.88e-4 \\ 2.49e-9 \\ -3.33e-7 \end{bmatrix}^T \begin{bmatrix} P^2T^2 \\ P^2T \\ P^2 \\ PT^2 \\ PT \\ P \\ T^2 \\ T \end{bmatrix} \tag{2.29}$$

where P is given in Atmospheres and T in Kelvin. Likewise, viscosity will not remain constant with varying temperature either. The equation used to describe its temperature dependence is given below [3]:

$$\mu_T = \mu_{273.15} \left(\frac{T}{273.15}\right)^{3/2} \frac{273.15 + S_{air}}{T + S_{air}} \tag{2.30}$$

where S_{air} is determined to be roughly 109.7 and $\mu_{273.15} = 1.7231 \cdot 10^{-5}$

2.3.1 Heat Balance

In order to calculate the temperature in the system, begin with the equation for Conservation of Energy [13].

$$\rho\left[\frac{\partial h}{\partial t} + \nabla \cdot (h\mathbf{u})\right] = -\frac{\partial p}{\partial t} + \nabla \cdot (k\nabla T) + \Phi + S_h \tag{2.31}$$

where Φ is the dissipation term, see equation 2.32, and S_h is a source term:

$$\Phi = \sum_i \sum_j \eta_{eff}\left(\dot{\varepsilon}_{ij}\dot{\varepsilon}_{ij} - \frac{1}{3}\dot{\varepsilon}_{ii}^2\right) \tag{2.32}$$

where $\dot{\varepsilon}$ is the strain rate tensor [7]:

$$\dot{\varepsilon} = \begin{bmatrix} \frac{\partial \mathbf{u}_x}{\partial x} & \frac{1}{2}\left(\frac{\partial \mathbf{u}_y}{\partial x} + \frac{\partial \mathbf{u}_x}{\partial y}\right) & \frac{1}{2}\left(\frac{\partial \mathbf{u}_z}{\partial x} + \frac{\partial \mathbf{u}_x}{\partial z}\right) \\ \frac{1}{2}\left(\frac{\partial \mathbf{u}_y}{\partial x} + \frac{\partial \mathbf{u}_x}{\partial y}\right) & \frac{\partial \mathbf{u}_y}{\partial y} & \frac{1}{2}\left(\frac{\partial \mathbf{u}_z}{\partial y} + \frac{\partial \mathbf{u}_y}{\partial z}\right) \\ \frac{1}{2}\left(\frac{\partial \mathbf{u}_z}{\partial x} + \frac{\partial \mathbf{u}_x}{\partial z}\right) & \frac{1}{2}\left(\frac{\partial \mathbf{u}_z}{\partial y} + \frac{\partial \mathbf{u}_y}{\partial z}\right) & \frac{\partial \mathbf{u}_z}{\partial z} \end{bmatrix} \tag{2.33}$$

$$\Phi = \eta_{eff}\left(\frac{1}{2}\left(\frac{\partial \mathbf{u}_y}{\partial x}+\frac{\partial \mathbf{u}_x}{\partial y}\right)^2+\frac{1}{2}\left(\frac{\partial \mathbf{u}_z}{\partial x}+\frac{\partial \mathbf{u}_x}{\partial z}\right)^2+\frac{1}{2}\left(\frac{\partial \mathbf{u}_z}{\partial y}+\frac{\partial \mathbf{u}_y}{\partial z}\right)^2\right) \tag{2.34}$$

where η_{eff} is the effective viscosity due to strain, currently assumed to be negligible due to only looking at a 1-D case. h is the specific enthalpy of the system, defined as [8]:

$$h = c_p T + \frac{p}{\rho} \tag{2.35}$$

which when returned to the energy equation expands it to :

$$\rho\left[c_p\frac{\partial T}{\partial t}+c_p\nabla\cdot(T\mathbf{u})+\frac{1}{\rho}\frac{\partial p}{\partial t}+\frac{1}{\rho}\nabla\cdot(p\mathbf{u})\right] = -\frac{\partial p}{\partial t}+\nabla\cdot(k\nabla T)+\Phi+S_h \quad \left[\frac{J}{sm^3}\right] \tag{2.36}$$

multiplying in ρ where convenient and separating the pressure and temperature terms yield:

$$\rho\left[c_p\frac{\partial T}{\partial t}+c_p\nabla\cdot(T\mathbf{u})\right]-\nabla\cdot(k\nabla T)-\Phi = -2\frac{\partial p}{\partial t}-\nabla\cdot(p\mathbf{u})+S_h \quad \left[\frac{J}{sm^3}\right] \tag{2.37}$$

which, when integrated over a control volume V yields:

$$\iiint_V \rho c_p\frac{\partial T}{\partial t}dV+\iiint_V \rho c_p\nabla\cdot(T\mathbf{u})\,dV-\iiint_V \nabla\cdot(k\nabla T)\,dV-\iiint_V \Phi dV \tag{2.38}$$

$$= -2\iiint_V \frac{\partial p}{\partial t}dV-\iiint_V \nabla\cdot(p\mathbf{u})\,dV+\iiint_V S_h dV \quad \left[\frac{J}{s}\right] \tag{2.39}$$

after that, Gauss theorem is applied to relevant terms:

$$\iiint_V \rho c_p\frac{\partial T}{\partial t}+\oiint_S \rho c_p\,(T\mathbf{u})\,dS-\oiint_S (k\nabla T)\,dS-\iiint_V \Phi dV \tag{2.40}$$

$$= -2\iiint_V \frac{\partial p}{\partial t}dV-\oiint_S (p\mathbf{u})\,dS+\iiint_V S_h dV \quad \left[\frac{J}{s}\right] \tag{2.41}$$

V is then assumed to be small enough that values within are effectively constant.

$$\rho c_p\frac{\partial T}{\partial t}V+\rho c_p\oiint_S T\mathbf{u}dS-k\oiint_S \nabla T dS-\Phi V \tag{2.42}$$

$$= -2\frac{\partial p}{\partial t}V-\oiint_S (p\mathbf{u})\,dS+S_h V \quad \left[\frac{J}{s}\right] \tag{2.43}$$

similarly to the handling of the continuity equations, replace surface integral with sum of discrete surfaces as per equation 2.5: Utilize equation 2.6 and assume all other variables act as local constants carried by the volumetric flow rate:

$$\rho c_p\frac{\partial T}{\partial t}V+\sum_i (\rho c_p TQ)_i-\sum_i (k\nabla TA)_i-\Phi V \tag{2.44}$$

$$= -2\frac{\partial p}{\partial t}V-\sum_i (pQ)_i+S_h V \quad \left[\frac{J}{s}\right] \tag{2.45}$$

assuming there exists more than one constant cell, and that they are adjacent, ∇T can be approximated using these two cells a and b as:

$$\nabla T \approx \frac{T_a - T_b}{L_{a\to b}} = \frac{\partial T_i}{L_i} \tag{2.46}$$

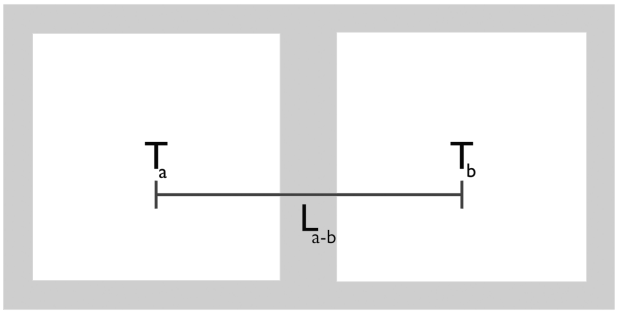

Figure 2.3: Demonstration of the geometry behind the approximation of ∇T

Where $L_i := L_{a\to b}$ for $i \in \{0, \ldots, M\}$ where M is the number of interfaces in a given geometry, is the distance between the center of the cells, see figure 2.3 for an example, gives:

$$\rho c_p \frac{\partial T}{\partial t} V + \sum_i \left(\rho c_p T Q\right)_i - \sum_i \left(kA\frac{\partial T}{L}\right)_i - \Phi V = -2\frac{\partial p}{\partial t} V - \sum_i \left(pQ\right)_i + S_h V \quad \left[\frac{J}{s}\right] \tag{2.47}$$

ignoring Φ which was previously presumed negligible and looking at the steady-state variant of the equation yields, when combining the sums.

$$\sum_i \left(\rho c_p T Q - kA\frac{\partial T}{L} + pQ\right)_i = S_h V \qquad \left[\frac{J}{s}\right] \tag{2.48}$$

In order to formulate a transient solution, instead approximate $\frac{\partial T}{\partial t} \approx \frac{T_t - T_{t-\partial t}}{\partial t}$ and $\frac{\partial p}{\partial t} \approx \frac{p_t - p_{t-\partial t}}{\partial t}$ and assume all cross-wall transport utilizes the temperature in the prior time step $T_{t-\partial t}$:

$$\rho c_p \frac{T_t - T_{t-\partial t}}{\partial t} V + \sum_i \left(\rho c_p T Q - kA\frac{\partial T}{L} + pQ\right)_{i,t-\partial t} = -2\frac{p_t - p_{t-\partial t}}{\partial t} V + S_h V \quad \left[\frac{J}{s}\right] \tag{2.49}$$

which yields an equation for T_t when shifted around:

$$T_t = T_{t-\partial t} - 2\frac{(p_t - p_{t-\partial t})}{\rho c_p} - \frac{\partial t}{V \rho c_p}\left(\sum_i \left(\rho c_p T Q - kA\frac{\partial T}{L} + pQ\right)_{i,t-\partial t} + S_h V\right) \quad [K] \tag{2.50}$$

2.3.2 Thermal properties

The coefficients k and c_p calculated as [3]:

$$k = \frac{9\gamma - 5}{4} c_v \mu \qquad c_v = \frac{R}{\gamma - 1}\frac{1}{M} \qquad c_p = \frac{\gamma R}{\gamma - 1}\frac{1}{M} \tag{2.51}$$

where μ is the temperature-dependent viscosity as per equation 2.30 and $\gamma \approx 1.4$ is the heat capacity ratio for air [16].

2.3.3 Interpolation of temperature at flow-faces

For determining the value of $T_{a\to b}$, the temperature being carried by the flow rate Q_is, it is approximated as a linear combination of T_a and T_b based on the analytical solution of the 1-D isobaric steady-state heat equation for a normalized distance $x \in (0, 1)$. This is done instead of standard linear interpolation in order to attempt to combat the potential error cause by the large cell sizes:

$$T(x) = -\frac{T_1 - T_0\,\mathrm{e}^{-\alpha}}{\mathrm{e}^{-\alpha} - 1} - \frac{\mathrm{e}^{-\alpha x}\,(T_0 - T_1)}{\mathrm{e}^{-\alpha} - 1} \tag{2.52}$$

where α is defined by equation 2.53:

$$\alpha = \frac{\rho c_p Q}{k\frac{A}{L}} \tag{2.53}$$

which, when using the scaled temperatures $T_1 = 1$ and $T_0 = 0$ has the expected value:

$$E[T(x)] = -\frac{1}{\alpha} - \frac{1}{\mathrm{e}^{-\alpha} - 1} = \beta \tag{2.54}$$

For a visualization of what this expected value evaluates to at differing values of α, see figure 2.4.

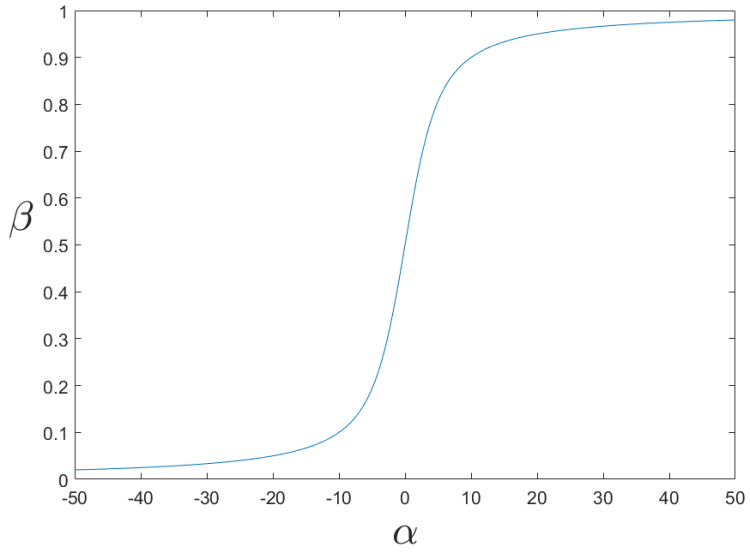

Figure 2.4: The average interface temperature scaling as per equation 2.54

thus, let:

$$T_{a\to b} = (1-\beta)\, T_a + \beta T_b \tag{2.55}$$

Assuming a set of volumetric flow rates Q_i and pressure p_i exists from a prior solution to the momentum equation, there are a number of unknowns T equal to the number of control volumes, since interface-values can be extrapolated from control-volume values.

2.3.4 Heat Transfer over wall

There exists additional sources of heat in each control volume however, as heat may transfer through solid walls that exist within the volume as per the heat transfer equation [5]:

$$\dot{q} = UA\,(T_o - T_i) \qquad \left[\frac{J}{s}\right] \tag{2.56}$$

where T_i is the temperature in the control volume, T_o is the temperature on the other side of the wall, A is the area over which the heat is transferred and U is the overall heat transfer coefficient, calculated as follows [5]:

$$UA = \frac{1}{\frac{1}{h_i A_i} + \frac{d_w}{k_w A_w} + \frac{1}{h_o A_o}} \tag{2.57}$$

where h_i, h_o is the heat transfer coefficient for the internal fluid and external fluid respectively, k_w is the thermal conductivity of the wall material, d_w is the wall thickness, and A_i, A_o & A_w is the respective areas over which the heat is transferred.

In order to determine the heat transfer coefficients for the fluids, the default assumption is that the outside heat transfer coefficient arises from free convection and that the internal flow Q is known. As such, for the internal heat transfer coefficient h_i, the Gnielinski correlation for forced convection is utilized [6]:

$$\mathrm{Nu}_L = \frac{hL}{k} = \frac{\left(\frac{f}{8}\right)(\mathrm{Re}_L - 1000)\,\mathrm{Pr}}{1 + 12.7\sqrt{\left(\frac{f}{8}\right)}\left(\mathrm{Pr}^{\frac{2}{3}} - 1\right)} \tag{2.58}$$

which is valid for:

$$0.5 \le \mathrm{Pr} \le 2000 \qquad\qquad 3000 \le \mathrm{Re}_L \le 5 \cdot 10^6 \tag{2.59}$$

where L is the characteristic length, here meaning $\frac{V}{S}$, f is the Darcy Friction Factor as per equation 2.20 Re_L is the Reynolds number for the same characteristic length and Pr is the Prandtl number.

$$\mathrm{Pr} = \frac{c_p \mu}{k} \qquad\qquad \mathrm{Re}_L = \frac{\rho \mathbf{u} L}{\mu} \tag{2.60}$$

If the Gnielinski correlation is invalid, most likely due to the velocity $\mathbf{u}$ being low enough to cause the Reynolds number to drop below 3000, the Nusselt number for for circular tubes with uniform heat flux is utilized instead:

$$\mathrm{Nu}_L = 4.36 \tag{2.61}$$

The inner heat transfer coefficient can then be approximated as:

$$h_i = \frac{\mathrm{Nu}_L k}{L} \tag{2.62}$$

When looking at the external heat transfer coefficient, a different correlation is needed to approximate the value from what is assumed to be free convection. Here, the Churchill and Chu correlation is used[4]:

$$\bar{\mathrm{Nu}}_L = 0.68 + \frac{0.663\mathrm{Ra}_L^{\frac{1}{4}}}{\left[1 + \left(\frac{0.492}{\mathrm{Pr}}\right)^{\frac{9}{16}}\right]^{\frac{4}{9}}} \tag{2.63}$$

which is valid for:

$$\mathrm{Ra}_L \leq 10^8 \tag{2.64}$$

where Ra_L is the Rayleigh number, usually written as the product of the Grashof number and the Prandtl number:

$$\mathrm{Ra}_L = \mathrm{GrPr} = \frac{\rho\hat{\beta}\Delta T l^3 g}{\mu\hat{\alpha}} \tag{2.65}$$

where $\hat{\beta}$ (K^{-1}) is the thermal expansion coefficient, ΔT is the temperature difference between the wall and the outside fluid and $\hat{\alpha} = \frac{k}{\rho c_p}$ is the thermal diffusivity . Like for the internal heat transfer coefficient, the external heat transfer coefficient is calculated in the same manner $h_o = \frac{\bar{\mathrm{Nu}}_L k}{L}$. In order to determine the wall temperature T_w for ΔT, it is assumed that $\frac{k_{Wall}}{d_{Wall}} >> h_i, h_o$, hence the wall temperature reaches steady state much faster than the fluid and can be approximated using the steady state approximation:

$$\partial T = T_w - T_o \qquad\qquad T_w = \frac{h_i A_i T_i + h_o A_o T_o}{h_i A_i + h_o A_o} \tag{2.66}$$

2.3.5 Shell Conduction

Even though T_w is, for the most part, uniform in the normal direction through the wall, it is not necessarily so along the length of the wall interior. Hence, an alternative approach to determining T_w is to treat the wall as an additional control volume. This approach allows for inclusion of conduction factors in directions along the wall interior. Assuming that the wall is solid, and as such no convection occurs in the wall volume, the equation for the wall volume becomes:

$$\iiint_V \rho_w \left[c_{p,w}\frac{\partial T_w}{\partial t}\right] dV = \oiint_{A-\{A_i,A_o\}} (k_w \nabla T)\, dA + \oiint_{A_o} U\,(T_o - T_w)\, dA_o + \oiint_{A_i} U\,(T_i - T_w)\, dA_i \tag{2.67}$$

There the terms on the right hand side can be labeled as the internal conduction, the outside heat and the inside heat respectively. For a visual reference of these different terms, see figure 2.5.

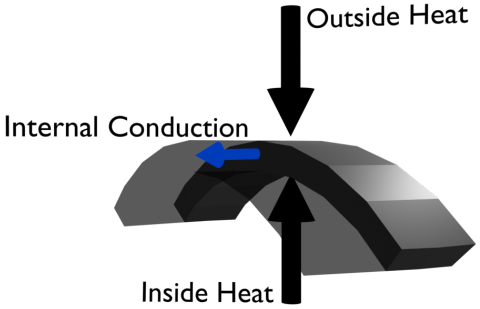

Figure 2.5: Visual reference for heat transfer in the wall of a pipe, terminology originates from equation 2.67

Assuming sufficiently small areas and volumes that internal values can be considered constant.

$$V_w \rho_w c_{p,w} \frac{\partial T_w}{\partial t} = \sum_j \left(k_w \nabla T\right) S_j + UA_o \left(T_o - T_w\right) + UA_i \left(T_i - T_w\right) \tag{2.68}$$

This can then be further simplified by approximating ∇T as a difference between the current node $T_{w,n}$ and the adjacent wall segment on the other side of the surface S_j, $T_{w,j}$ divided by the distance between them $L_{n \to j}$:

$$\nabla T \approx \frac{T_{w,n} - T_{w,j}}{L_{n \to j}} \tag{2.69}$$

leading to the following equation for a transient wall volume:

$$V_{w,n} \rho_w c_{p,w} \frac{\partial T_{w,n}}{\partial t} = \sum_j k_w S_j \frac{T_{w,n} - T_{w,j}}{L_{n \to j}} + UA_o \left(T_{o,n} - T_{w,n}\right) + UA_i \left(T_{i,n} - T_{w,n}\right) \tag{2.70}$$

or it's steady-state equivalent:

$$0 = \sum_j k_w S_j \frac{T_{w,n} - T_{w,j}}{L_{n \to j}} + UA_o \left(T_{o,n} - T_{w,n}\right) + UA_i \left(T_{i,n} - T_{w,n}\right) \tag{2.71}$$

3

Methods

3.1 Geometry

In order to apply the derived equations for a flow rate solver, such as equation 2.8, equation 2.10 and equation 2.48, a set of control volumes and surfaces is needed in order to achieve a FVM-style discretization. Due to the need to validate any such solution for any geometry against prior sources, the geometries constructed for this solver are based on equivalent geometries constructed for a commercial solver, namely ANSYS FLUENT. The basis for the geometries constructed in the implementation can be seen in figures 3.1 and figure 3.3

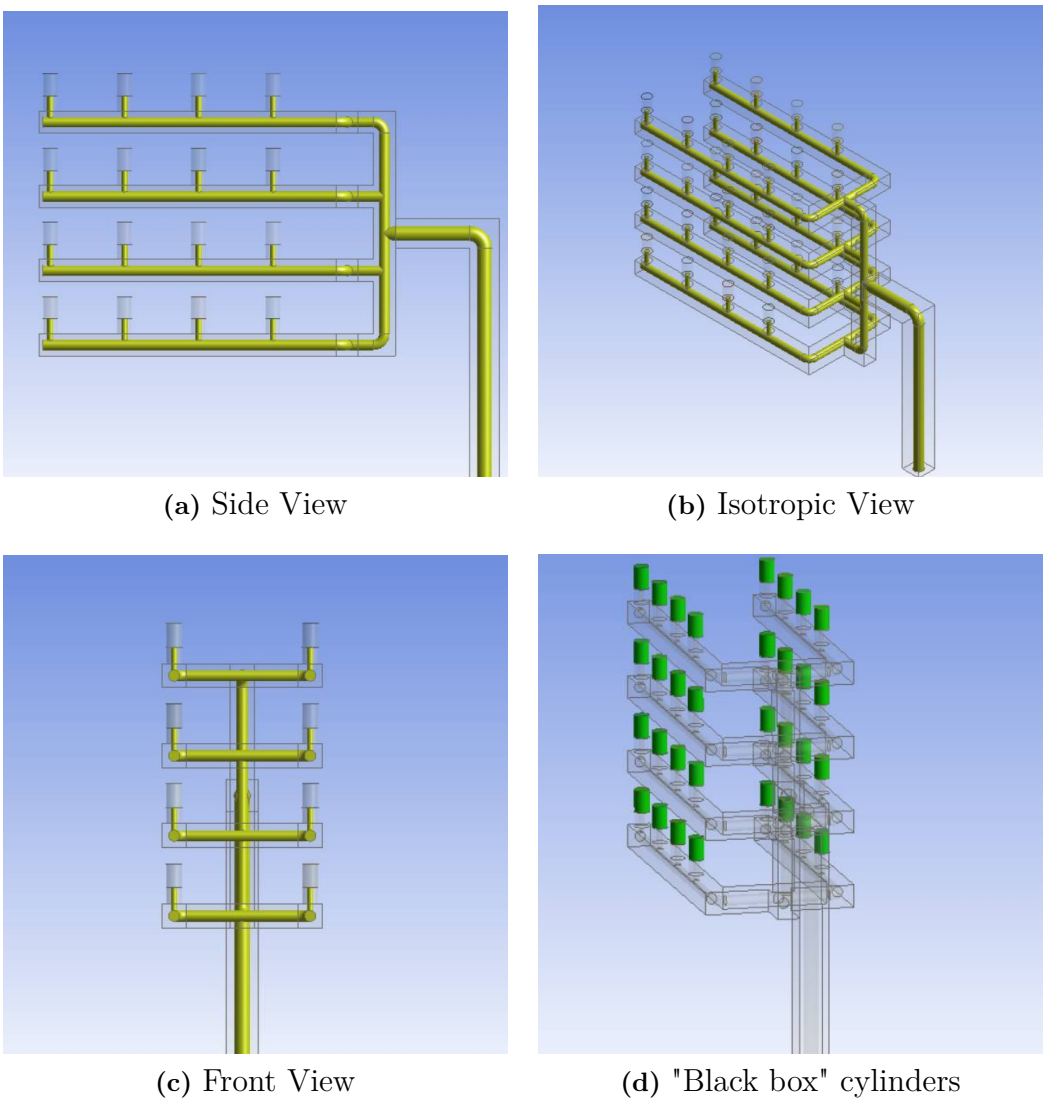

(a) Side View

(b) Isotropic View

(c) Front View

(d) "Black box" cylinders

Figure 3.1: Multi-layer geometry overview

The cylinders observed on top of each layer and arm are otherwise empty volumes that serve to bridge the interior and the exterior and are not representative of any real design, but rather a hypothetical "black box" that contains some manner of heat producing equipment to be cooled. Therefore, these cylinders are henceforth

referred to as 'boxes'. The MATLAB representation of the same geometry can be seen in figure 3.2.

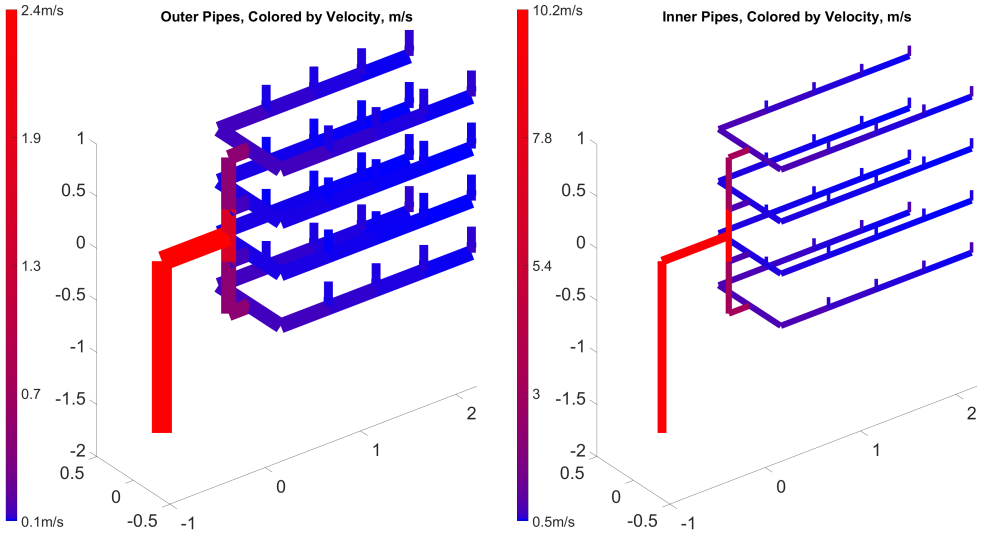

Figure 3.2: MATLAB visualization of the multi layer layer simulation geometry, colored by velocity of a test run

3.1.1 Single layer geometry

In order to isolate the effects of a single arm of the geometry presented in figure 3.1, a secondary geometry was constructed in ANSYS FLUENT, pertaining only to a single layer of the full geometry and without an inflow trunk, but otherwise identical. This geometry is henceforth referred to as the single layer geometry.

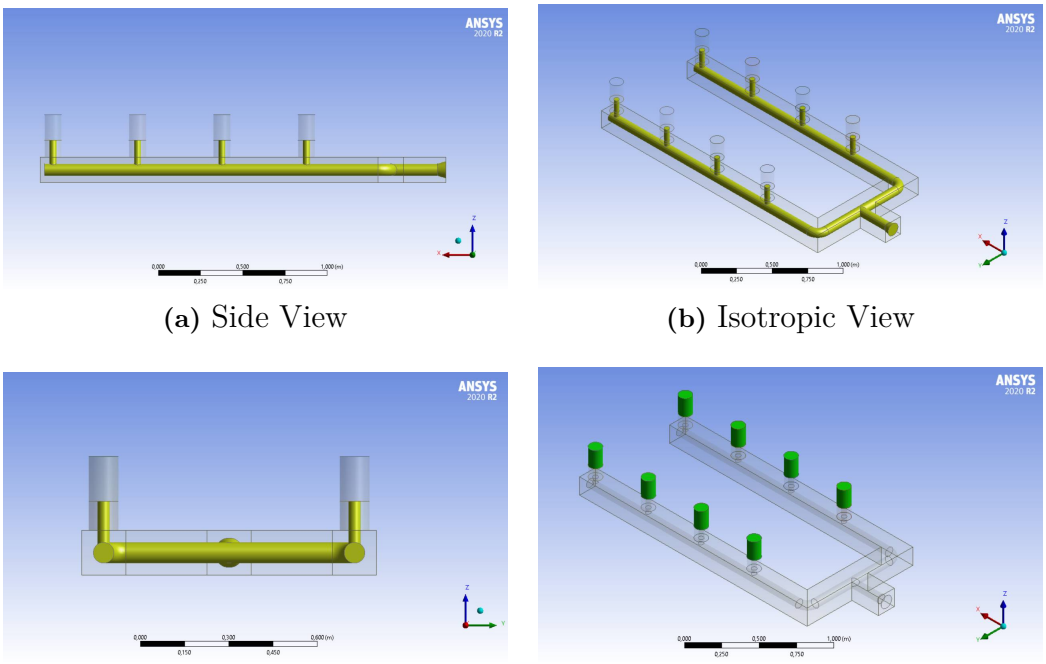

(a) Side View

(b) Isotropic View

(c) Front View

(d) "Black box" cylinders

Figure 3.3: Single geometry overview

Similarly to the multi-layer geometry, the MATLAB equivalent can be seen in figure 3.4.

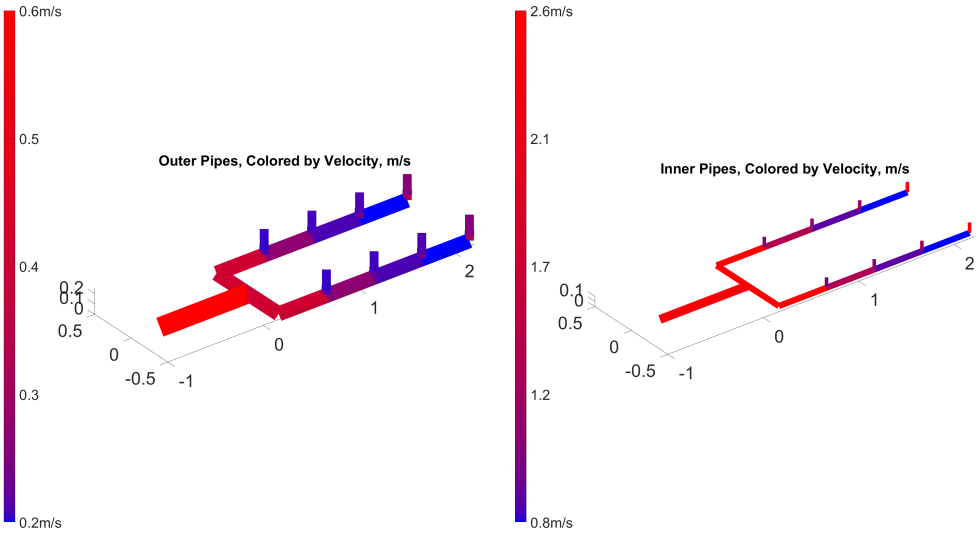

Figure 3.4: MATLAB visualization of the single layer simulation geometry, colored by velocity

3.1.2 Flow rate Solver Implementation

For the purposes of the flow rate solver, it is necessary to define a set of control volumes, or hereafter referenced as nodes $\mathcal{N}$ and a set of surfaces or interfaces between the nodes, hereafter referenced as connections $\mathcal{C}$. It is suitable to think of a node as the connection point between otherwise straight pipes, such as the example in figure 2.1 and connections as the straight pipes that go between them. In order to create these sets, a set of points in 3D space is generated that closely follows the points at which the geometrical basis turns or otherwise splits, which, due to the nature of the geometry, may very well overlap in space.

3.1.2.1 Adjacency Matrix

These points form the basis for the nodes, which are then connected to one another through an adjacency matrix $\mathbf{A}$. Let $\mathbf{A}_{i,j} = 1$ mean that there exists an interface running from node i to node j and $A_{i,j} = 0$ means that there is no interface between the nodes i and j. $\mathbf{A}$ is intentionally kept unidirectional, flowing from the inlet node to the outlet node as one traverses the adjacency matrix, but the omni-directional adjacency matrix $\mathbf{A}_O$ can easily be constructed as per:

$$\mathbf{A}_O = \mathbf{A} + \mathbf{A}^T \tag{3.1}$$

From $\mathbf{A}$ the set of connections can then be defined, holding an equivalent number of elements to the number of non-zero entries in $\mathbf{A}$, where each entry $c \in \mathcal{C}$ has a source S_c and a target T_c such that, for the entry into the adjacency matrix $A_{i,j} = 1$ there exists an unique $c \in \mathcal{C}$ such that $S_c = i$ and $T_c = j$. For a visual reference on how the adjacency matrix appears, with zeroes colored blue and ones colored

yellow, see figure 3.5. When referencing interpolated geometries, the figure refers to a single node inserted in every previously existing connection.

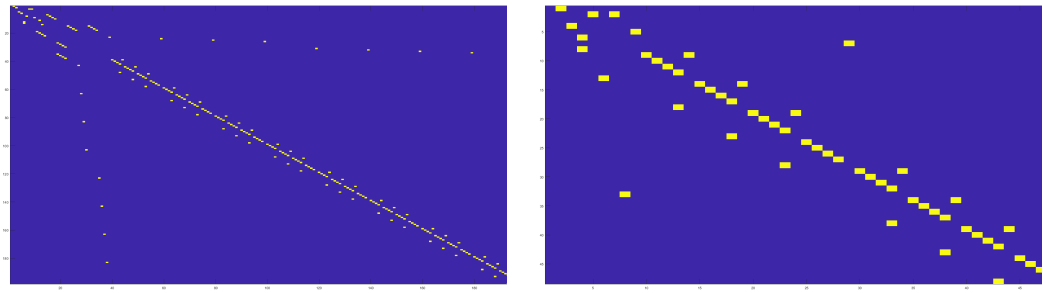

(a) Multi-layer geometry

(b) Single-layer geometry

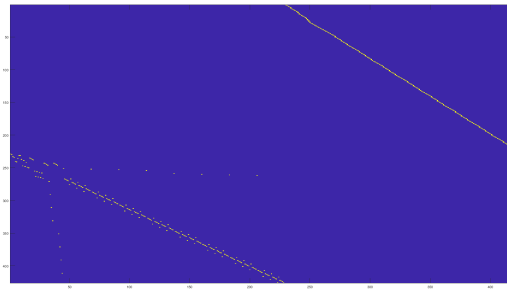

(c) Multi-layer, interpolated

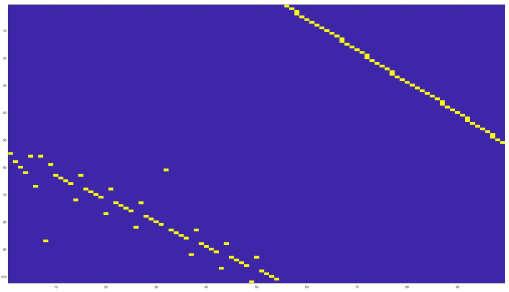

(d) Single-layer, interpolated

Figure 3.5: Visualizations of the adjacency matrix $\mathbf{A}$ with size $|\mathcal{N}|x|\mathcal{N}|$ for different geometries

3.1.2.2 Lengths, diameters, areas and volumes

However, in order to properly define the geometry, it is not sufficient to simply concern oneself with connected points in space. Additionally, information about the area through which the flow traverses must also be available, as well as the length through which it travels over each interface. Length is simple enough to determine, for each connection c, the length is calculated as follows:

$$L_c = \left| [x, y, z]_{T_c} - [x, y, z]_{S_c} \right|_2 \tag{3.2}$$

Meaning simply the distance in 3D space between the source node S_c and the target node T_c. In order to calculate the area of the surface however, information about the radius or diameter is necessary. These cannot be calculated from any existing data however, and thus have to be manually entered, with each connection possessing a diameter or diameter equivalent in the case of non-cylindrical pipes D_c. The area of the connection A_c can then be calculated as follows:

$$A_c = \left(\frac{D_c}{2}\right)^2 \pi \tag{3.3}$$

With this information, calculating the volume of the connection V_c is trivial, since $V_c = A_c L_c$. The volume of a node is also needed. In order to determine that, let

the volume of a node $n \in N$, V_n be equal to half the volume of all incoming and outgoing connections to n in order to ensure $\sum_n V_n = \sum_c V_c$:

$$V_n = \frac{\sum\limits_{S_c=n} V_c + \sum\limits_{T_c=n} V_c}{2} \tag{3.4}$$

Additionally, the inner surface area A_i of a connection and a node is of interest for the purpose of solving equation 2.71. Similarly to the volume, these are calculated relatively trivially for the connections as the circumference times the length $A_{c,i} = D_c \pi L_c$ and interpolated as the half sum of all incoming and outgoing connections for the nodes.

$$A_{n,i} = \frac{\sum\limits_{S_c=n} A_{c,i} + \sum\limits_{T_c=n} A_{c,i}}{2} \tag{3.5}$$

Finally, it is also of interest to calculate the outer surface area A_o of the connections and nodes for the purposes of equation 2.71. Similarly as for the inner surface area, it is trivial for connections and interpolated for the nodes.

$$A_{c,o} = (D_c + d_w)\,\pi L_c \qquad\qquad A_{n,o} = \frac{\sum\limits_{S_c=n} A_{c,o} + \sum\limits_{T_c=n} A_{c,o}}{2} \tag{3.6}$$

Where d_w is the thickness of the wall as previously stated in equation 2.57.

3.2 Matrix System

This section aims to explain the different matrices used in the solver. Now that the set of connections $\mathcal{C}$ and nodes $\mathcal{N}$ along with their respective set of properties and the adjacency matrix has been established, these nodes and connections can be used to establish matrices that allow solutions to equations 2.8, 2.10 and 2.48 to be generated.

3.2.1 Flow Matrix Generation

To begin with, equation 2.8 is considered. Given that the sought after variable Q, the volumetric flow rate, is a property of the connections between nodes and that equation 2.8 is specified for a node, the flow matrix $\mathbf{F}$ is generated as per algorithm 1:

Algorithm 1 Generation of flow matrix $\mathbf{F}$

initialize $\mathbf{F}$ as $[|\mathcal{N}|,\ |\mathcal{C}|]$ size zero matrix
for $i = 1, \ldots, |\mathcal{C}|$ **do**
    $a \leftarrow S_{\mathcal{C}_i}$
    $b \leftarrow T_{\mathcal{C}_i}$
    $\mathbf{F}_{a,i} = -1$
    $\mathbf{F}_{b,i} = 1$
end for
Remove row $\mathbf{F}_{no,\cdot}$ where no is the outlet node.
Return $\mathbf{F}$

The outlet row is removed because it is not necessary, since it is covered by the boundary condition that appears at row ni, the inlet row. Once established, $\mathbf{F}$ can be used to solve equation 2.8 as follows:

$$\mathbf{F}\left(\rho\vec{Q}\right) = \vec{b} \tag{3.7}$$

Where $\rho\vec{Q}$ is the vector of all mass flows in the system and $\vec{b}$ is the solution vector that is 0 in all elements except for row ni, where $\vec{b}_{ni} = \rho\vec{Q}_{in}$ is the velocity inlet boundary condition. For a visualization of the flow matrix for the four different cases displayed in figure 3.5, see figure 3.6. -1 is colored blue in the figure, 1 is colored yellow and 0 is colored green.

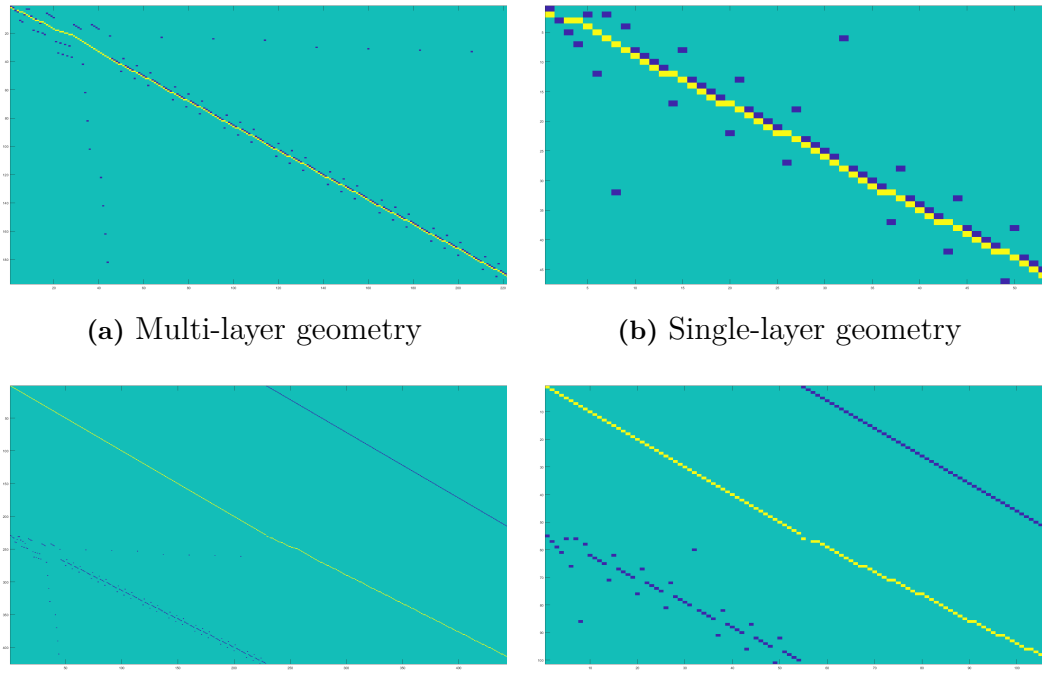

(a) Multi-layer geometry

(b) Single-layer geometry

(c) Multi-layer, interpolated

(d) Single-layer, interpolated

Figure 3.6: Visualizations of the flow matrix $\mathbf{F}$ of size $(|\mathcal{N}| - 1)x|\mathcal{C}|$ where green is 0, blue is -1 and yellow is $+1$

3.2.2 Pressure Drop Matrix Generation

As previously stated, equation 3.7 is insufficient to describe the system by itself. To this end, equation 2.10 needs to be implemented. In order to do this, consider the set of paths $\mathcal{P}$ where $\mathcal{P}_i$ is the set of connections that make up path i, and the set of path differentials $\mathcal{D}$, since $|\mathcal{C}| - |\mathcal{N}| - 1 = |\mathcal{D}|$. Where $\mathcal{D}$ is defined as follows:

$$\mathcal{D} = \left\{ \delta_{\mathcal{P}_i} - \delta_{\mathcal{P}_j} \middle| \begin{matrix} i = 1, \ldots, |\mathcal{P}| \\ i \neq j \\ \mathcal{P}_i, \mathcal{P}_j \in \mathcal{P} \\ \delta_{\mathcal{P}_j} - \delta_{\mathcal{P}_i} \notin \mathcal{D} \end{matrix} \right\} \tag{3.8}$$

Where $\delta_{\mathcal{P}_i}$ means 0 if $c \notin \mathcal{P}_i$ and 1 if $c \in \mathcal{P}_i$. The exclusion of the reverse loop $\delta_{\mathcal{P}_j} - \delta_{\mathcal{P}_i}$ is included in the set definition to remove the redundant equations otherwise generated, such as with equation 2.13 in the theory section. There exists a variety of ways to generate $\mathcal{D}$, or more accurately its matrix representation $\mathbf{D}$. One such way that works for simple, binary tree pipe systems is provided in algorithm 2.

Algorithm 2 Generation of pressure drop matrix $\mathbf{D}$

Initialize list of start nodes $\vec{n_s}$
for $i = 1, \ldots, |\mathcal{N}|$ **do**
    $x = 0$
    for $j = 1, \ldots, |\mathcal{N}|$ **do**
        $x = x + \mathbf{A}_{i,j}$
    end for
    if $x \geq 2$ **then**
        Append i to $\vec{n_s}$
    end if
end for
Initialize $\mathbf{D}$ as $[|\vec{n_s}|, \ |\mathcal{C}|]$ zero matrix
for $i = 1, \ldots, |\vec{n_s}|$ **do**
    Get connections $\vec{c} = \{c \in \mathcal{C} | S_c = \vec{n_s}(i)\}$
    Initialize node vector $\vec{n} = \left\{T_{\vec{c}(1)}, T_{\vec{c}(2)}\right\}$
    Initialize path 1 list $\vec{P_1} = \vec{c}_1$
    Initialize path 2 list $\vec{P_2} = \vec{c}_2$
    while $\nexists \vec{P_1} \in \vec{P_2}$ **do**
        for $i = 1, 2$ **do**
            Get connection $c = \{c \in \mathcal{C} | S_c = \vec{n}_i\}$
            Append $c(1)$ to $\vec{P_i}$.
            $\vec{n}_i = T_{c(1)}$
        end for
    end while
    $c = \left\{c \in \mathcal{C} | c \in \vec{P_1} \ \ \& \ \ c \in \vec{P_2}\right\}$
    Get a, the index of c in $\vec{P_1}$.
    $\vec{P_1} = \vec{P_1}(1, \ldots, a)$
    Get b, the index of c in $\vec{P_2}$.
    $\vec{P_2} = \vec{P_2}(1, \ldots, b)$
    $\mathbf{D}_{i,\cdot} = \delta_{\vec{P_1}} - \delta_{\vec{P_2}}$
end for
Return $\mathbf{D}$

An equivalent, but less efficient way to generate $\mathbf{D}$ would for example be to traverse all the paths from the inlet node n_i to the outlet node n_o and then calculate $\mathbf{D}$ as $\mathbf{D}_{i,\cdot} = \vec{P_i} - \vec{P_1}$ for $i \in \{2, \ldots, |\mathcal{P}|\}$. Whichever way is utilized, $\mathbf{D}$ may then be combined with equation 3.7 to produce the full mass flow rate equation:

$$\begin{bmatrix} \mathbf{F}\rho\vec{Q} \\ \mathbf{D}\vec{\Delta p} \end{bmatrix} = \vec{b'} \tag{3.9}$$

Where $\vec{\Delta p}$ is the vector of pressure drops from equation 2.14 and $\vec{b'}$ is the solution vector similar to it's construction in equation 3.7, except being of size $|\mathcal{C}|$ rather than size $|\mathcal{N}| - 1$. In order to actually solve for the mass flow rate however, all independent terms need to be moved to the right hand side. Thus, separate $\vec{\Delta p}$ into the flow dependent pressure drop $\vec{\Delta p_Q}$ and the height dependent pressure drop $\vec{\Delta p_h}$ and move the latter to the left hand:

$$\eta = \begin{bmatrix} 0_1 \\ \dots \\ 0_{|\mathcal{N}|-1} \\ \mathbf{D}\vec{\Delta p_h} \end{bmatrix} \tag{3.10}$$

Where 0_1 to $0_{|\mathcal{N}|-1}$ means $|\mathcal{N}| - 1$ leading 0 value rows.

$$\begin{bmatrix} \mathbf{F}\rho\vec{Q} \\ \mathbf{D}\vec{\Delta p_Q} \end{bmatrix} = \vec{b'} - \eta \tag{3.11}$$

However, ρQ is currently not presented as a singular vector. In order to resolve this, replace $\vec{\Delta p_Q}$ with the variable $\theta = \frac{\vec{\Delta p_Q}}{\rho Q}$ and form the pressure drop coefficient matrix $\mathbf{\Theta}$ such that $\mathbf{\Theta}_{i,j} = \mathbf{D}_{i,j}\theta_j$:

$$\begin{bmatrix} \mathbf{F} \\ \mathbf{\Theta} \end{bmatrix} \rho\vec{Q} = \vec{b'} - \eta \tag{3.12}$$

Which allows for the generation of full solution for $\rho\vec{Q}$. Since $\mathbf{\Theta}$ is not independant on $\rho\vec{Q}$, the equations must be solved iteratively. A basic algorithm for this iterative solution is presented in algorithm 3:

Algorithm 3 Iterative solution of $\rho\vec{Q}$

1: initialize initial guess $\rho\vec{Q}_0$
2: initialize new value $\rho\vec{Q}_1$
3: **while** $\sum \left(\rho\vec{Q}_1 - \rho\vec{Q}_0\right)^2 \geq$ some threshold t **do**
4: $\quad \rho\vec{Q}_0 = \rho\vec{Q}_1$
5: $\quad$ Calculate $\mathbf{\Theta}$ using $\rho\vec{Q}_0$
6: $\quad$ Solve equation 3.12 using $\mathbf{\Theta}$ and store result in $\rho\vec{Q}_1$
7: **end while**
8: Return $\rho\vec{Q}_0$

For a visualization of the pressure drop matrix for the four different cases displayed in figure 3.5, see figure 3.7. -1 is colored blue in the figure, 1 is colored yellow and 0 is colored green.

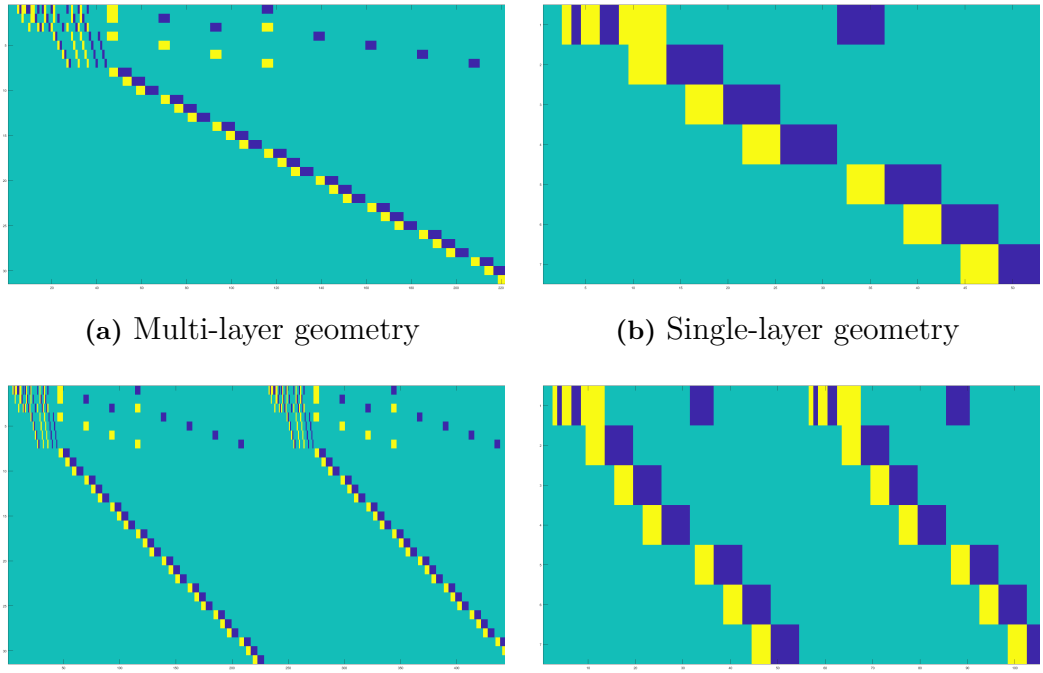

(a) Multi-layer geometry

(b) Single-layer geometry

(c) Multi-layer, interpolated

(d) Single-layer, interpolated

Figure 3.7: Visualizations of the pressure drop matrix $\mathbf{D}$ of size $(|\mathcal{C}| - |\mathcal{N}| + 1)x|\mathcal{C}|$ where green is 0, blue is -1 and yellow is $+1$

3.2.3 Pressure Sum Matrix

For the purposes of solving the density ρ and the temperature T fields, it is of interest to know the actual pressure at the nodes $n \in \mathcal{N}$ and connections $c \in \mathcal{C}$. In order to determine this, the pressure drop vector $\vec{\Delta p}$ is summed over a specific set of nodes running from the inlet node n_i to the node of interest. Additionally, due to the assumed straight-pipe nature of the connections, it is assumed that the pressure drop $\Delta p_{c\in\mathcal{C}}$ is linear. Hence, it is assumed that $p_c = \frac{p_{S_c}+p_{T_c}}{2}$. For a demonstration of how to implement the summation from inlet to node of interest that uses a pressure sum matrix, see algorithm 4.

Algorithm 4 Generation of pressure sum matrix $\mathbf{P}$

initialize $\mathbf{P}$ as $[|\mathcal{N}|,\ |\mathcal{C}|]$ zero matrix
for $i = 1, \ldots, |\mathcal{N}|$ **do**
    initialize current node $n = i$
    initialize next node n_n as the index of the first nonzero element in $\mathbf{A}_i^T$
    Get connection $c_1 = \{c \in \mathcal{C} | S_c = n_n \ \&\ T_c = n\}$
    $\mathbf{P}_{i,c_1} = 1$
    while $n \neq n_i$ **do**
        $n = n_n$
        Get n_n as the index of the first nonzero element in $\mathbf{A}_n^T$
        Get connection $c_1 = \{c \in \mathcal{C} | S_c = n_n \ \&\ T_c = n\}$
        $\mathbf{P}_{i,c_1} = 1$
    end while
end for
Return $\mathbf{P}$

Once the pressure sum matrix $\mathbf{P}$ has been generated, the vector of node pressures $\vec{p_n}$ can be calculated as per equation 3.13

$$\vec{p_n} = \mathbf{P}\vec{\Delta p} \tag{3.13}$$

For a visualization of the pressure sum matrix for the four different cases displayed in figure 3.5, see figure 3.8. 0 is colored blue in the figure and 1 is colored yellow.

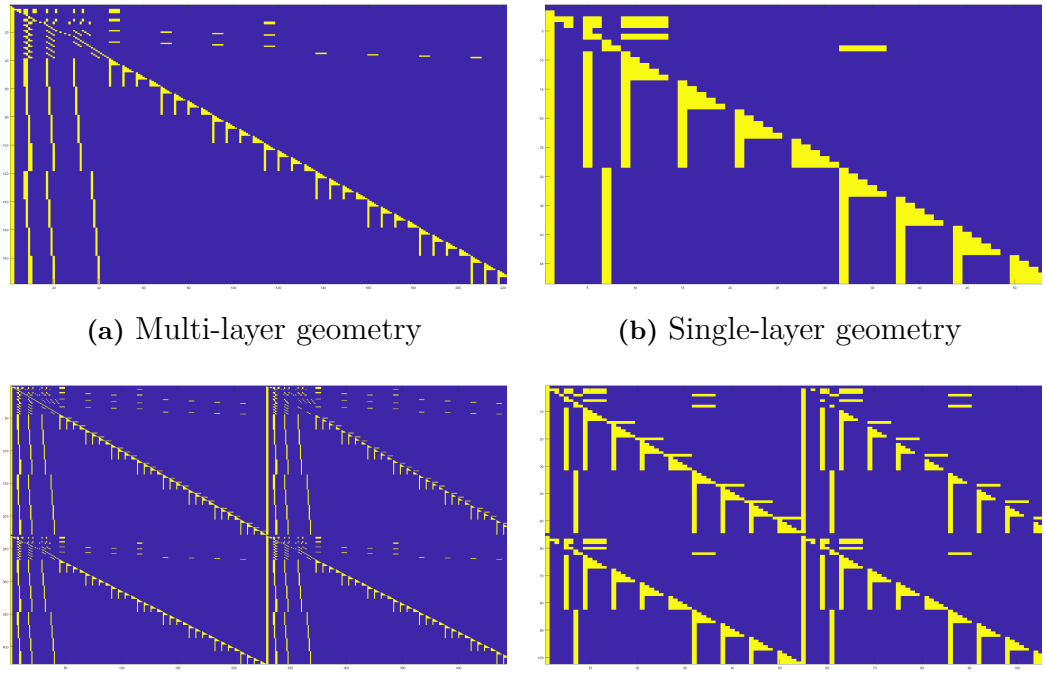

(a) Multi-layer geometry

(b) Single-layer geometry

(c) Multi-layer, interpolated

(d) Single-layer, interpolated

Figure 3.8: Visualizations of the pressure sum matrix $\mathbf{P}$ of size $|\mathcal{N}|x|\mathcal{C}|$

3.2.4 Heat Matrix Generation

Finally, for the purposes of determining the temperature T in the nodes $\mathcal{N}$ and connections $\mathcal{C}$, the heat matrix $\mathbf{H}$ of size $[|\mathcal{N}|,\ |\mathcal{N}|]$ is constructed by means of algorithm 5.

Algorithm 5 Generation of heat matrix $\mathbf{H}$

initialize $\mathbf{H}$ as $[|\mathcal{N}|,\ |\mathcal{N}|]$ zero matrix
initialize heat boundary $\vec{b^H}$ as $|\mathcal{N}|$ zero vector
$\vec{b^H} = -\vec{UA}\left(T_o - \vec{T}\right)$
————CONVECTION & CONDUCTION
for $i = 1, \ldots, |\mathcal{C}|$ **do**
    $\mathbf{H}_{S_i,T_i} = -\left(1 - \beta_i\right)\left(\rho c_p Q\right)_i + \left(k\frac{A}{L}\right)_i$, where β comes from equation 2.54
    $\mathbf{H}_{T_i,S_i} = \beta_i\left(\rho c_p Q\right)_i + \left(k\frac{A}{L}\right)_i$
    $\vec{b^H}_{S_i} = \vec{b^H}_{S_i} + \vec{p}_i$
    $\vec{b^H}_{T_i} = \vec{b^H}_{T_i} - \vec{p}_i$
end for
———WALL HEAT TRANSFER
if There exists nodes that have a cross-wall connection with another node **then**
    Let $\mathcal{J}$ be the set of nodes that cross-wall connect to an arbitrary node k_j.
    for $j \in \mathcal{J}$ **do**
        $\mathbf{H}_{j,k} = (UA)_{j,k}$
        where $UA_{j,k}$ is the effective heat transfer as per equation 2.57
        $\mathbf{H}_{k,j} = (UA)_{j,k}$
    end for
end if
———TRANSPORTIVE PROPERTY ASSURANCE
for $i = 1, \ldots, |\mathcal{N}|$ **do**
    $\mathbf{H}_{i,i} = \sum_j \mathbf{H}_{i,j}$
end for
———INLET BOUNDARY CONDITION
$\mathbf{H}_{n_i,n_i} = \mathbf{H}_{n_i,n_i} - \left(\rho c_p Q\right)_{n_i}$
$\vec{b^H}_{n_i} = \vec{b^H}_{n_i} - \left(\rho c_p Q\right)_{n_i} T_{n_i}$
———HEAT SOURCES
for $i = 1, \ldots, |\mathcal{N}|$ **do**
    $\vec{b^H}_i = \vec{b^H}_i - S_{h,i} V_i$
end for
Return $\mathbf{H}$ & $\vec{b^H}$

Once $\mathbf{H}$ is constructed, $\vec{T_n}$ can be solved as per equation 3.14. Since both $\mathbf{H}$ and $\vec{b^H}$ is dependent on $\vec{T_n}$, the equation needs to be solved iteratively in a similar manner to algorithm 3.

$$\mathbf{H}\vec{T_n} = \vec{b^H} \tag{3.14}$$

For a visualization of the Heat matrix for the four different cases displayed in figure 3.5, see figure 3.9. 0 is colored blue as per other images presented in similar style, while coefficients are colored according to a colorbar.

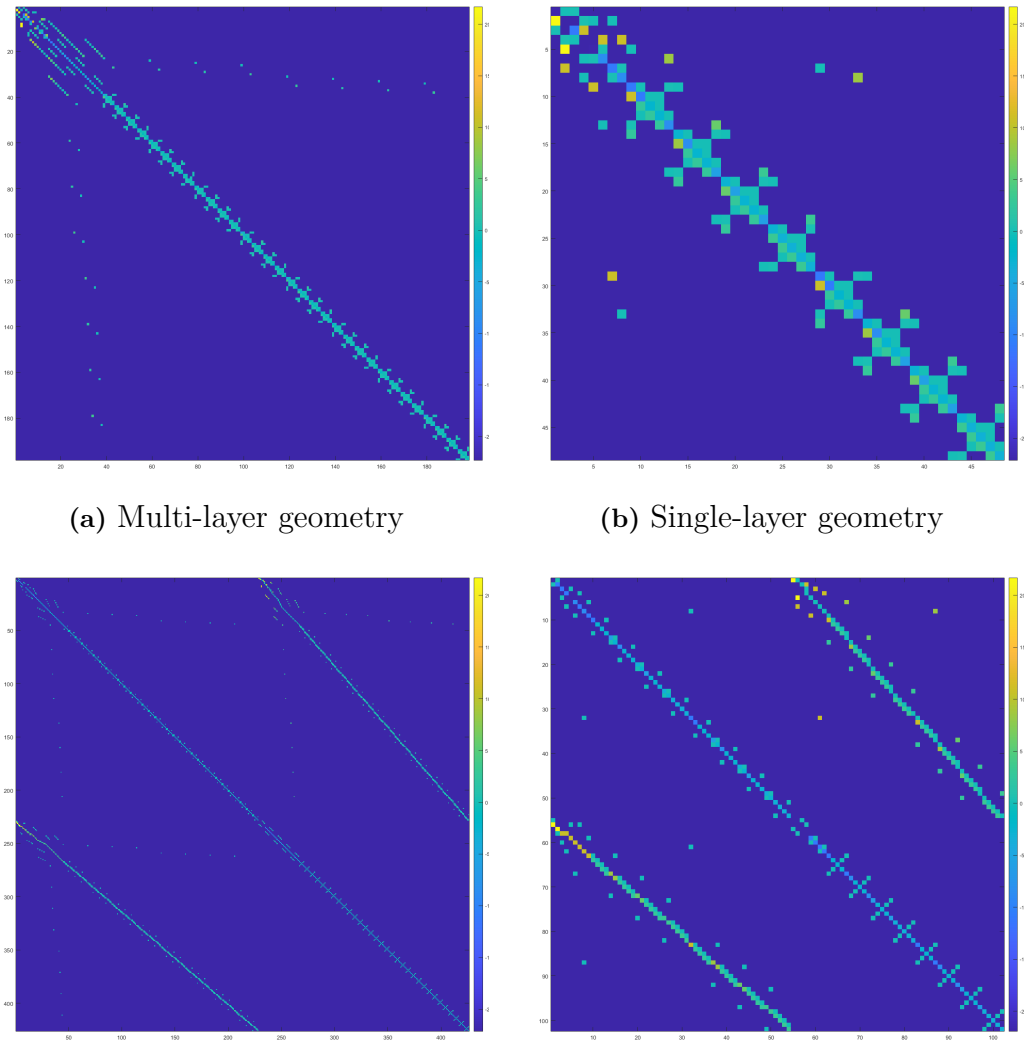

(a) Multi-layer geometry

(b) Single-layer geometry

(c) Multi-layer, interpolated

(d) Single-layer, interpolated

Figure 3.9: Visualizations of the heat matrix **H** of size $|\mathcal{N}|x|\mathcal{N}|$

3.3 Relaxation

This section covers the usage of relaxation in the solver in order to avoid non-terminating 'vibrating' solutions. Whenever an iteratively solved variable, such as $\rho\vec{Q}$, $\vec{T}$ and $\vec{p_n}$ is updated, the assignment

$$x_{old} \leftarrow x_{new} \tag{3.15}$$

is replaced by the relaxed assignment

$$x_{old} \leftarrow r \cdot x_{new} + (1 - r) \cdot x_{old} \tag{3.16}$$

where r is the iteration dependent relaxation factor, given partially in equation 3.17.

$$r_c(i) = r_c y^{iz} \tag{3.17}$$

As the temperature is looped internally, it's relaxation factor depends on the internal loop over j rather than the main loop over i. For an example of what this relaxation coefficient looks like when $y = 1 - 10^{-6}$ and $z = 2$, see figure 3.10

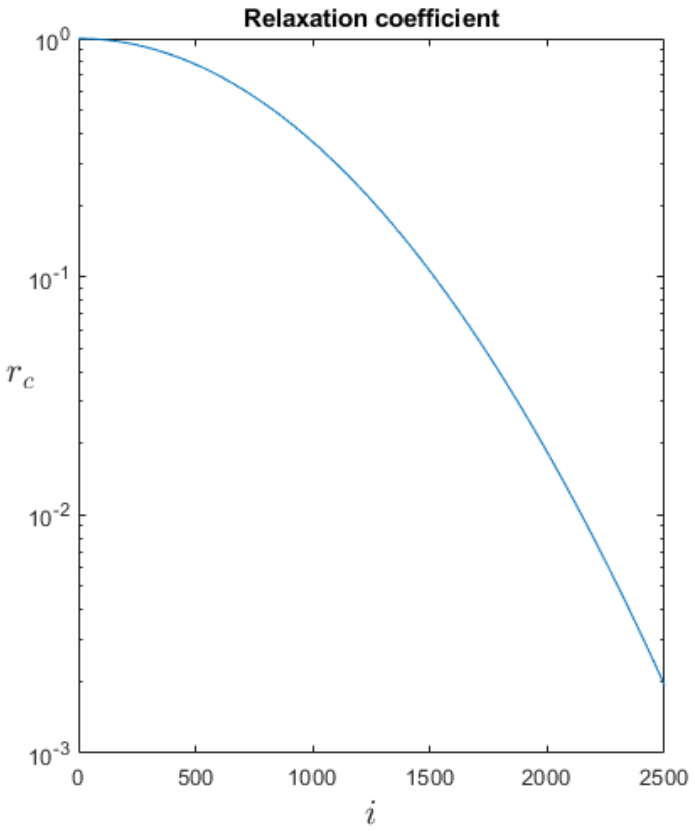

Figure 3.10: Relaxation coefficient for $y = 1 - 10^{-6}$ and $z = 2$

However, this alone does not prevent the possibility of the solution exploding, another issue which the solver might face. In order to regard this, the relaxation factor

is upwards limited by the pre-update error:

$$e_p = \sqrt{\max\left(\left(x_{new} - x_{old}\right)^2\right)}. \tag{3.18}$$

Such that

$$r = \min\left(r_c\left(i\right), \frac{1}{e_p}\right) \tag{3.19}$$

Meaning that in any one iteration, the maximum change $\max\left(x_{new} - x_{old}\right)$ can be no greater than 1.

3.4 Solver Implementation

This section aims to give an overview of how the solver is constructed. The general structure of the solver follows algorithm 6

3.4.1 Settings

A number of settings is available to the solver, as follows:

3.4.1.1 Solver Settings

- Number of iterations I
- Number of internal iterations J
- Tolerance level t
- Initial relaxation coefficient r_c
- Relaxation coefficient update rate y
- Relaxation coefficient update exponent z
- Number of iterations inbetween output message ΔI_{print}
- Number of iterations inbetween visualization ΔI_{draw}

3.4.1.2 Physics Settings

- Inlet Velocity V_{in} $(ms^{-}1)$
- Inlet Temperature T_{in} (K)
- Ambient Temperature T_{am} (K)
- Heat Source value S (W)

3.4.1.3 Override Settings

- Override outer heat transfer coefficient h_o $(Js^{-1}m^{-2}K^{-1})$
- Override density field ρ (kgm^{-3})
- Override flow field ρQ using Fluent data
- Override thermal conductivity k $(Js^{-1}m^{-1}K^{-1})$
- Override viscosity μ $(kgs^{-1}m^{-1})$
- Override specific heat capacity c_p (JK^{-1})
- Override inner heat transfer coefficient h_i $(Js^{-1}m^{-2}K^{-1})$

3.4.1.4 Display Settings

- Boolean: Write node values on graph
- Boolean: Write connection values on graph
- Boolean: Save data to file
- String: Value-path to color visuals by

3.4.2 Algorithm

Algorithm 6 Flow rate solver

Read material and solver settings
Read or Create Geometry G
Use G to form Adjacency Matrix $\mathbf{A}$
Calculate $\mathbf{F}$, $\mathbf{D}$ and $\mathbf{P}$ from $\mathbf{A}$, settings and G
Initialize values for all variables, such as $\rho\vec{Q}$, $\vec{T}$ and $\vec{p}_n$

for $i = 1, \ldots, I$ where I is the number of iterations to run **do**

    Update relaxation coefficient
    Update density ρ using latest information on $\vec{p}_n$ and $\vec{T}$
    Update Mass flow $\rho\vec{Q}$ by iterating once as per algorithm 3
    Update pressure $\vec{p_n}$ and $\vec{p_c}$ as per algorithm 4

    if Pressure, Mass flow and density error below tolerance value **then**
        for $j = 1, \ldots, J$ where J is the number of internal iterations **do**
            Update $\vec{T}$ as per algorithm 5
            if Temperature Error below tolerance **then**
                Break
            end if
        end for
    end if

    if All errors below tolerance **then**
        Break
    end if

end for
Draw Visuals
Save data

3.5 Test cases

This section covers the test cases used for validating the flow rate solver. In each test case, four variables are varied, these being the inlet temperature T_{in}, the ambient temperature T_A, the inlet velocity v_{in} and the heat sources S_hV.

3.5.1 Multiple layer geometry

This section presents the test cases used for the multiple layer geometry as seen in figure 3.1. These test cases were chosen to fulfill certain criteria, such as 'cooling' or 'warm-up from cold start' rather than any sort of full experimental design. This is partially motivated by a time limit on how many full scale fluent simulations could reliably be performed, since a full, 3-value experimental design for each variable would require 81 test cases.

Table 3.1: Test cases for the multiple layer geometry

Case	$T_{in}\,[K]$	$T_A\,[K]$	$v_{in}\,[ms^{-1}]$	$S_hV\ [W]$
1	20	50	20	0
2	20	50	10	0
3	20	50	10	200
4	20	50	5	0
5	30	0	20	0
6	30	0	10	0
7	30	0	10	200
8	30	0	5	0
9	40	-20	20	0
10	40	-20	10	0
11	40	-20	10	200
12	40	-20	5	0

3.5.2 Single layer geometry

This section presents the test cases used for the single layer geometry as seen in figure 3.3. Similarly to the full scale geometry, these were chosen to fulfill specific criteria rather than to embody a full scale experimental design.

Table 3.2: Test cases for the single layer geometry

Case	$T_{in}\,[C]$	$T_A\,[C]$	$v_{in}\,[ms^{-1}]$	$S_hV\ [W]$
1	20	50	2.5	0
2	30	0	2.5	0
3	30	0	5	0
4	30	0	2.5	200
5	40	-20	2.5	0

3.6 Fluent Comparison

This section covers the settings used in the fluent model for validation of the flow rate solver. All the models described within are taken from ANSYS FLUENT's theory guide [1]. The basis for the fluid flow models utilized in ANSYS is the mass conservation equation and the momentum conservation equation, as ANSYS presents them in equation 3.20 and equation 3.21. A velocity inlet condition with velocity dependent on the test case was assigned to the inlet of the interior at the lower end of the trunk and a pressure outlet condition assigned to the outlet of the exterior at the lower end of the trunk. All surfaces other than the inlet and outlet are regarded as no-slip walls for the purposes of the continuity and viscous transport equation.

$$\frac{\partial \rho}{\partial t} + \nabla \cdot (\rho \vec{v}) = S_m \tag{3.20}$$

Where S_m is a source term for mass added from non-continuous phases.

$$\frac{\partial}{\partial t}(\rho \vec{v}) + \nabla \cdot (\rho \vec{v}\vec{v}) = -\nabla p + \nabla \cdot \left(\bar{\bar{\tau}}\right) + \rho \vec{g} + \vec{F} \tag{3.21}$$

Where $\bar{\bar{\tau}}$ is the stress tensor given by equation 3.22, $\vec{F}$ is the external body forces and other source terms and $\vec{g}$ is the gravitational vector.

$$\bar{\bar{\tau}} = \mu \left[\left(\nabla \vec{v} + \nabla \vec{v}^T \right) - \frac{2}{3} \nabla \cdot \vec{v} I \right] \tag{3.22}$$

Where μ is the molecular viscosity and I is the unit tensor.

3.6.1 SST $k - \omega$

For capturing possible turbulent effects of the system, the Shear-Stress Transport (SST) $k - \omega$ model which includes transport of turbulence kinetic energy k and specific dissipation rate ω as seen in equation 3.28 and equation 3.39. The model acts as a blend between the $k - \omega$ model and the $k - \epsilon$ model by the use of blending functions F_1 and F_2 described in equations 3.23 and 3.26 respectively.

$$F_1 = \tanh\left(\Phi_1^4\right) \tag{3.23}$$

$$\Phi_1 = \min\left[\max\left(\frac{\sqrt{k}}{0.09\omega y}, \frac{500\mu}{\rho y^2 \omega}\right), \frac{4\rho k}{\sigma_{\omega,2} D_\omega^+ y^2}\right] \tag{3.24}$$

$$D_\omega^+ = \max\left[2\rho \frac{1}{\sigma_{\omega,2}} \frac{1}{\omega} \frac{\partial k}{\partial x_j} \frac{\partial \omega}{\partial x_j}, 10^{-10}\right] \tag{3.25}$$

$$F_2 = \tanh\left(\Phi_2^2\right) \tag{3.26}$$

$$\Phi_2 = \max\left[2\frac{\sqrt{k}}{0.09\omega y}, \frac{500\mu}{\rho y^2 \omega}\right] \tag{3.27}$$

Where y is the distance to the next surface and D_ω^+ is the positive component of the cross-diffusion term.

3.6.1.1 k transport equation

$$\frac{\partial}{\partial t}(\rho k) + \frac{\partial}{\partial x_i}(\rho k u_i) = \frac{\partial}{\partial x_j}\left(\Gamma_k \frac{\partial k}{\partial x_j}\right) + \bar{G}_k - Y_k + S_k \tag{3.28}$$

Where Γ_k is the effective diffusivity of k given by equation 3.29, G_k is the production of turbulence kinetic energy defined by equation 3.30, Y_k is the dissipation of k defined by equation 3.32 and S_k is any user defined source term.

$$\Gamma_k = \mu + \frac{\mu_t}{\sigma_k} \tag{3.29}$$

$$\bar{G}_k = \min\left(G_k, 10\rho\beta^* k\omega\right) \tag{3.30}$$

$$G_k = -\rho\overline{u_i' u_j'}\frac{\partial u_j}{\partial x_i} \tag{3.31}$$

$$Y_k = \rho\beta^* k\omega \tag{3.32}$$

Where σ_k is the turbulent Prandtl number for k as per equation 3.33 and μ_t is the turbulent viscosity as per equation 3.54 and β^* is given by equation 3.34

$$\sigma_k = \frac{1}{F_1/\sigma_{k,1} + (1 - F_1)/\sigma_{k,2}} \tag{3.33}$$

Where $\sigma_{k,1} = 1.176$ and $\sigma_{k,2} = 1$.

$$\beta^* = \beta_i^* \left[1 + \zeta^* F\left(\mathrm{M}_t\right)\right] \tag{3.34}$$

$$\beta_i^* = \beta_\infty^* \left(\frac{4/15 + \left(\mathrm{Re}_t/R_\beta\right)^4}{1 + \left(\mathrm{Re}_t/R_\beta\right)^4}\right) \tag{3.35}$$

Where $\beta_\infty^* = 0.09$, $R_\beta = 8$, $\zeta^* = 1.5$ and $F(\mathrm{M}_t)$ is the compressibility function given by equation 3.36

$$F\left(\mathrm{M}_t\right) = \begin{cases} 0 & \mathrm{M}_t \leq \mathrm{M}_{t0} \\ \mathrm{M}_t^2 - \mathrm{M}_{t0}^2 & \mathrm{M}_t > \mathrm{M}_{t0} \end{cases} \tag{3.36}$$

Where $\mathrm{M}_t^2 = \frac{2k}{a^2}$, $\mathrm{M}_{t0} = 0.25$ and $a = \sqrt{\gamma RT}$

$$f_{\beta^*} = \begin{cases} 1 & \chi_k \leq 0 \\ \frac{1+680\chi_k^2}{1+400\chi_k^2} & \chi_k > 0 \end{cases} \tag{3.37}$$

Where χ_k is given by equation 3.38

$$\chi_k = \frac{1}{\omega^3}\frac{\partial k}{\partial x_j}\frac{\partial \omega}{\partial x_j} \tag{3.38}$$

3.6.1.2 ω transport equation

$$\frac{\partial}{\partial t}(\rho\omega) + \frac{\partial}{\partial x_i}(\rho\omega u_i) = \frac{\partial}{\partial x_j}\left(\Gamma_\omega \frac{\partial \omega}{\partial x_j}\right) + \bar{G}_\omega - Y_\omega + D_\omega + S_\omega \tag{3.39}$$

Where Γ_ω is the effective diffusivity of k given by equation 3.40, G_ω is the production of ω given by equation 3.41, Y_ω is the dissipation of the specific dissipation rate given by equation 3.42, D_ω is the cross diffusion term calculated as per equation 3.43 and S_ω is a user defined source term.

$$\Gamma_\omega = \mu + \frac{\mu_t}{\sigma_\omega} \tag{3.40}$$

$$G_\omega = \frac{\rho\alpha}{\mu_t}\bar{G}_k \tag{3.41}$$

$$Y_\omega = \rho\beta\omega^2 \tag{3.42}$$

$$D_\omega = 2(1 - F_1)\rho\sigma_{\omega,2}\frac{1}{\omega}\frac{\partial k}{\partial x_j}\frac{\partial \omega}{\partial x_j} \tag{3.43}$$

Where σ_ω is the Prandtl number for ω as per equation 3.44, α is a relaxation factor given by equation 3.45 and β is given by equation 3.49.

$$\sigma_\omega = \frac{1}{F_1/\sigma_{\omega,1} + (1 - F_1)/\sigma_{\omega,2}} \tag{3.44}$$

Where $\sigma_{\omega,1} = 2$ and $\sigma_{\omega,2} = 1.168$

$$\alpha = \frac{\alpha_\infty}{\alpha^*}\left(\frac{\alpha_0 + \mathrm{Re}_t/R_k}{1 + \mathrm{Re}_t/R_k}\right) \tag{3.45}$$

Where α_∞ is defined in equation 3.46 and $\alpha_0 = \frac{1}{9}$

$$\alpha_\infty = F_1\alpha_{\infty,1} + (1 - F_1)\alpha_{\infty,2} \tag{3.46}$$

$$\alpha_{\infty,1} = \frac{\beta_{i,1}}{\beta^*_\infty} - \frac{\kappa^2}{\sigma_{\omega,1}\sqrt{\beta^*_\infty}} \tag{3.47}$$

$$\alpha_{\infty,2} = \frac{\beta_{i,2}}{\beta^*_\infty} - \frac{\kappa^2}{\sigma_{\omega,2}\sqrt{\beta^*_\infty}} \tag{3.48}$$

$$\beta = \beta_i\left[1 - \frac{\beta^*_i}{\beta_i}\zeta^* F(\mathrm{M}_t)\right] \tag{3.49}$$

$$\beta_i = F_1\beta_{i,1} + (1 - F_1)\beta_{i,2} \tag{3.50}$$

Where $\beta_{i,1} = 0.075$ and $\beta_{i,2} = 0.0828$.

$$f_\beta = \frac{1 + 70\chi_\omega}{1 + 80\chi_\omega} \tag{3.51}$$

Where χ_ω is given by equation 3.52

$$\chi_\omega = \left|\frac{\Omega_{ij}\Omega_{jk}S_{ki}}{(\beta^*_\infty\omega)^3}\right| \tag{3.52}$$

$$\Omega_{ij} = \frac{1}{2}\left(\frac{\partial u_i}{\partial x_j} - \frac{\partial u_j}{\partial x_i}\right) \tag{3.53}$$

3.6.1.3 Turbulent viscosity

The turbulent viscosity is calculated as follows:

$$\mu_t = \frac{\rho k}{\omega} \frac{1}{\max\left[\frac{1}{\alpha^*}, \frac{SF_2}{a_1 \omega}\right]} \tag{3.54}$$

Where α^* is a dampening coefficient given by equation 3.55, S is the strain rate magnitude and $a_1 = 0.31$

$$\alpha^* = \alpha^*_\infty \left(\frac{\alpha^*_0 + \mathrm{Re}_t/R_k}{1 + \mathrm{Re}_t/R_k}\right) \tag{3.55}$$

$$\mathrm{Re}_t = \frac{\rho k}{\mu \omega} \qquad R_k = 6 \qquad \alpha^*_0 = \frac{\beta_i}{3} \qquad \beta_i = 0.072 \tag{3.56}$$

Where $\alpha^*_\infty = 1$.

3.6.2 Energy equation

The standard energy equation provided by ANSYS FLUENT as seen in equation 3.57 served as the basis for validating the temperature of the flow, utilizing coupled boundary conditions for the interior walls and convective boundary conditions for the exterior walls with a fixed free-stream heat transfer coefficient of 5 $\frac{W}{m^2 \cdot K}$, a wall thickness of 2 mm, no shell conduction and varied inlet and ambient temperature as per the previously mentioned test cases. Heat sources were assigned to the interior fluid volumes of the cylinders that served as the interfaces between the interior pipes and the exterior pipes, given in Wm^{-3} such that the total energy added in each box was 200 W.

$$\frac{\partial}{\partial t}(\rho E) + \nabla \cdot (\vec{v}(\rho E + p)) = \nabla \cdot \left(k_{eff} \nabla T - \sum_j h_j \vec{J}_j + \left(\bar{\bar{\tau}}_{eff} \cdot \vec{v}\right)\right) + S_h \tag{3.57}$$

Where E is the energy, defined here as per equation 3.58

$$E = h - \frac{p}{\rho} + \frac{v^2}{2} \tag{3.58}$$

Where h is the sensible enthalpy defined for ideal gases as per equation 3.59

$$h = \sum_j Y_j h_j \tag{3.59}$$

Where Y_j is the mass fraction of j and h_j is defined as per equation 3.60

$$h_j = \int_{T_{ref}}^{T} c_{p,j} dT \tag{3.60}$$

Where $T_{ref} = 298.15$ K

$$S_h = \frac{S_i}{V_c} \tag{3.61}$$

Where S_i is the relevant heat source for the test case and V_c is the volume of the box in question.

3.7 Data sampling for validation

This section covers the method used to perform validation given the results from the flow solver and the fluent data. The main object of comparison between the two solvers being the mass flow into each separate box, the average temperature in the box and the pressure drop over the box. In order to acquire this data, it needs to be extracted from ANSYS FLUENT and MATLAB respectively.

From ANSYS FLUENT, the mass flow was extracted using the mass flow result calculation tool on the internal surface that served as the inlet into the box. The outlet from the box was found to have the same value, as was expected, and as such it was deemed valid. The temperature was extracted as a volume average of the total temperature field in the internal box fluid volume, the same one to which the heat source is applied. The pressure was extracted as two surface averages over the inlet and outlet to the box respectively, which was then subtracted on a per box basis in post processing.

From MATLAB, mass flow data was extracted per box as the mass flow of the inlet connection for that specific box (which is likewise equivalent to the mass flow of the outlet connection for that specific box). The temperature was taken as simply the temperature value of the box node, which is like the ANSYS FLUENT case, where the heat source is applied. The pressure was taken as the difference between the pressure in the inlet connection and the outlet connection for each respective box.

Additionally, in order to ensure the validation is relevant, the flow solvers settings were set such that they mirrored the ANSYS FLUENT settings to the greatest available extent. These settings can be seen in table 3.3

Table 3.3: Validation constants

Constant	Value (Air)	Value (Aluminum)	Unit
Density ρ	1.225	2719	kg/m^3
Specific heat capacity c_p	1006.43	871	J/kgK
Thermal conductivity k	0.0242	202.4	$/mK$
Outer heat transfer coefficient h_o	5	5	W/m^2K

4

Results

4.1 Fluent Results

Herein, an overview of selected results produced through ANSYS fluent is presented. With an overview of how a typical velocity, temperature and pressure field was found to behave for both the multiple layer geometry and the single layer geometry presented.

4.1.1 Velocity

This section presents the typical velocity field for a test case, with the images in question produced from post processing of case 6 of the multiple layer geometry and case 4 of the single layer geometry respectively. Figure 4.1 presents a contour overview of the velocity magnitude through the system, seen from two different axis in order to provide a better overview.

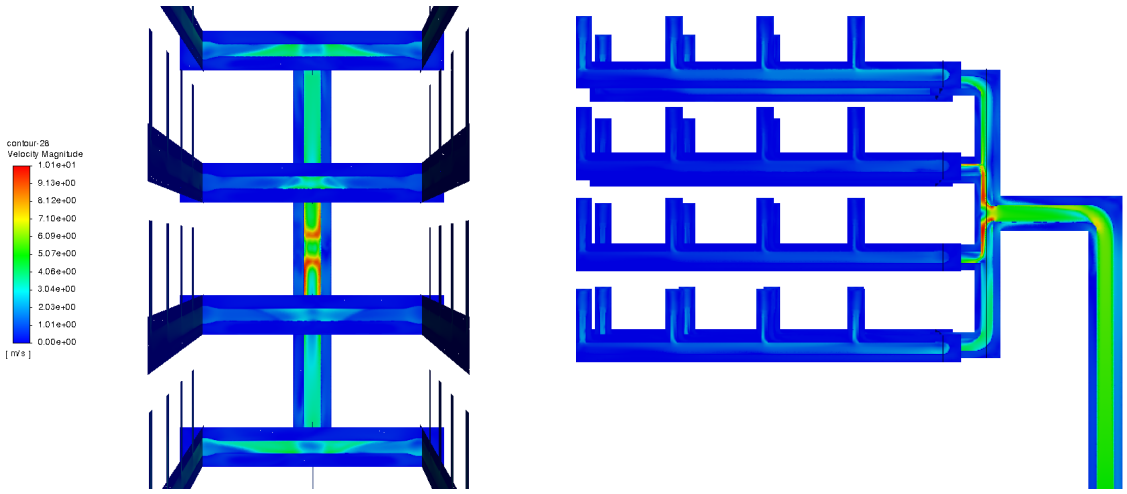

(a) Front View **(b)** Side View

Figure 4.1: Contour plot of fluent velocity field

Figure 4.2-4.4 presents a number of vector plots generated from from different parts of the trunk and the initial split from which the fluid runs to and from the different

layers where the differing behavior between the trunk curve, T-junctions and bends are visible.

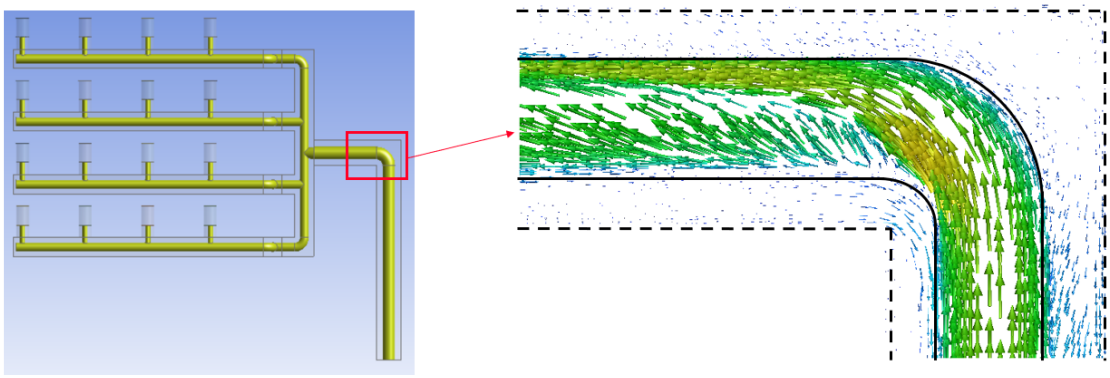

Figure 4.2: Vector plot of the trunk bend

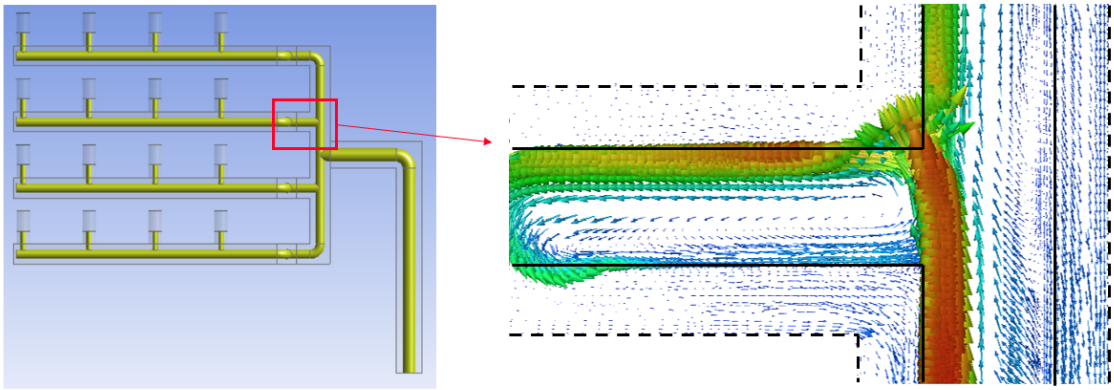

Figure 4.3: Vector plot of divider T-junction

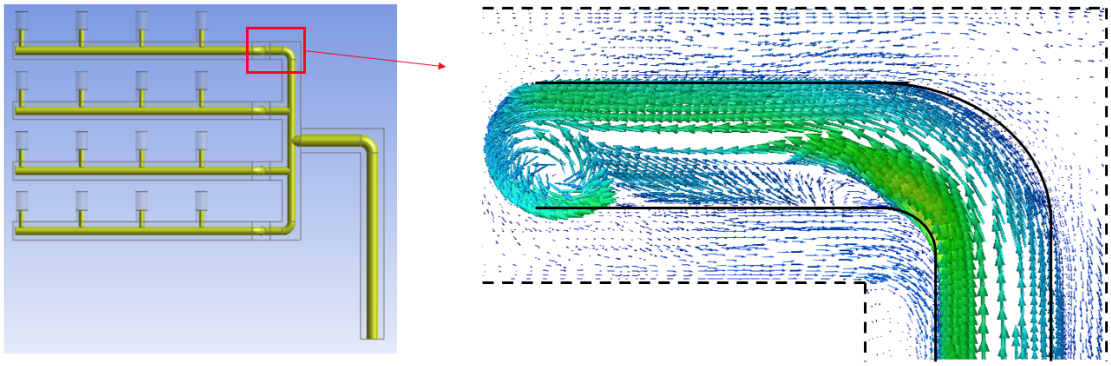

Figure 4.4: Vector plot of divider bend

Figure 4.5-4.6 presents vector plots generated from observation of a singular arm of the full-scale geometry, specifically observing the part of the arm where the fluid

diverges from the straight pipe to enter a box, either through a t-junction or through a bend, as the fluid does once it reaches the very last box on the arm.

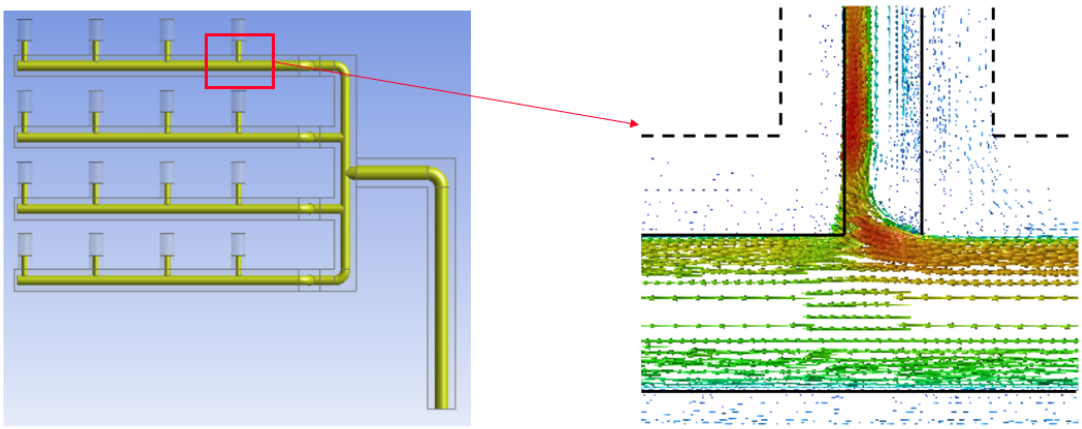

Figure 4.5: Vector plot of arm T-junction

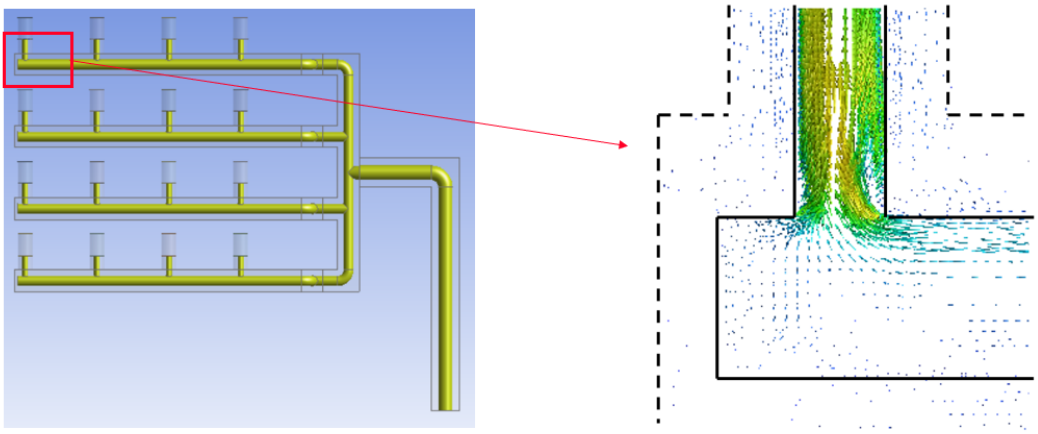

Figure 4.6: Vector plot of arm bend

In order to demonstrate the helical nature of the flow that was found during the fluent simulation, figure 4.7 presents two path-line traces observed at the point where the trunk splits into the different layers, and at the later arm split. Sub-figure (a) presents only the incoming flow, while sub-figure (b) also includes the returning flow.

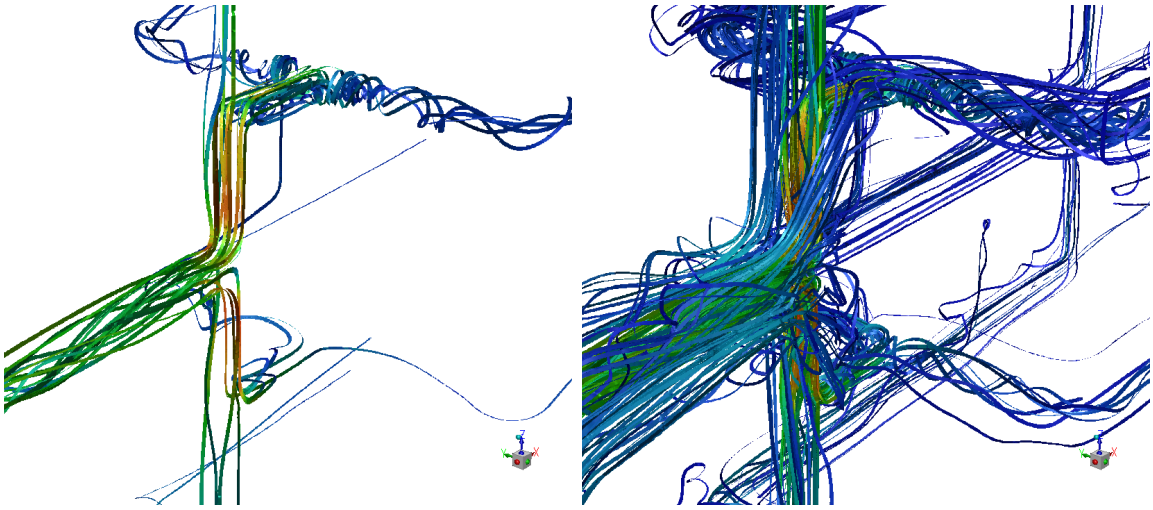

(a) Ingoing Trace **(b)** Returning Trace

Figure 4.7: Path-line plot of fluent velocity field

4.1.1.1 Single Layer

For the single-layer geometry, the velocity field has a more visible symmetry, as observed in figure 4.8, which presents a top and side view of the contour of the velocity magnitude for single layer test case 4.

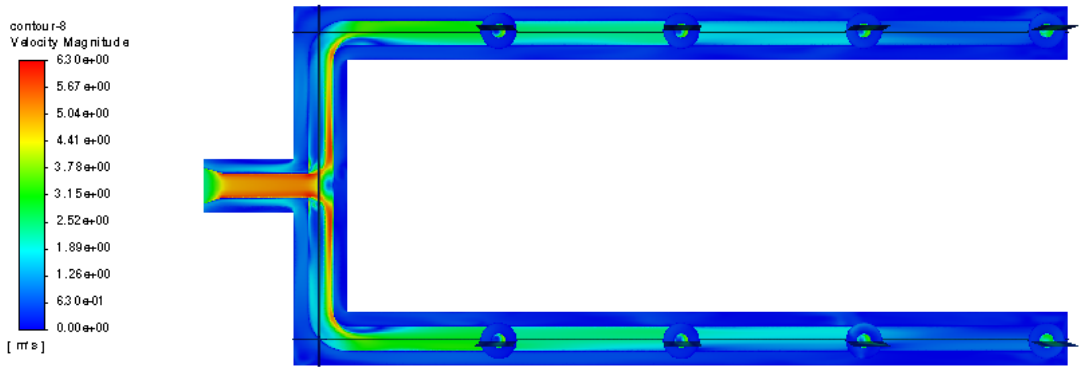

(a) Top View

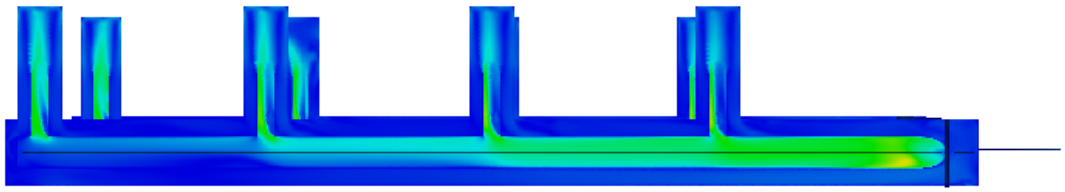

(b) Side View

Figure 4.8: Contour plot of fluent velocity field for the single layer geometry

Figure 4.9 shows a path-line trace of the velocity field for the single layer geometry. Visible, although not to a greater extent, is the lack of helical structures in the incoming (primarily green) flow, although the helical structures reappear in the returning (primarily blue) flow.

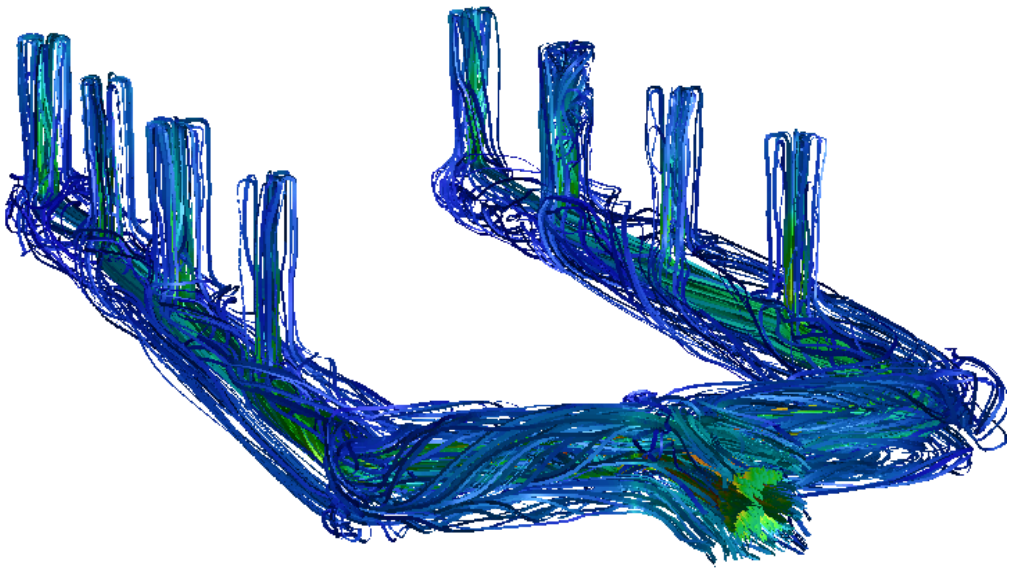

Figure 4.9: Path-line plot of fluent velocity field for single layer geometry

4.1.2 Temperature

The follow sections contains observed results regarding the temperature fields in a selected case for the multiple layer geometry and single geometry respectively, produced using ANSYS FLUENT. Figure 4.10 presents a contour of the temperature field for the multiple layer geometry seen from two different views. Of note is the visibly lower temperature in the third layer compared to the second from the bottom. Additionally, several asymmetries can be noted in the front view, particularly in the z-direction within each layer in the returning flows.

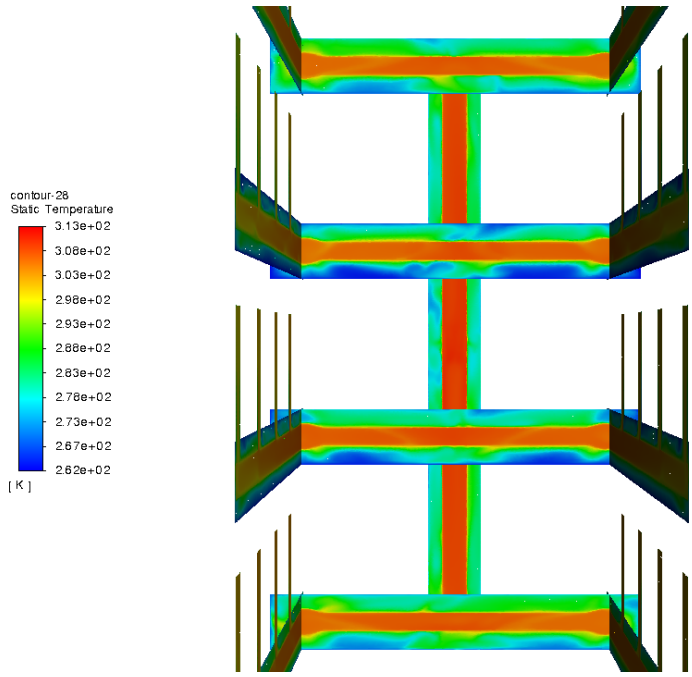

(a) Front View

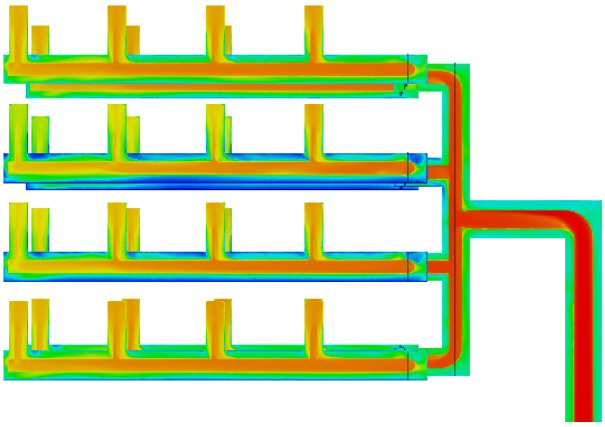

(b) Side View

Figure 4.10: Contour plot of fluent temperature field

4.1.2.1 Single Layer

Figure 4.11 presents a single layer geometry temperature contour, similarly to the velocity field, it appears on visual inspection as entirely symmetrical.

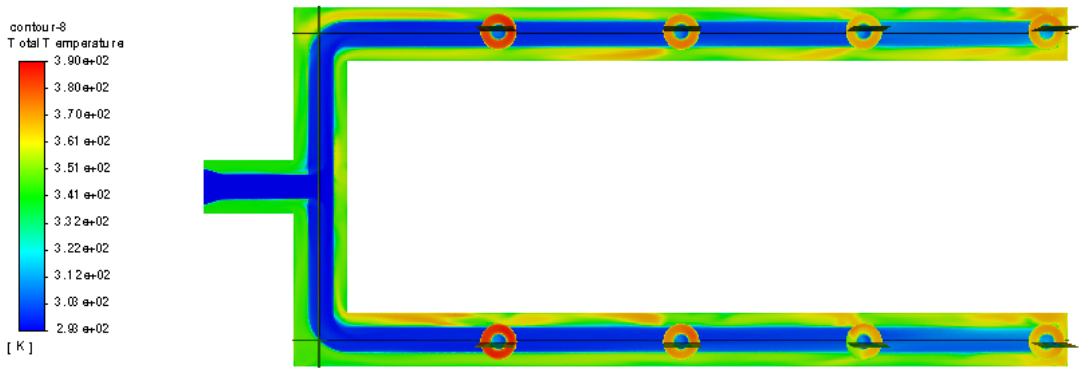

(a) Top View

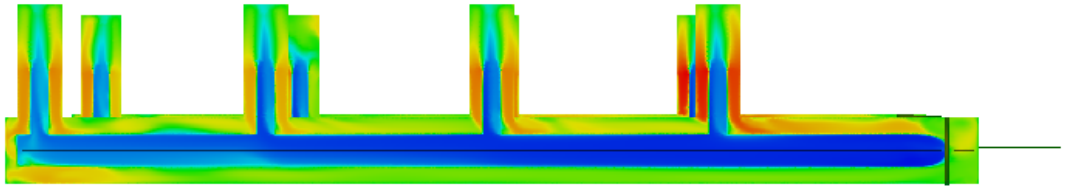

(b) Side View

Figure 4.11: Contour plot of fluent temperature field for single layer geometry

4.1.3 Pressure

The follow sections contains observed results regarding the pressure fields in a selected case for the multiple layer geometry and single layer geometry respectively, produced using ANSYS FLUENT. Figure 4.12 shows a contour of the pressure field for the multiple layer geometry, with the different layers differing in pressure primarily due to the presence of gravity. Otherwise the field remains predictably analogous to the velocity field.

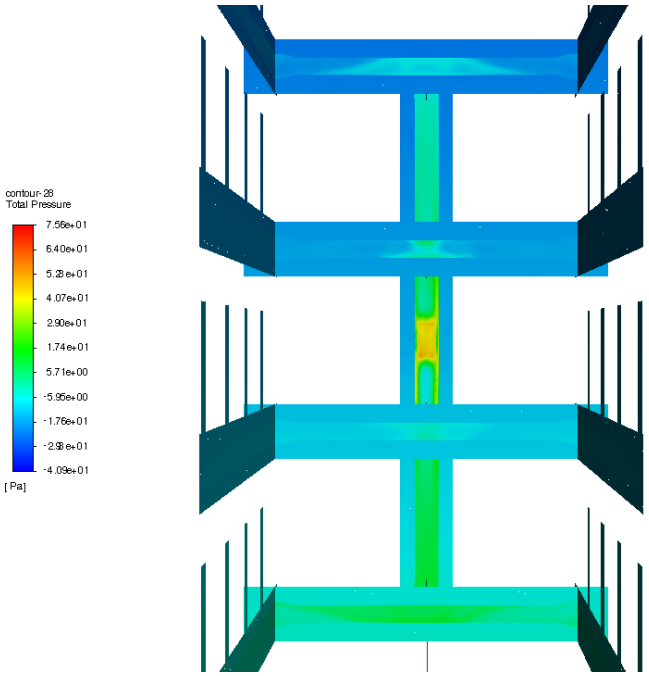

(a) Front View

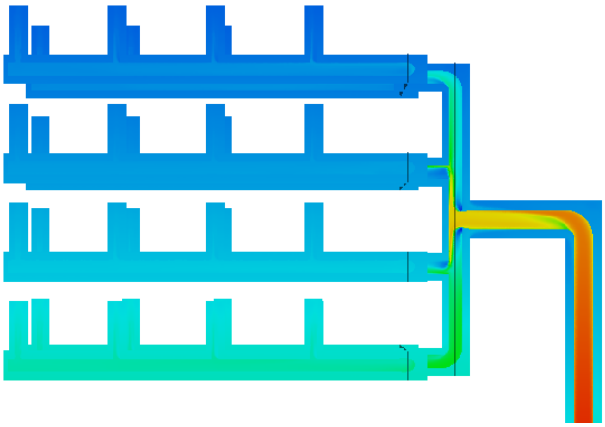

(b) Side View

Figure 4.12: Contour plot of fluent pressure field

4.1.3.1 Single Layer

Figure 4.13 shows a contour of the pressure field for the single layer geometry, the only gravitational difference that can be reliably observed here is the ascent into the boxes, otherwise displaying a dropping pressure in the x-directions with a significant pressure drop upon the entering enlarging pipe area of the box.

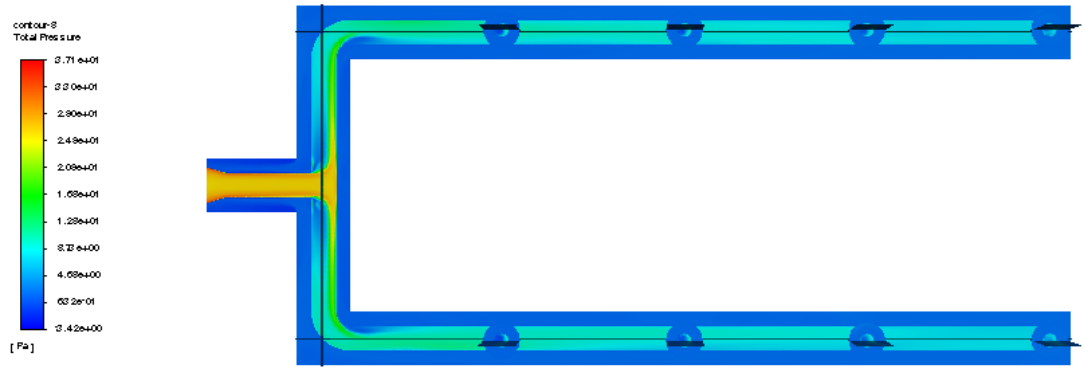

(a) Top View

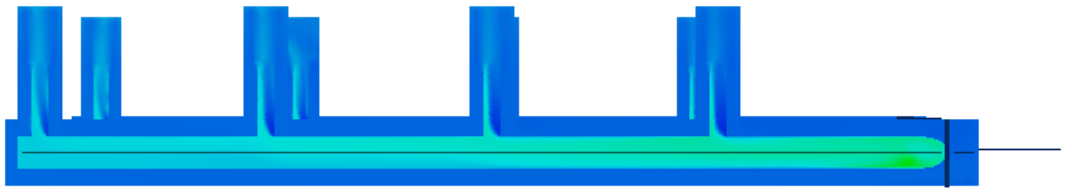

(b) Side View

Figure 4.13: Contour plot of fluent pressure field for single layer geometry

4.2 Validation Error Comparision

This section presents the comparisons calculated between the ANSYS FLUENT simulations and the flow solver created in MATLAB. When layers and boxes are referenced in the graphs in this section, refer to figure 4.14 for information on what the different layers and indexes or boxes in said layers entail.

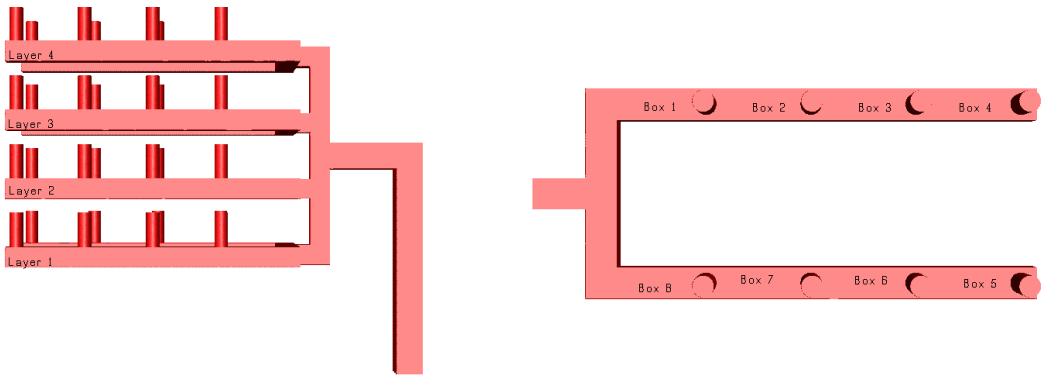

(a) Layer Structure **(b)** Box Structure

Figure 4.14: Indication of layer and box structure

Additionally, the table of test cases is repeated here for ease of access for multiple layer geometries. Not all of the cases here are presented in the following sections, instead, a selected few are presented, having been chosen to demonstrate particular findings. Similar results for all cases are available in the appendix.

Table 4.1: Reference table for full-scale test cases

Case	$T_{in}\,[K]$	$T_A\,[K]$	$v_{in}\,[ms^{-1}]$	$S_hV\ [W]$
1	20	50	20	0
2	20	50	10	0
3	20	50	10	200
4	20	50	5	0
5	30	0	20	0
6	30	0	10	0
7	30	0	10	200
8	30	0	5	0
9	40	-20	20	0
10	40	-20	10	0
11	40	-20	10	200
12	40	-20	5	0

Finally, when Total Pressure Drop is referenced in figures 4.17 it is calculated in as per equation 4.1.

$$\Delta p_{total} = \vec{p}_{Inlet} - \vec{p}_{Outlet} \tag{4.1}$$

Where $\vec{p}$ is the vector of pressures in the flow solver. Additionally, mass flow is expressed in kg/s. Temperature is expressed in K and pressure drop in Pa in all following graphs.

4.2.1 Case 1

Figure 4.15-4.17 presents the error calculations for mass flow, temperature and pressure for case one, a high velocity cooling case with no active heat sources. Temperature error is consistently negative, indicating that the flow rate solver predicts a less effective cooling than ANSYS FLUENT for this specific case. The pressure error behaves erratically, and is thus omitted from any further cases, as it provides no interesting information for discussion.

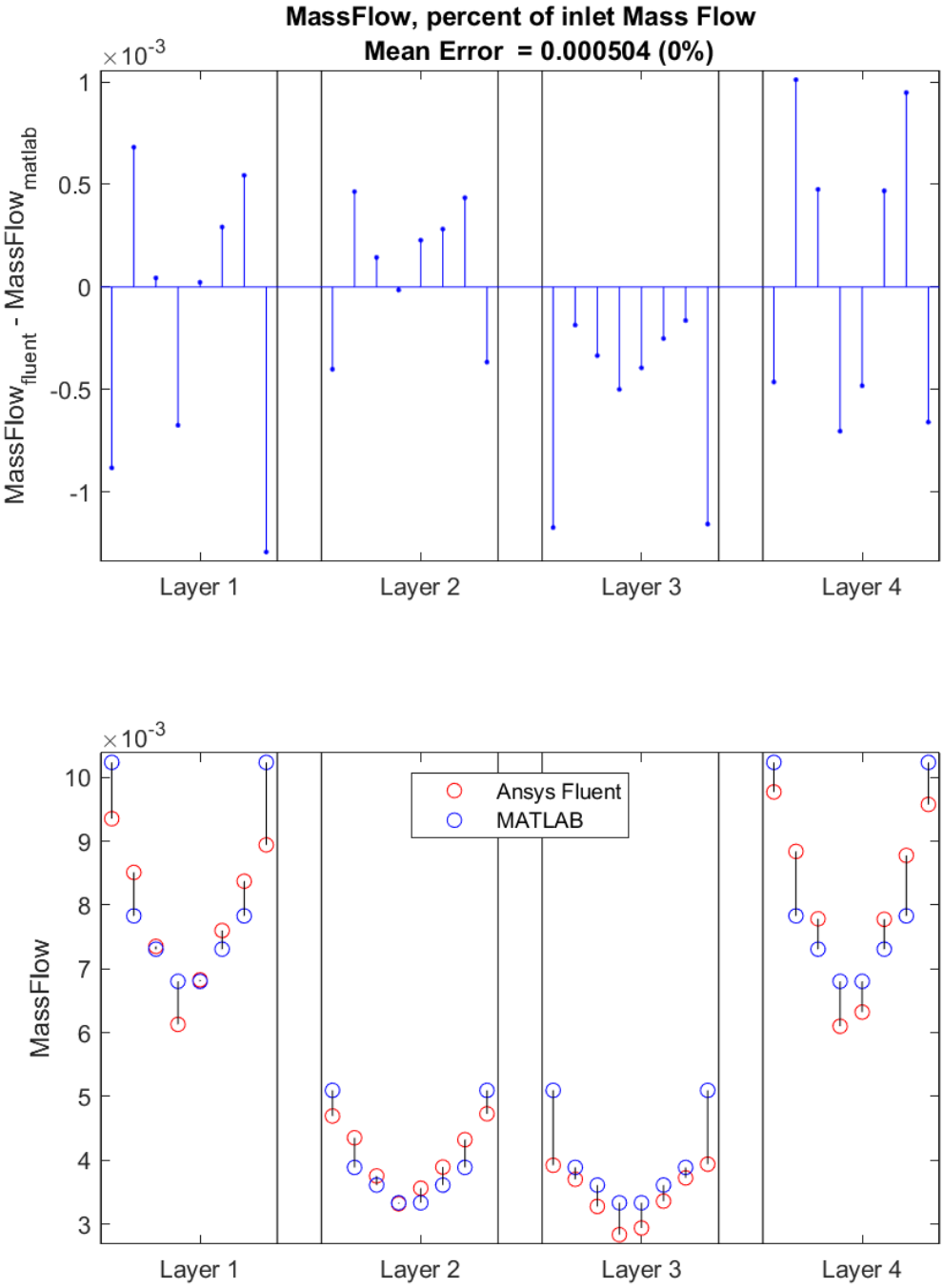

Figure 4.15: Mass Flow Error Plots for case 1

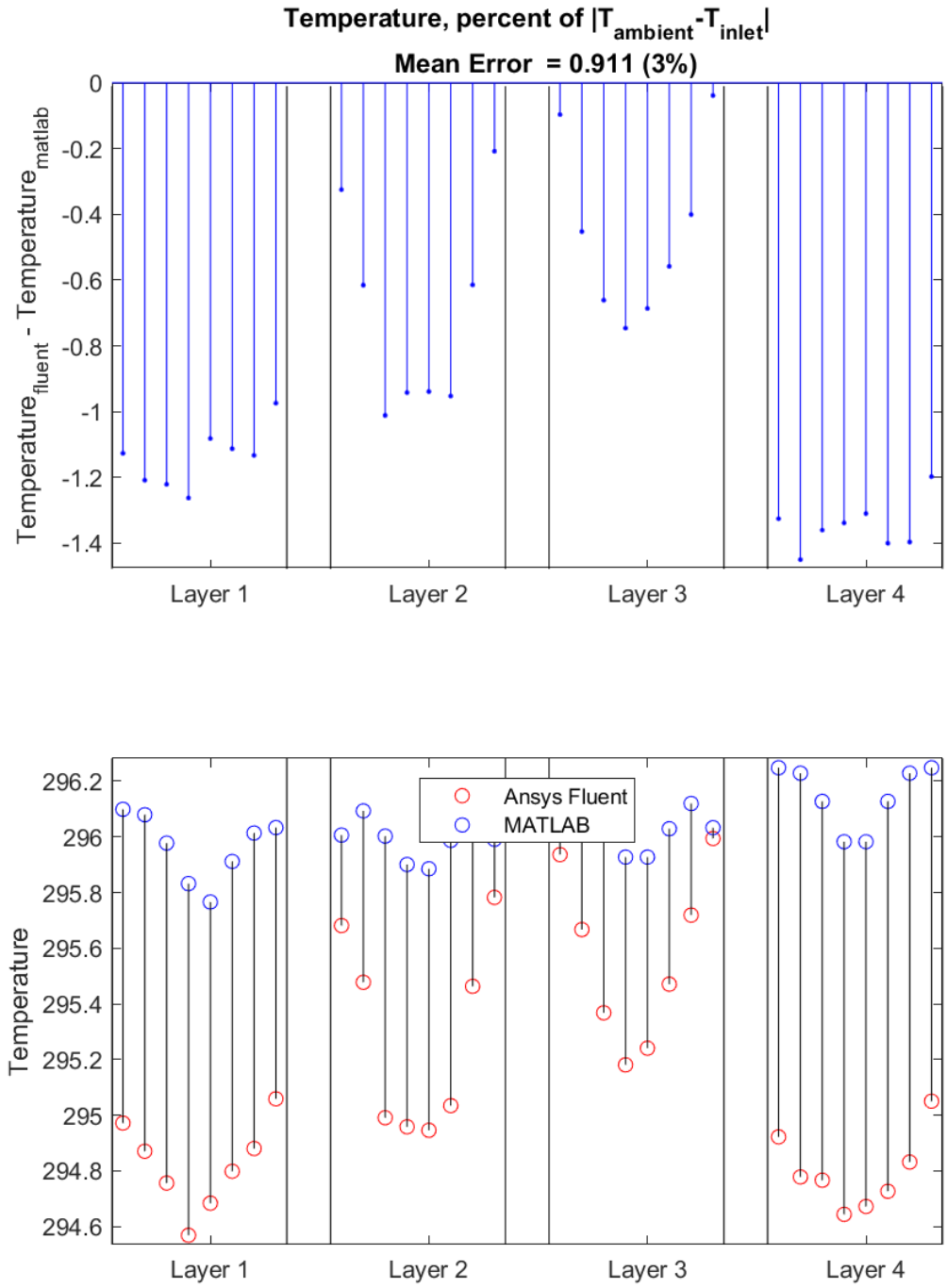

Figure 4.16: Temperature Error Plots for case 1

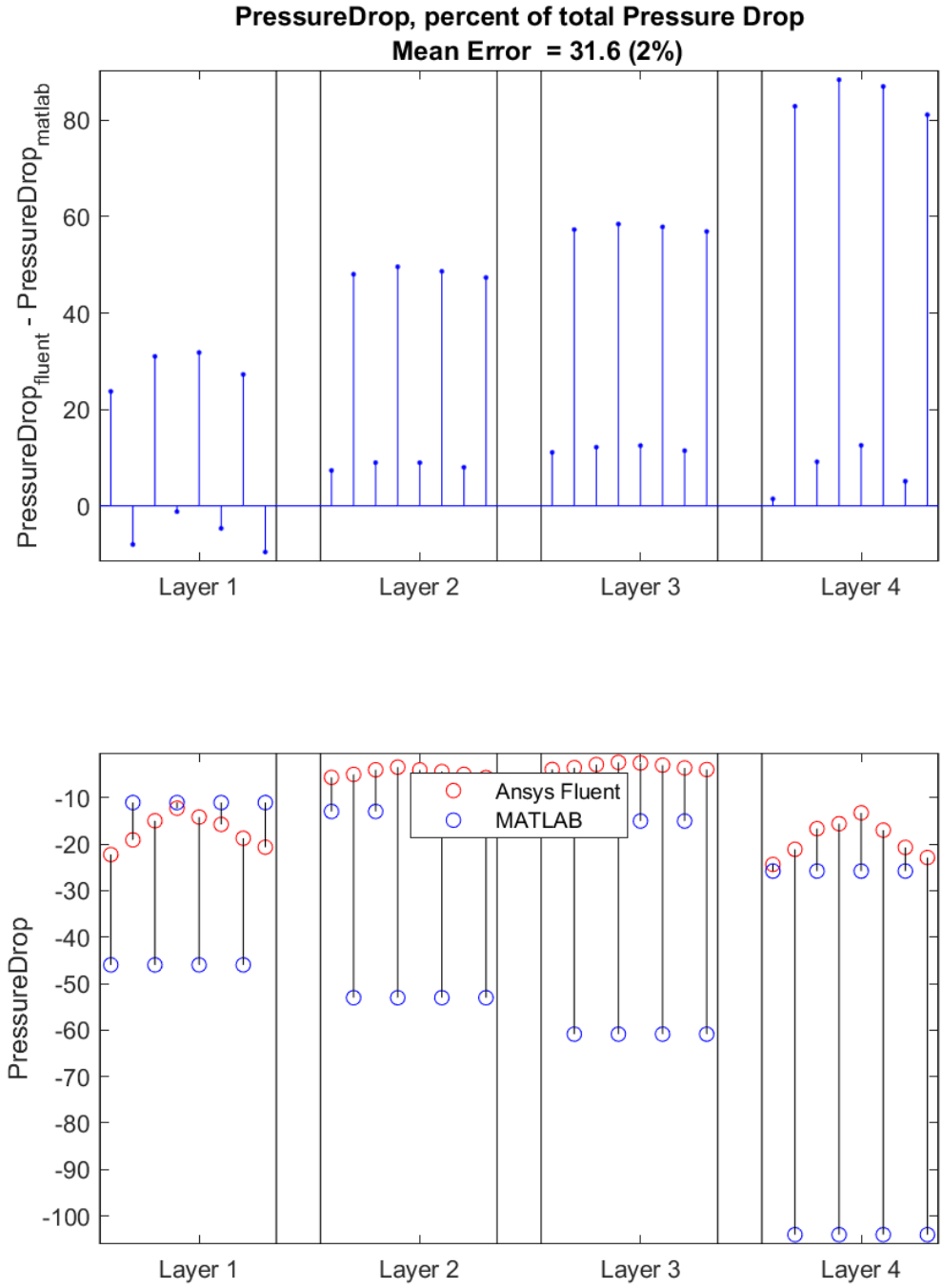

Figure 4.17: Pressure Error Plots for case 1

4.2.2 Case 2

Figure 4.18-4.19 presents the error calculations for mass flow, temperature and pressure for case two, a medium velocity cooling case with no active heat sources. Tem-

perature error is not consistently positive or negative like in case 1.

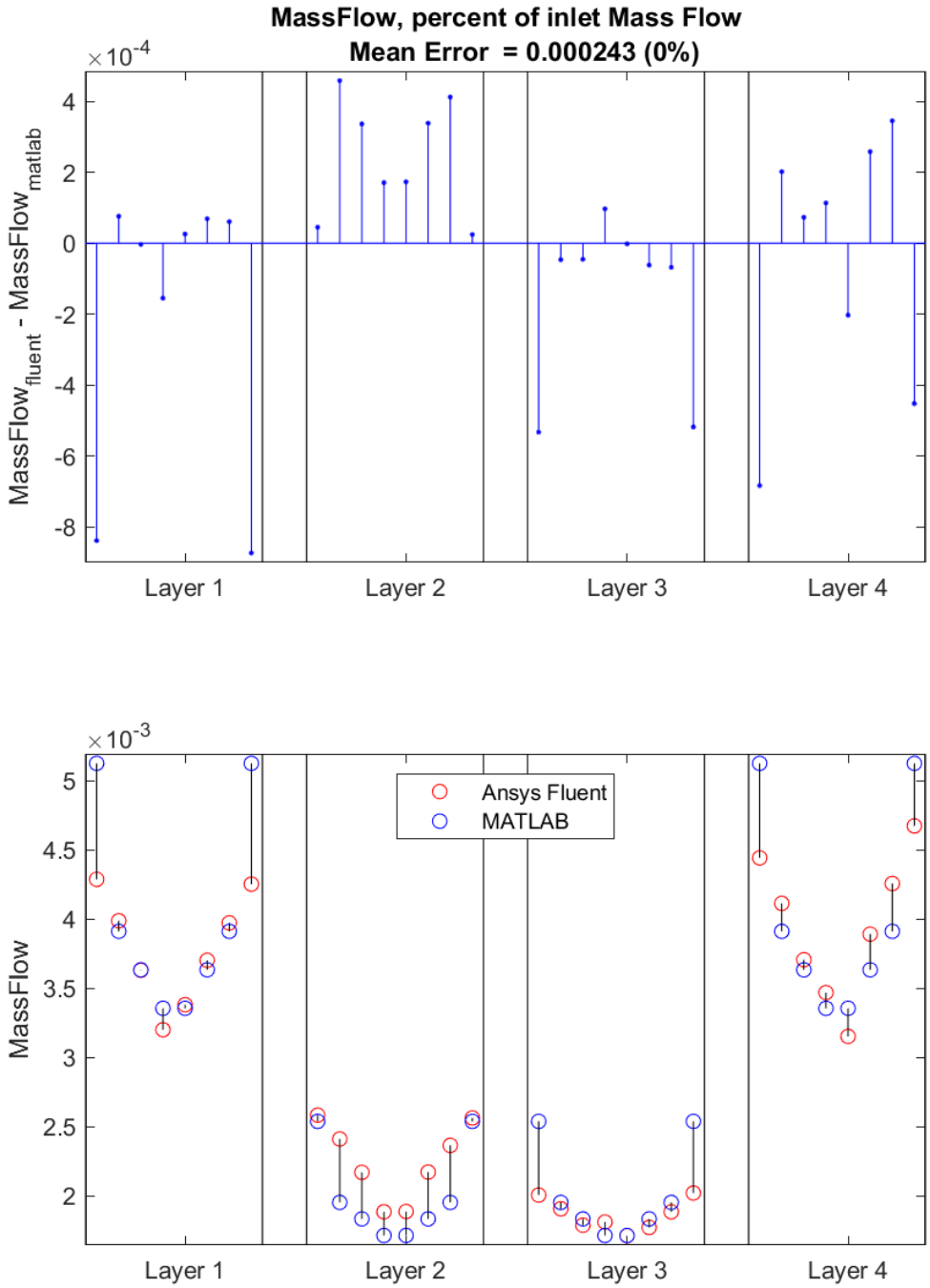

Figure 4.18: Mass Flow Error Plots for case 2

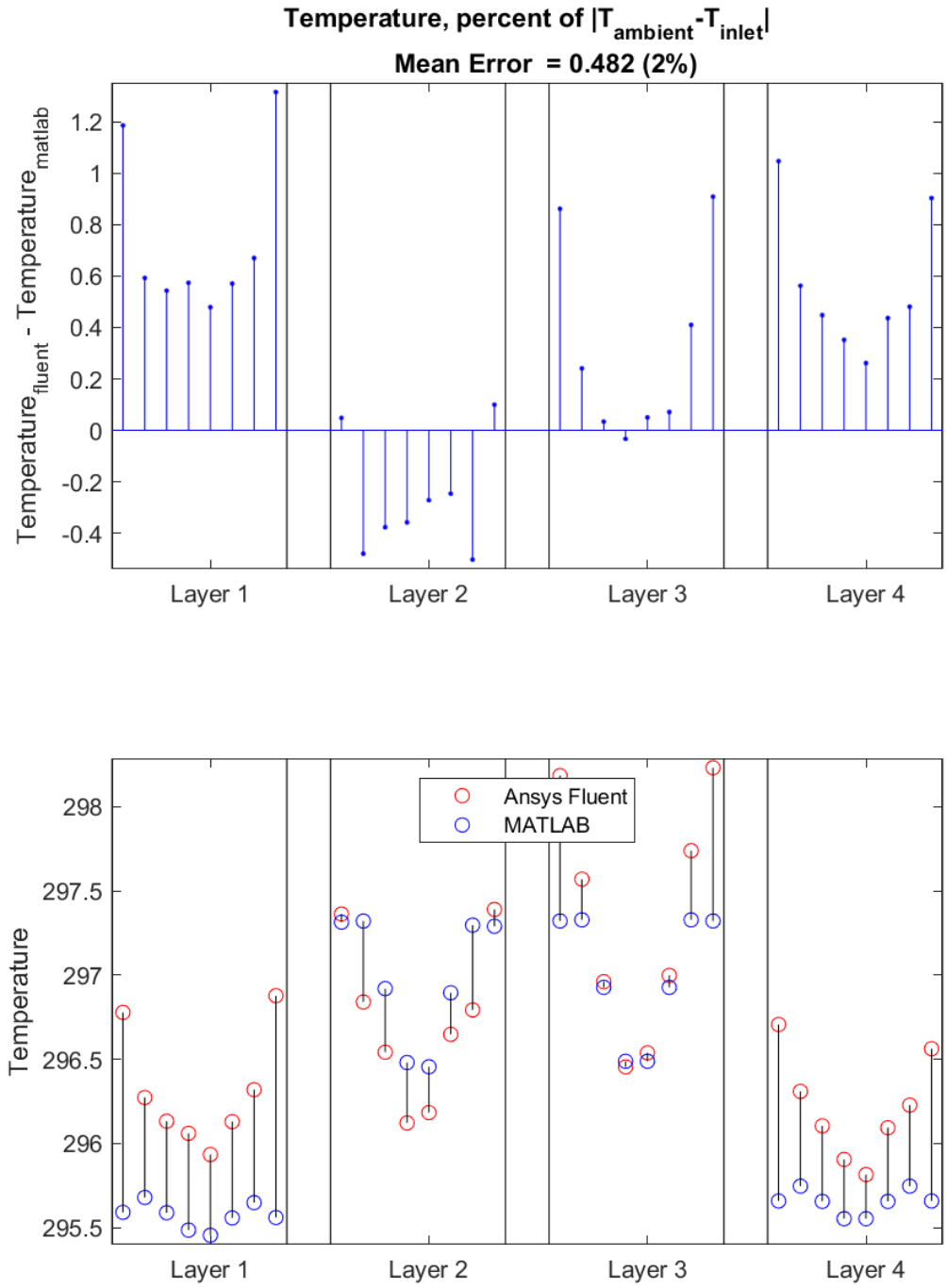

Figure 4.19: Temperature Error Plots for case 2

4.2.3 Case 3

Figure 4.20-4.21 presents the error calculations for mass flow, temperature and pressure for case three, a medium velocity cooling case with active heat sources. Tem-

perature error here is notably larger than in prior cases.

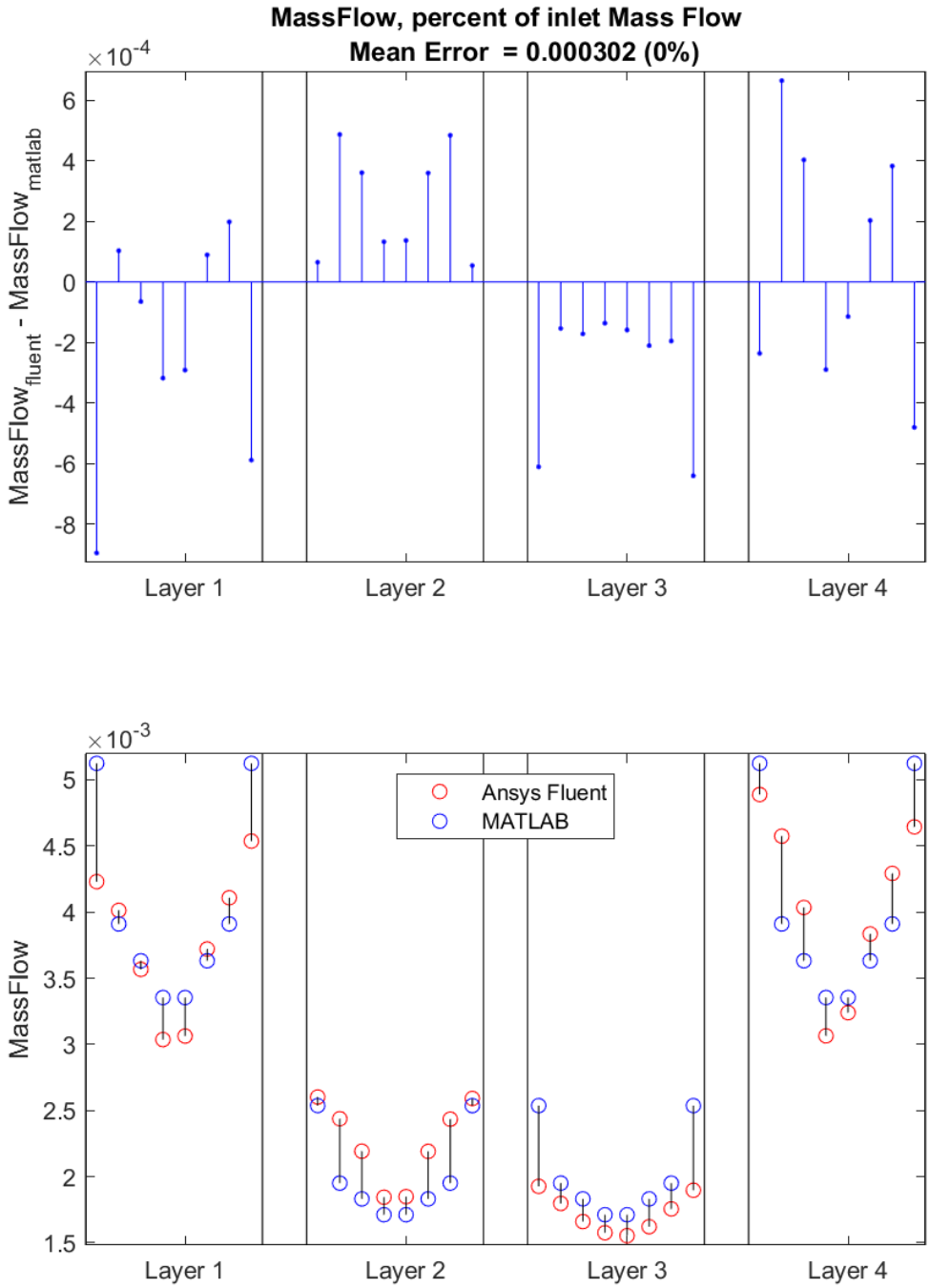

Figure 4.20: Mass Flow Error Plots for case 3

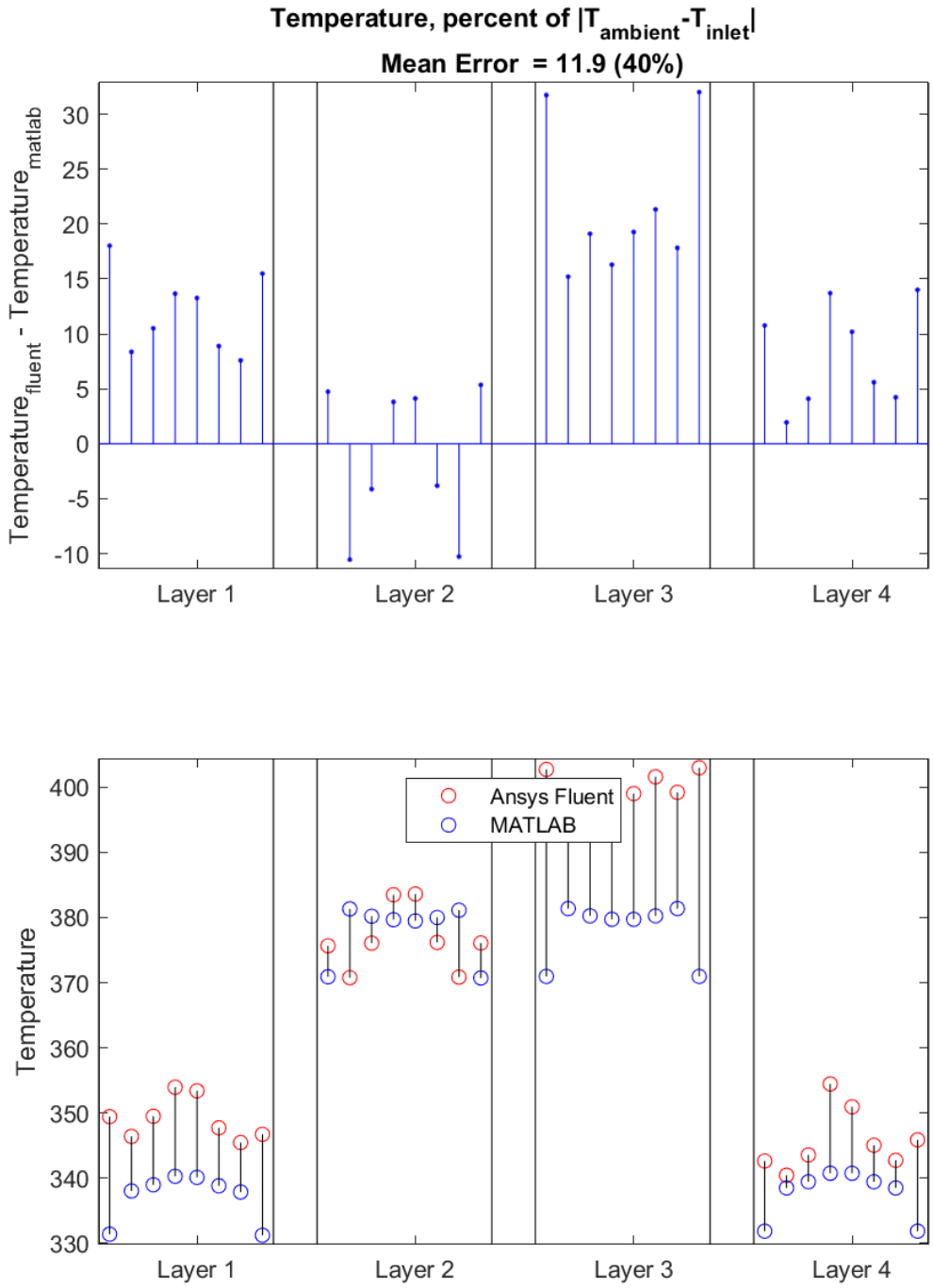

Figure 4.21: Temperature Error Plots for case 3

4.2.4 Case 4

Figure 4.22-4.23 presents the error calculations for mass flow, temperature and pressure for case 4, a low velocity cooling case with no active heat sources. Temperature

error rises here compared to medium and high velocity cases while flow error linearly decreases with inlet velocity.

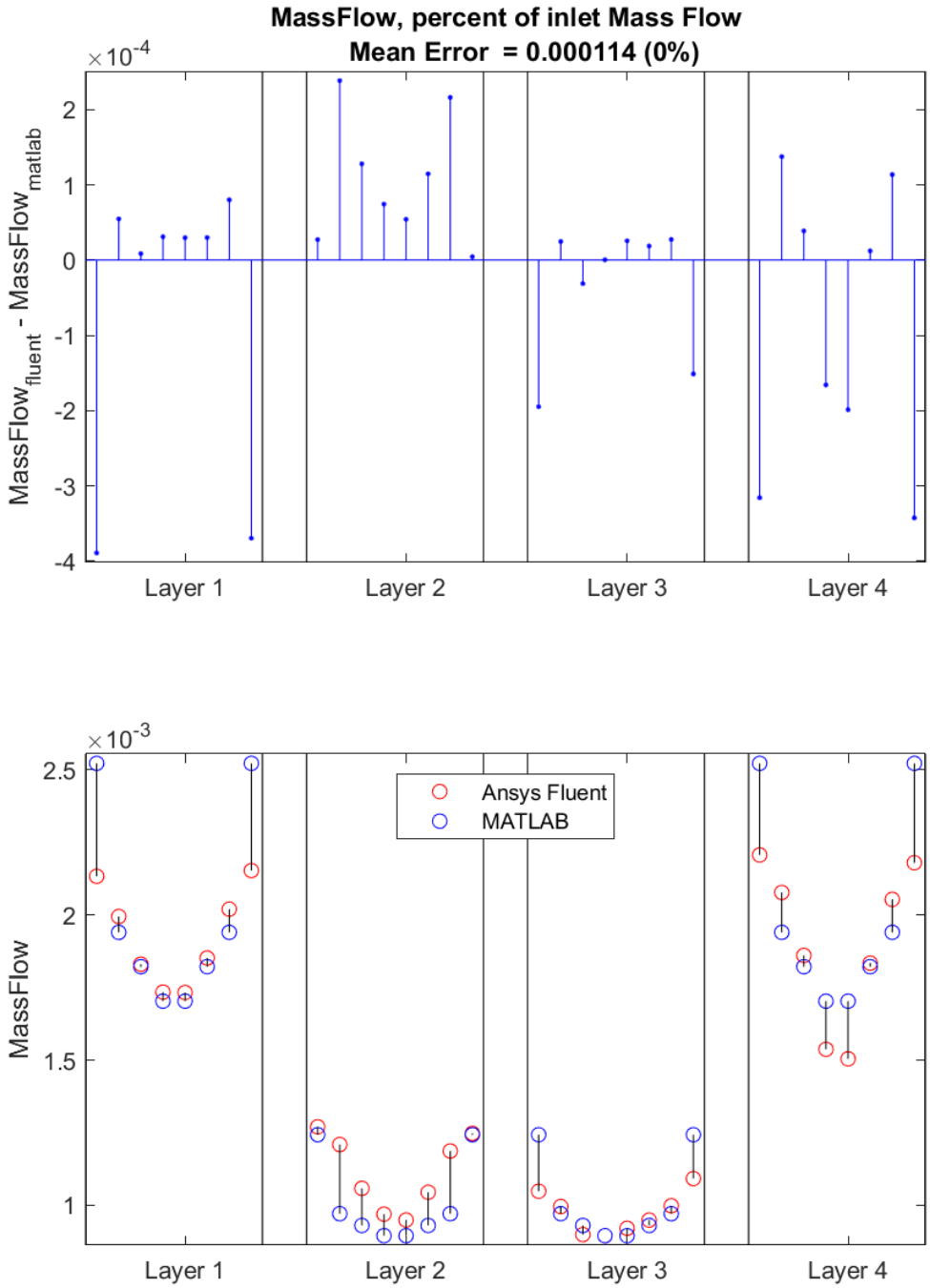

Figure 4.22: Mass Flow Error Plots for case 4

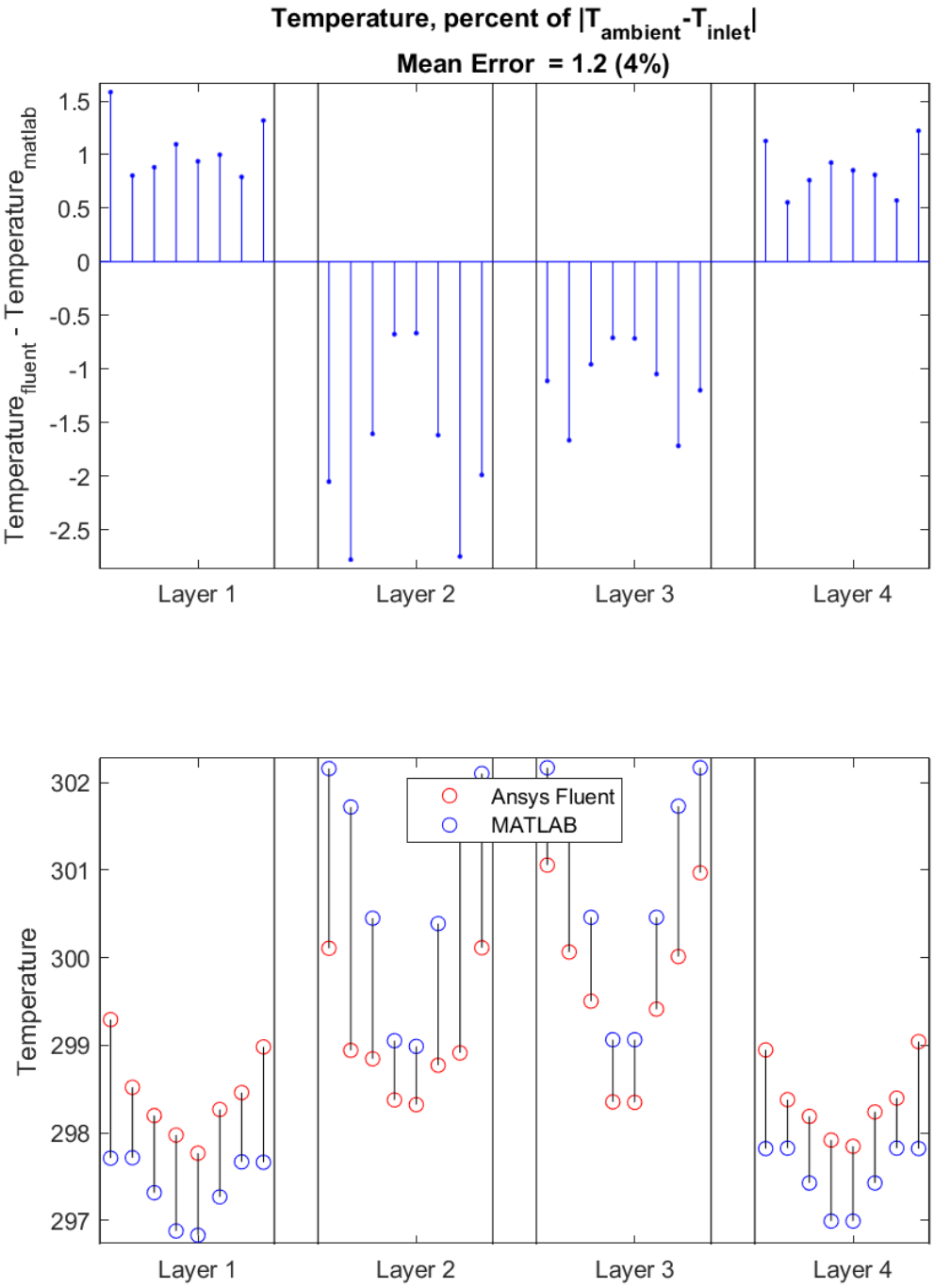

Figure 4.23: Temperature Error Plots for case 4

4.2.5 Case 7

Figure 4.24-4.25 presents the error calculations for mass flow and temperature for case 7, a medium velocity heating case with active heat sources. The temperature

error remains high even with lower flow error compared to case 3, points to an asymmetry arising in ANSYS FLUENT, as the MATLAB flow rate solver produced, with constant density, symmetrical values.

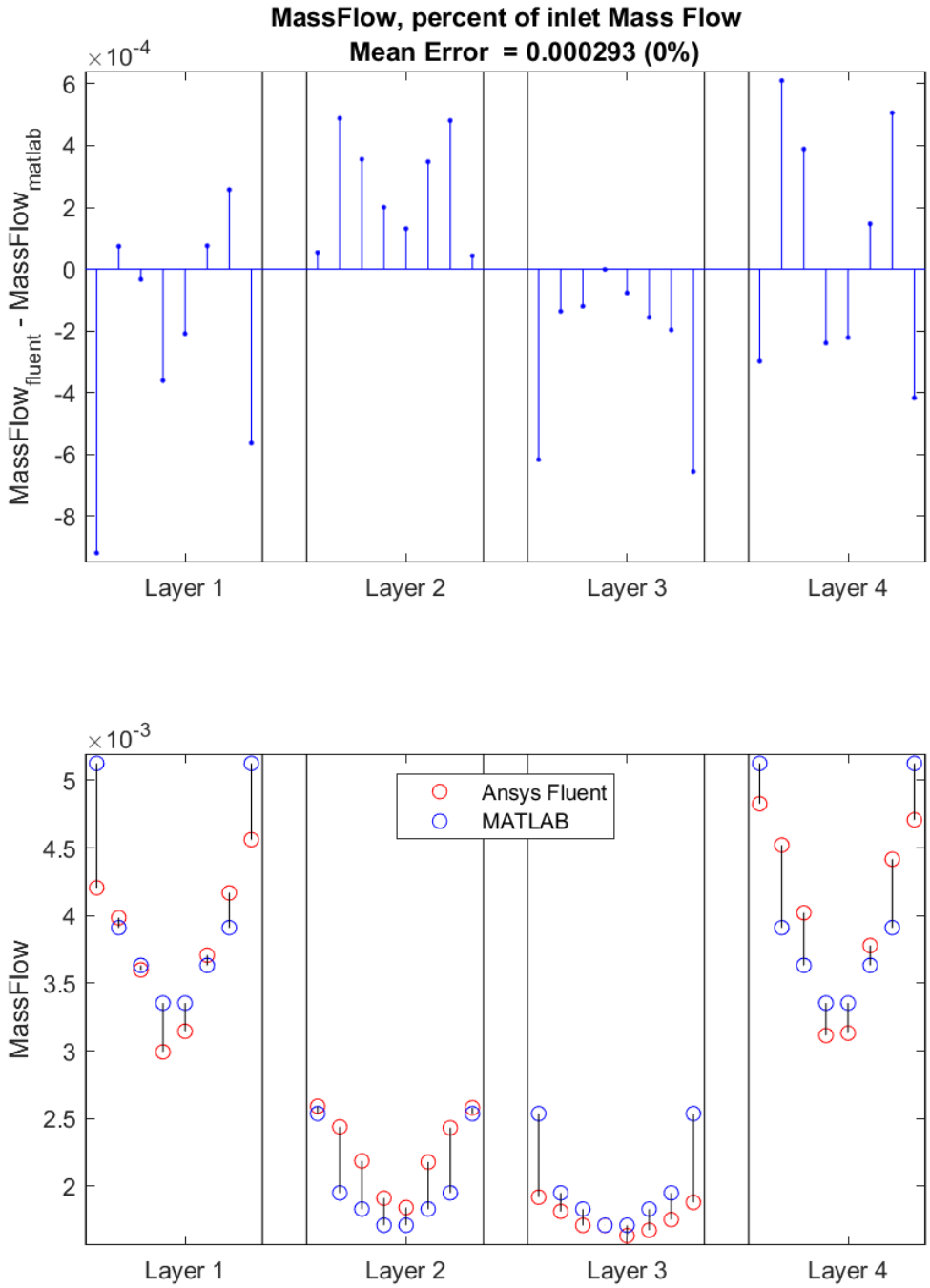

Figure 4.24: Mass Flow Error Plots for case 7

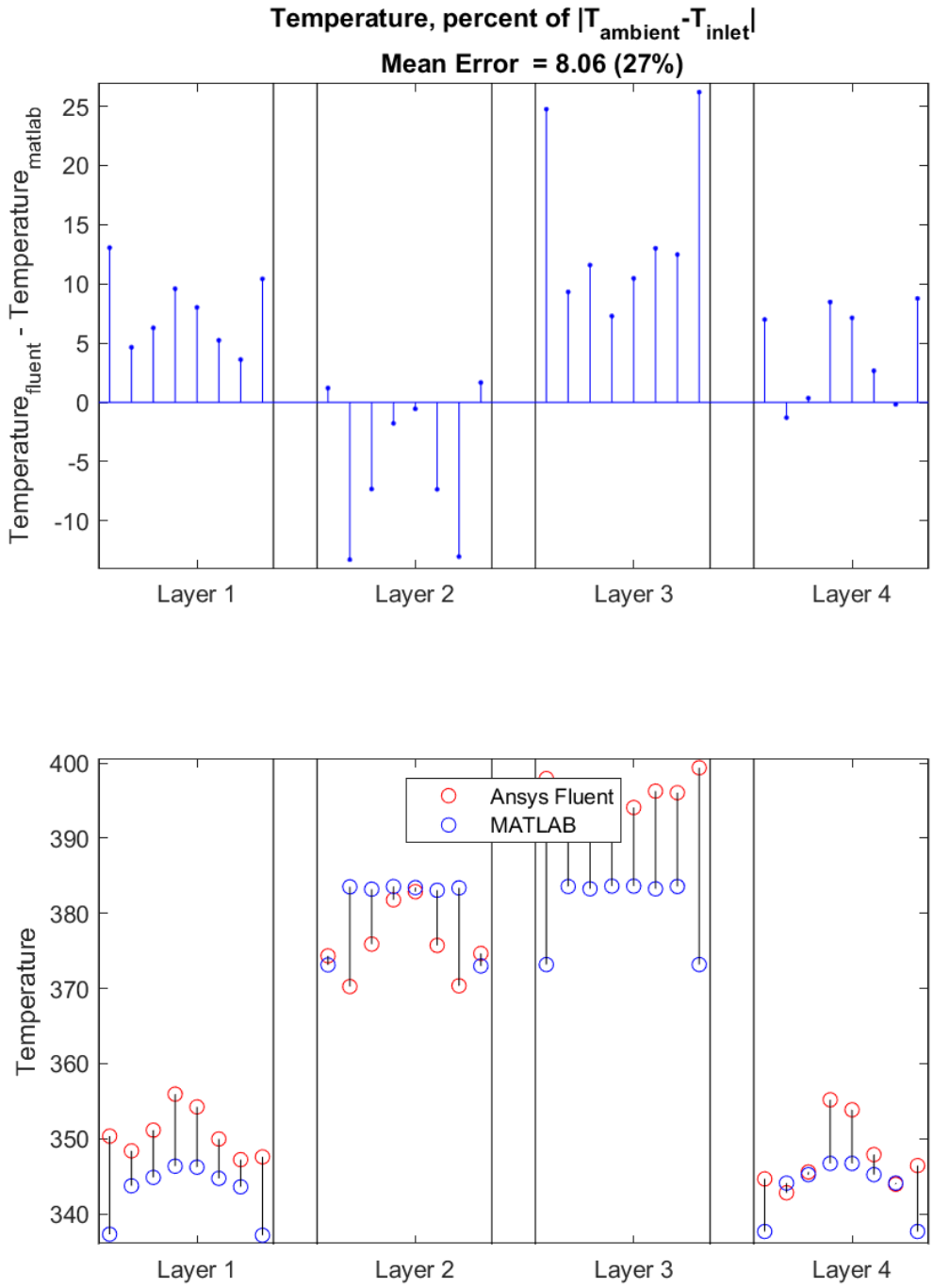

Figure 4.25: Temperature Error Plots for case 7

4.2.6 Case 11

Figure 4.26-4.27 presents the error calculations for mass flow, temperature and pressure for case 11, a medium velocity heating case with high heat differential and active

heat sources. Like in case 7, the temperature error remains centered around layer 2 without clear visual indication from the flow error to indicate the source of this behavior.

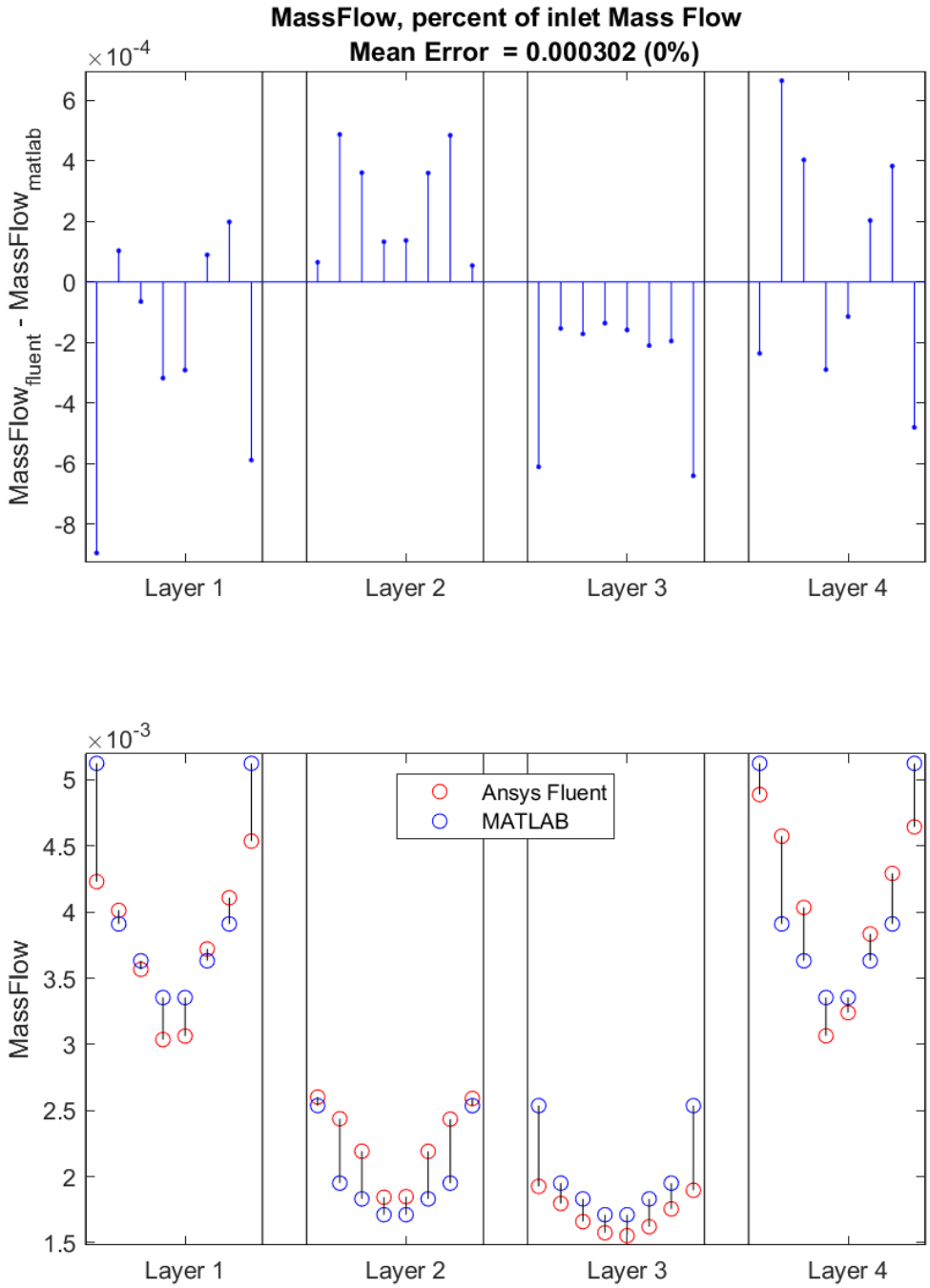

Figure 4.26: Mass Flow Error Plots for case 11

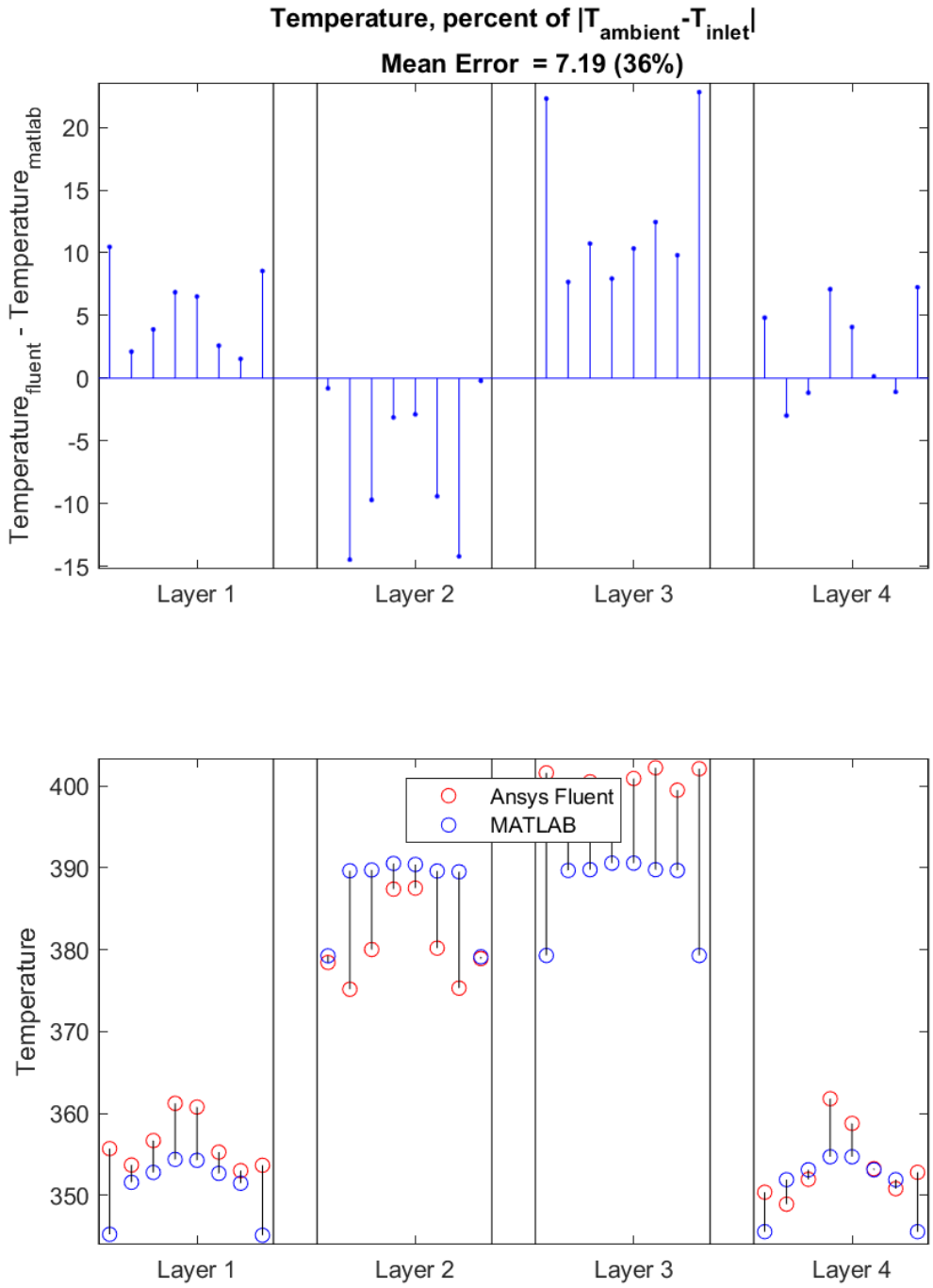

Figure 4.27: Temperature Error Plots for case 11

4.2.7 Single Layer

For the single layer geometry, the results are presented as split into two arms, with arm one representing boxes $1-4$ in ascending order and arm 2 representing box $5-8$ in descending order. The choice to present the result in this manner is to give an overview of the systems symmetrical nature. Like for the multiple layer geometry, the the case table is again presented here for convenience. Like for the multi layer validation results, most of these allocated to the appendix.

Table 4.2: Reference table for single layer test cases

Case	$T_{in}\,[C]$	$T_A\,[C]$	$v_{in}\,[ms^{-1}]$	$S_hV\ [W]$
1	20	50	2.5	0
2	30	0	2.5	0
3	30	0	5	0
4	30	0	2.5	200
5	40	-20	2.5	0

4.2.7.1 Case 4

Figure 4.28-4.29 presents the error calculations for mass flow, temperature and pressure for case 4 for the single layer geometry, a medium velocity heating case with active heat sources. Although the magnitude of the temperature error increases, it's shape remains roughly consistent with case 1 for the single layer, a cooling case.

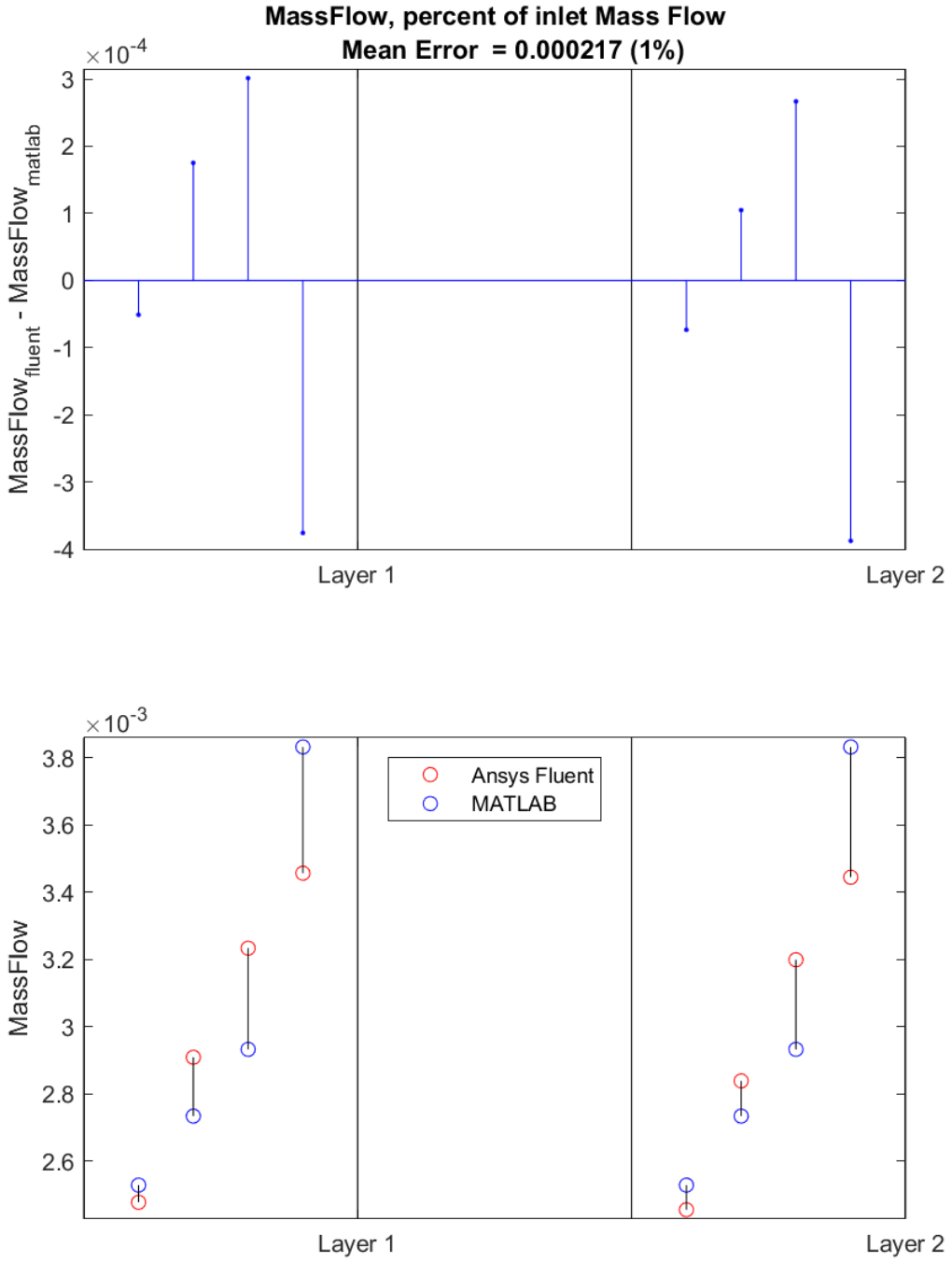

Figure 4.28: Mass Flow Error Plots for case 4

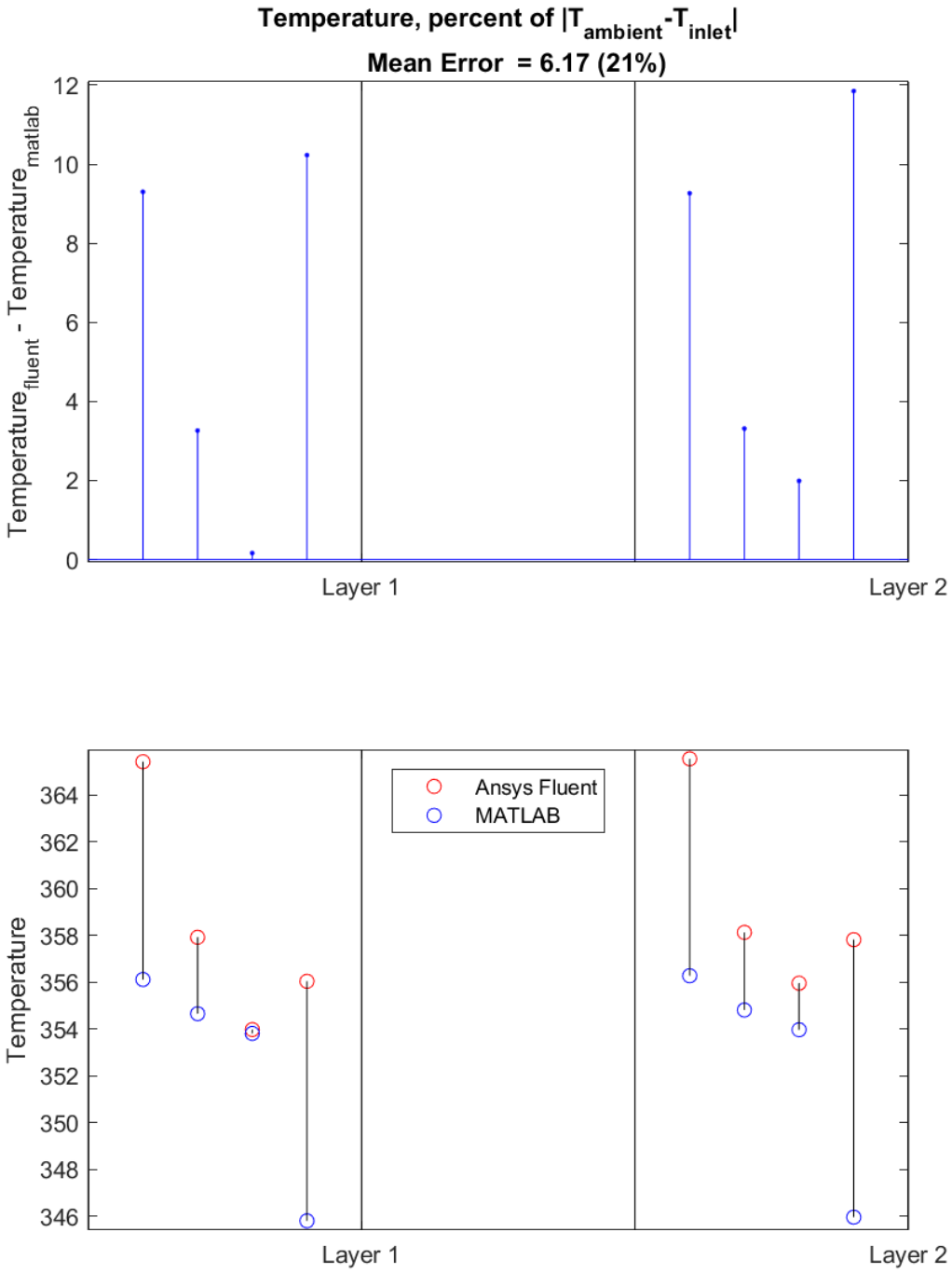

Figure 4.29: Temperature Error Plots for case 4

4.3 Error correlation estimates

This section presents a number of graphical error correlation estimates for the differing input variables present in the test cases. Figure 4.30 presents the behavior of the temperature error in response to the different temperature inputs available in the test cases while figure 4.31 presents the behavior of the temperature error in response to the different velocity inputs. Of note is that the cases with heat sources active all occur at $V_{in} = 10$, hence that serves to limit the information that can be gained from the velocity plot.

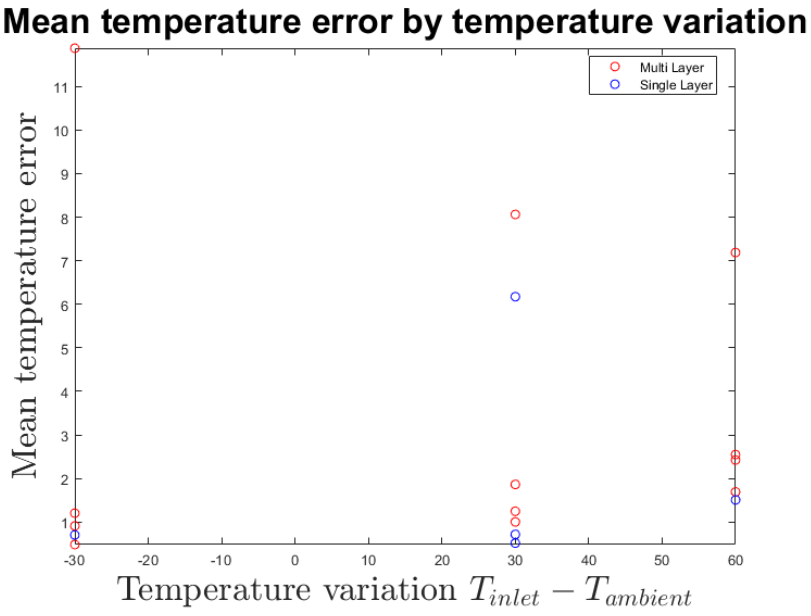

Figure 4.30: The temperature errors correlation with input temperature

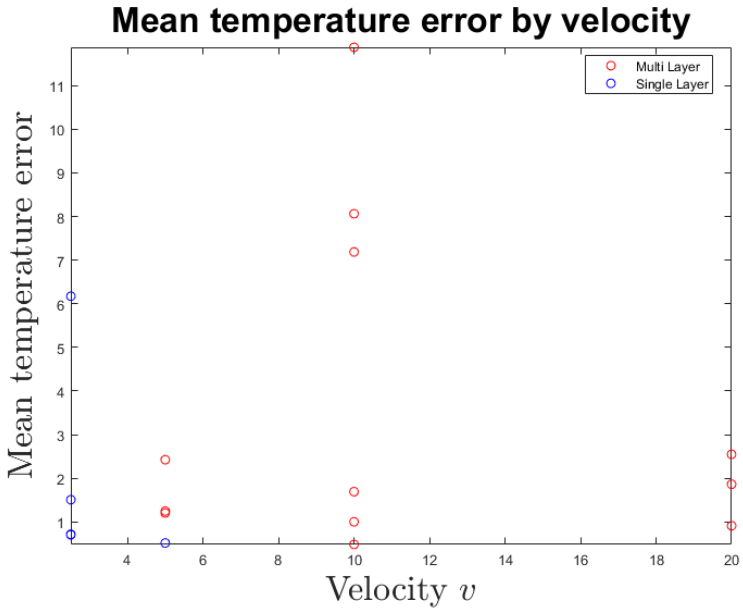

Figure 4.31: The temperature errors correlation with input velocity

Figure 4.32 presents the behavior of the flow error in response to the different velocity inputs available. The flow error has some manner of probably correlation, although it is not as easily observable.

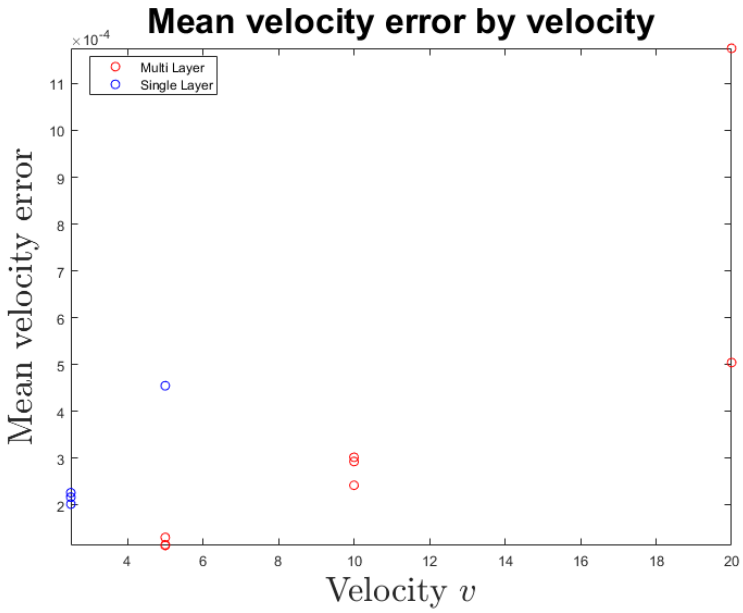

Figure 4.32: Velocity error correlation with input velocity

Figure 4.33 presents the behavior of the temperature error in response to the inclusion of a 200 W heat source as an adjusted temperature in each of the cylinders.

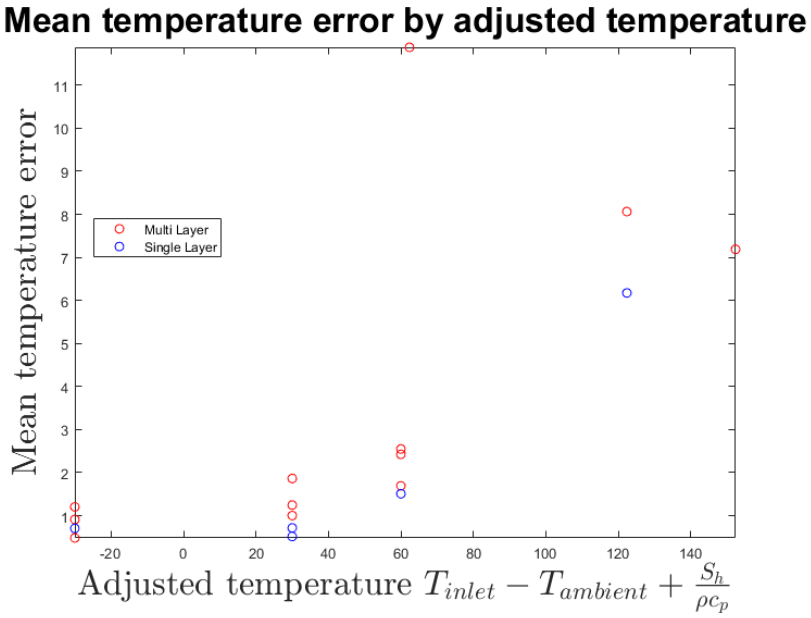

Figure 4.33: The temperature errors correlation with adjusted temperature

Figure 4.34 presents an alternate way of creating an adjusted temperature that is included to shine further light on the interactions between the heat source and the temperature error.

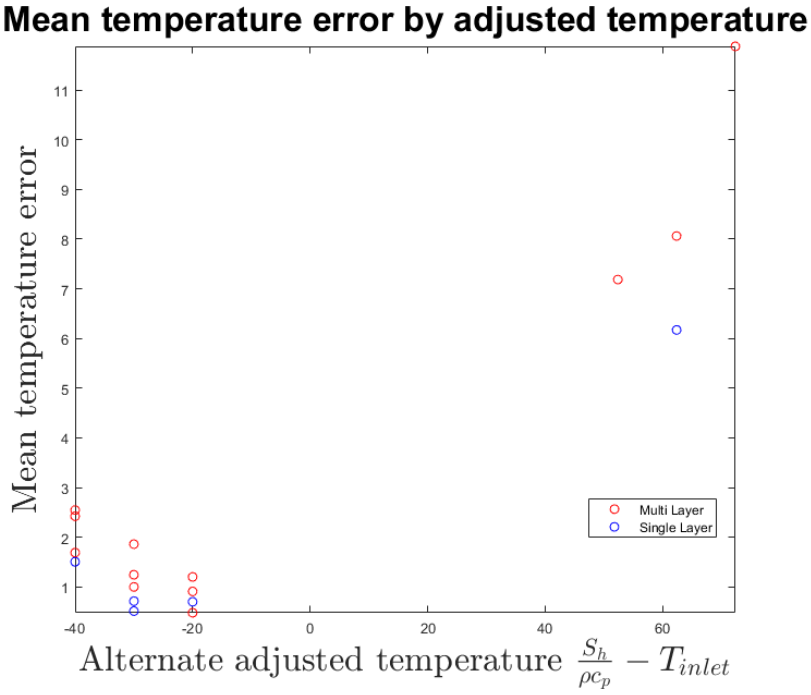

Figure 4.34: The temperature errors correlation with adjusted temperature

4.4 Minor loss coefficient approximations

This section describes the result of varying the minor loss coefficients on the mass flow error. Figure 4.35 presents the variation of the mass flow error as the minor loss coefficient of the unknown box is varied. Since there is no precedent for this value, it is taken as the local optimum found at 150.

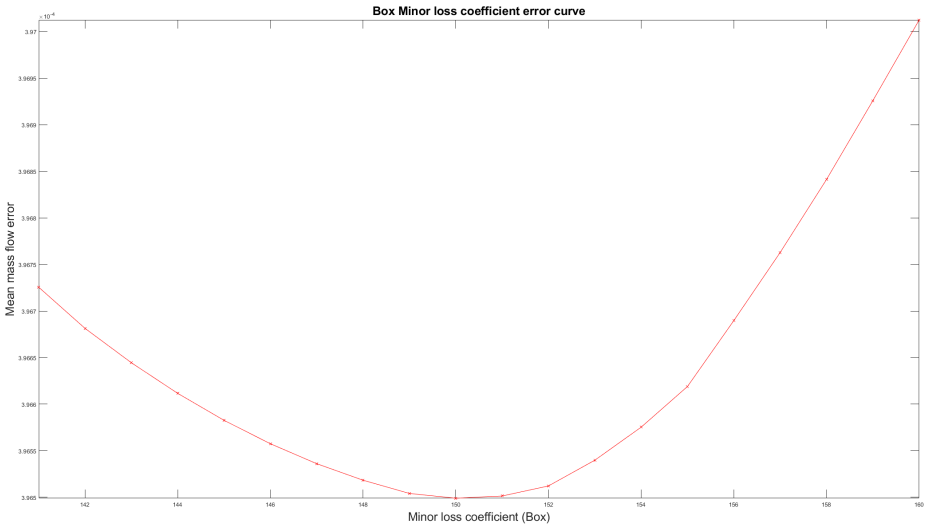

Figure 4.35: Mass flow error correlation with Box coefficient

Using this value of 150, figure 4.36 presents the variation of the mass flow error as the minor loss coefficient for the t-junctions found in equation 2.21 and equation 2.27 is multiplied by a factor. As there is a precedent for the value of the minor loss coefficient for T-junctions, this is not used to produce other results.

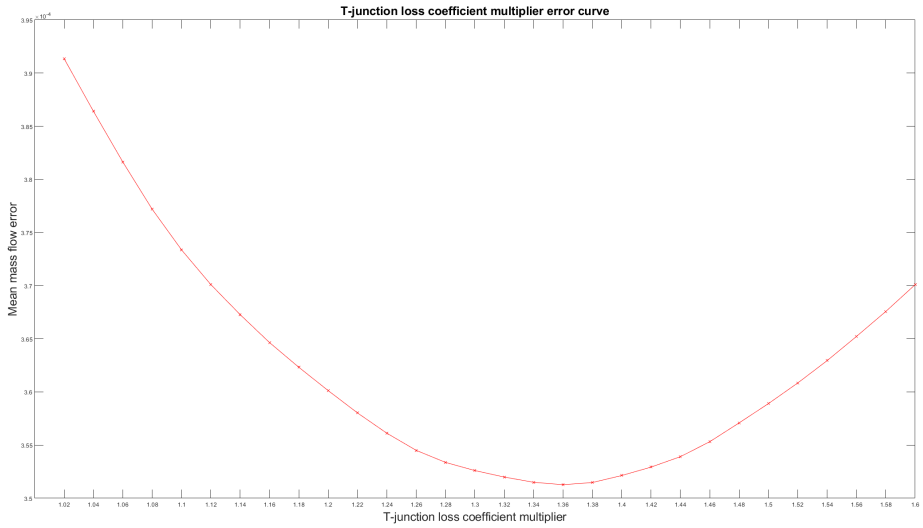

Figure 4.36: Mass flow error correlation with T-junction coefficient multiplier

Similarly, figure 4.37 presents the variation of the mass flow error as the minor loss coefficient for the bend is varied. All three figures presented so far have been observed to the approximately convex on the band that was investigated. Although there is significant reason to believe that these minor loss coefficients optima would be interlinked, running the variation of the box coefficient with the respective optima for both the bend and t-junction coefficients yielded no new optima.

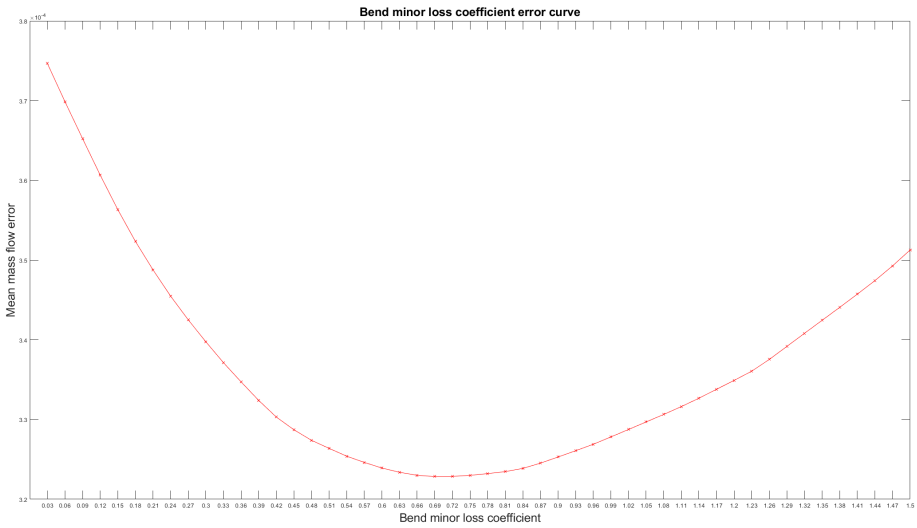

Figure 4.37: Mass flow error correlation with bend coefficient

4.5 Transient implementation

Figure 4.38 shows the progression of the transient version of the flow rate solver for case 2 for the single layer geometry without density overrides, with the values measured in the same manner as for the validation. The time-step used in generating this figure was 0.01. This implementation is not validated, as repeated issued occurred with the usage of ANSYS FLUENT to create a transient validation. The transient solution had a run-time of roughly five minutes for 2000 time-steps in the MATLAB Flow rate solver. An attempted transient ANSYS FLUENT with similar paraments calculation took an excess of 10 hours but did not produce any conclusive results.

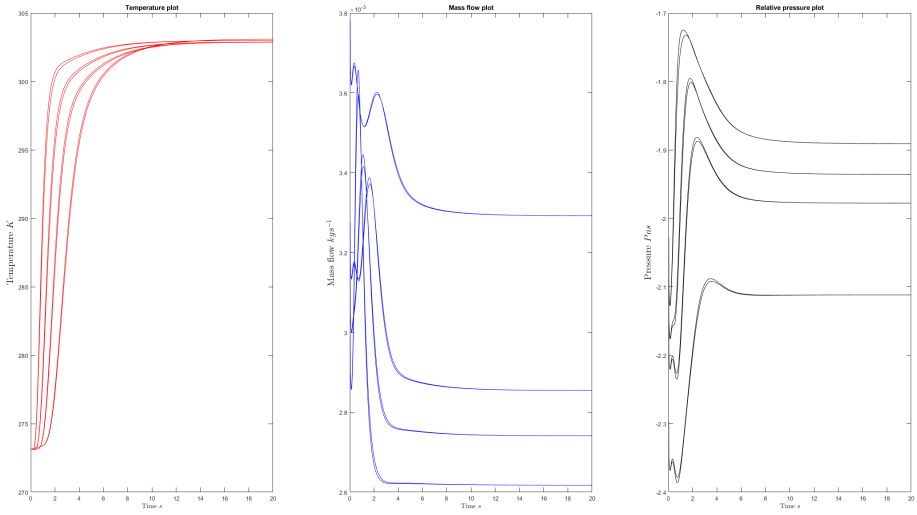

Figure 4.38: Showcase of transient flow rate solver for case 2

Figure 4.39 shows the progression of the transient version of the flow rate solver for case 4 for the single layer geometry without density overrides. Similarly to figure 4.38, it is not validated and uses a time-step of 0.01. The run-time was roughly four minutes.

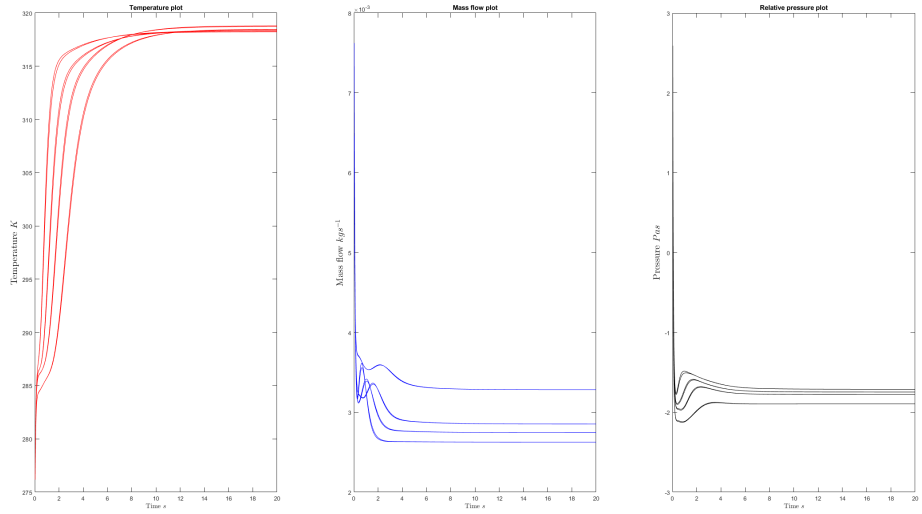

Figure 4.39: Showcase of transient flow rate solver for case 4

Figure 4.40 shows the progression of the transient version of the flow rate solver for case 3 for the multi-layer geometry without density overrides. The run-time for producing this simulation was roughly 15 minutes.

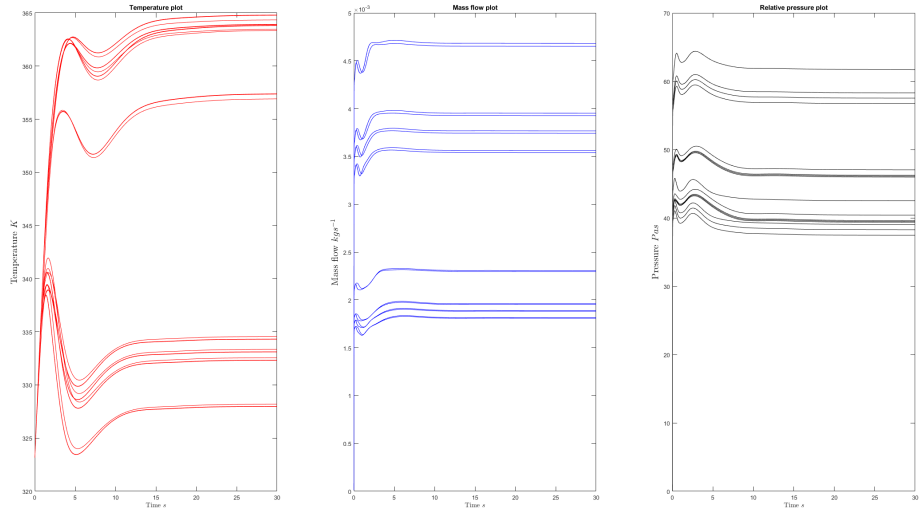

Figure 4.40: Showcase of transient flow rate solver for multi-layer case 3

4.6 Run time Comparison

Table 4.3 contains an overview of the differing run times of the MATLAB flow solver and the ANSYS FLUENT simulations. Due to the vast difference in scale and due to only having single runs to base the measurement off for the ANSYS FLUENT run times, the accuracy of the measurements is kept low and maintained simply for demonstrative purposes.

Table 4.3: Approximate run time for ANSYS FLUENT and MATLAB

Case	Run time (Fluent)	Run time (MATLAB)
1	>1 hours	3.6 s
2	>1 hours	1.7 s
3	>2 hours	1.8 s
4	>1 hours	1.2 s
5	>1 hours	3.8 s
6	>1 hours	1.6 s
7	>2 hours	1.8 s
8	>1 hours	1.3s
9	>1 hours	4.0 s
10	>1 hours	1.7 s
11	>2 hours	1.8 s
12	>1 hours	1.3 s
Single Layer	Run time (Fluent)	Run time (MATLAB)
1	>1 hours	0.4 s
2	>1 hours	0.3 s
3	>1 hours	0.4 s
4	>1 hours	0.4 s
5	>1 hours	0.6 s

5

Conclusion

5.1 Validation

This section discusses the results of the validations attempts of the model and the resulting findings regarding it's accuracy.

5.1.1 Temperature Error

For the purposes of evaluating the accuracy of the model, it is worth considering several factors. To begin with, the maximum error observed in any of the validation runs for temperature ranged around 20 to 25 K in the cases that had a $200W$ heat sources, corresponding to roughly 5% of the total temperature, $30 - 50\%$ of the temperature differential or $16 - 20\%$ of the adjusted temperature differential. Meanwhile the largest temperature error ranges around 4 to 5 K for the validation cases without heat sources, corresponding to roughly 1% of the total temperature or 8% of the temperature differential. This maximum error directly correlates with the cases that had the greatest temperature differential, that being the ones with an inlet temperature of 40 C° and an ambient temperature of -20 C°.

A way to simplify this error description would be to regard the heat sources as contributors to the temperature differential. Since both the ambient and inlet temperature are, in effect, volumetric heat sources, the contribution to the temperature differential could be approximated as $\frac{S_h}{\rho c_p}$, which, for the values used in the validation setting, would contribute to roughly 90 C° worth of temperature differential. Viewed this way, the temperature errors dependence on the adjusted temperature can be determined to have a somewhat complex interaction best observed in figure 4.34.

If one adopts this view of the temperature error, it is possible one can estimate an *a priori* temperature error compared to an ANSYS FLUENT simulation using the same settings from the flow rate solver based on the temperature differential recalculated to include any heat source. It is also obvious that the flow rate solver would need corrections to be able to accurately estimate the results of any high-energy simulations.

5.1.2 Flow Error

In regards to the predicted volumetric flow rate throughout the validated models, the results provide evidence that a volumetric flow rate model works relatively well as a predictor of the mass flow throughout the system, with the errors being small. There are however, a few noted consistencies in the error that fall squarely on the side of 'failure to model' which will be further discussed in the later parts of this chapter. Also of note is that the way the flow divides itself is heavily dependent on the assumed minor loss coefficient of the 'boxes' that were used to replace some unknown components. This indicates that what actually happens to the flow in-between leaving the inner pipe structure and returning to the outer one plays a key part in how the flow will operate in any actual structure, and thus great care should be taken to model it in any actual system.

5.1.3 Pressure error

Predicting the pressure drop over the unknown boxes can perhaps be seen as the greatest failure of the flow rate solver, as it is indivisibly linked to the volumetric flow rate division, and the actual pressure drop dependence on the frankly massive minor loss coefficient that was estimated for the unknown boxes. As such, the flow rate solver cannot be said to accurately predict the pressure field.

5.1.4 Faults in methodology

One of the obvious downside to the way the validation was done is the usage of constants for the material properties of air. This, rather than accounting for the fact that, in reality, it is a compressible gas with viscosity and other thermal properties that are dependent on the field variables of the solution. While methods for estimating these properties are presented in this paper and included in the flow rate solver, they are not validated. The lack of validation for these methods comes down to a lack of available simulation time for ANSYS FLUENT combined with a decision to prioritize validating an easier case, that being the one with constant material properties. It is however, a likely source of error, although test runs with compressibility active in the flow rate solver hints that this error source is less extreme than, for example, the temperature differential.

5.1.4.1 Lack of transient validation

Likewise, the transient implementation of the flow rate solver is not validated either. This also stems from a lack of available simulation time with ANSYS FLUENT, combined with early test runs of such simulations providing vastly different results dependent on the chosen time-step size that ranged between 10^{-3} and 5 s, hinting at a faulty setup for conducting transient simulations.

5.2 3D and resolution effects

This section discusses the observed effects of the ANSYS FLUENT simulations that for one reason or another could not be conceivably modeled in the flow rate solver.

5.2.1 Helical flows

As can be observed in figure 4.7 as well as partially in figure 4.2 the multi-layer ANSYS FLUENT simulation gave rise to a number of helical flows following the various bends and junctions in the structure. This helical flow may contribute to the asymmetry observed between the layers and arms in the ANSYS FLUENT simulation compared to the MATLAB one, but that is conjecture at best. What can be observed however is that the asymmetry between arms seemingly disappear in the single-layer structure where the internal pipe structure lacks any visible helical flow, as per figure 4.9. As the flow rate solver does not concern itself with the velocity field itself, merely the cross-section average over the entire pipe, it is by definition unable to model or capture any such behavior and presents a source of error as it is a 1D model.

5.2.2 Asymmetry

As previously mentioned when discussing the helical flows, the ANSYS FLUENT simulations produces an asymmetry along the z-axis that cannot be reasonably reproduced in the flow rate solver. It is guessed that this asymmetry arises as an aftereffect carried on the flow from the entrance trunk, as it is the only asymmetrical part of the system. Additionally, the asymmetry observed between the arms cannot be modeled in the flow rate solver, and may perhaps arise similarly from the asymmetrical trunk, and be carried forwards as turbulent energy.

By extension, this observed asymmetry indicates the possibility that a model utilizing minor loss coefficients in order to calculate the flow through complex pipe systems may not be sufficient for more complex pipe networks. This is due to each bend and twist having possible down-chain effects carried by the velocity field beyond just a simple pressure drop which could not be captured by a minor loss model. One could imagine studying implementations of various combined effect models that extend the minor loss effects, although such is regarded as beyond the scope of this paper.

5.2.3 Other outliers

Other noteworthy outliers from the ANSYS FLUENT simulations include case 9, where the aforementioned temperature and flow error seemed to suddenly shift over to layer 3 without any notable explanation. The case is otherwise identical in setup to case 1 and 5 except for the different heat differential. The volumetric flow rate in the MATLAB flow rate solver is identical for the three cases when using constant material properties (hence preventing the energy equation from influencing the flow

equation). Thus, this may arise as some manner of turbulent occurrence from the ANSYS FLUENT models, but cannot be easily explained.

5.3 Runtime

This section discusses the run-time differences between the ANSYS FLUENT solutions and the flow rate solver. Being perhaps the most beneficial component of the flow rate solver, it can be clearly observed in table 4.3 that the flow-rate solver presented in this thesis has a significant run-time advantage over ANSYS FLUENT. As such, it could be a valuable tool if one wants a variety of systems approximated in quick succession without needing to spend the hours of cluster-time required to perform accurate FLUENT simulations. This assumes that the approximate accuracy is good enough to judge whether or not a system is worthy of full simulation.

5.4 Observations

This section discusses other observations found from the results.

5.4.1 Design for equivalent cooling of multiple electrical enclosures

While, as previously mentioned, the flow division depends heavily on the actual pressure drop within the boxes and any actual system has to be designed around them, one observation of note is that a multi-pronged pipe of singular radius with several serial t-junctions will inherently not equally divide the flow to those t-junctions under any circumstances. In order to achieve an equal division, and thus equal cooling potential, the design would need to vary the pipe diameter in-between each of these junctions in a somewhat complex manner.

5.5 Future improvements

This section discusses how the flow rate solver could be improved in future iterations to better capture other properties of interest.

5.5.1 Error correction

The first, and most obvious improvements that could be made to the flow rate solver is to find and include further effects. To try and model the asymmetry found in the FLUENT simulations by some manner of down-chain minor loss linking for bends, such that the minor loss coefficient for the connection c has an effect on pipes n links away from c depending on their relative direction compared to c. Other improvements include adjustments to the energy equation to try and capture the runaway temperature error that occurs in the cases with high heat sources active.

5.5.2 Moisture transport

Another imaginable improvement would be the inclusion of moisture transport and accumulation as it is highly relevant in these kinds of systems. Attempts would have to be made to attempt and model the multi-phase interactions in a 1D environment. Such and attempt would also necessitate complex methods of calculating the density fields and thermal properties, but it is otherwise one of the simpler improvements that could be imagined.

5.5.3 Pipe size recommendations

A post-processing algorithm that uses the matrices, specifically the pressure drop matrix presented in this paper along with the flow matrix, could theoretically be constructed. Such an algorithm could provide recommended adjustments for pipe diameters in order to achieve an equivalent or near equal temperature in all ventilated enclosures.

Bibliography

[1] ANSYS FLUENT, *ANSYS FLUENT 12.0 Theory Guide - Contents*.

[2] G. Brown, *The Darcy–Weisbach Equation*, Oklahoma State University–Stillwater.

[3] S. Chapman and T. G. T. G. Cowling, *The mathematical theory of non-uniform gases; an account of the kinetic theory of viscosity, thermal conduction and diffusion in gases*, (1970), p. 423.

[4] S. W. Churchill and H. H. Chu, *Correlating equations for laminar and turbulent free convection from a vertical plate*, International Journal of Heat and Mass Transfer, 18 (1975), pp. 1323–1329.

[5] Engineering Toolbox, *Conductive Heat Transfer*, 2003.

[6] V. Gnielinski, *Neue Gleichungen für den Wärme- und den Stoffübergang in turbulent durchströmten Rohren und Kanälen*, Forschung im Ingenieurwesen A 1975 41:1, 41 (1975), pp. 8–16.

[7] O. Gonzalez and A. M. Stuart, *A First Course in Continuum Mechanics*, Cambridge Texts in Applied Mathematics, Cambridge University Press, 2008.

[8] E. A. Guggenheim, *Thermodynamics*, North-Holland Publishing Company, Amsterdam, 1959.

[9] V. John Philipp, L. Martin Francis, S. Angus, and B. Anton, *(PDF) Advances in Unsteady Friction Modelling in Transient Pipe Flow*.

[10] Jones and Frank E, *Calculation of Compressibility Factor for Air Over the Ranges of Pressure, Temperature, and Relative Humidity of Interest in Flowmeter Calibration*.

[11] V. J. Katz, *The history of Stokes's theorem*, Mathematics Magazine, 52 (1979), pp. 146–156.

[12] D. S. M.R. Spiegel, S. Lipschutz, *Vector Analysis (2nd Edition)*, (2009).

[13] J. Pedlosky, *Back Matter*, Geophysical Fluid Dynamics SE - 9, (1987), pp. 689–710.

[14] H. Rouse, *Elementary Mechanics of Fluids*, John Wiley & Sons, 1946.

[15] P. R. Vasava, *Fluid Flow in T-Junction of Pipes*, (2007).

[16] F. M. White, *Fluid mechanics*, (1999), p. 826.

A

Appendix

A.1 Supplemental case results

A.1.1 Multi layer geometry

A.1.1.1 Case 5

Figure A.1-A.2 presents the error calculations for mass flow, temperature and pressure for case 5, a high velocity heating case with no active heat sources. The temperature error is lower here than in the matching cooling case, case 1, and is not consistently positive or negative. Pressure error and flow error remain otherwise consistent in nature with case 1.

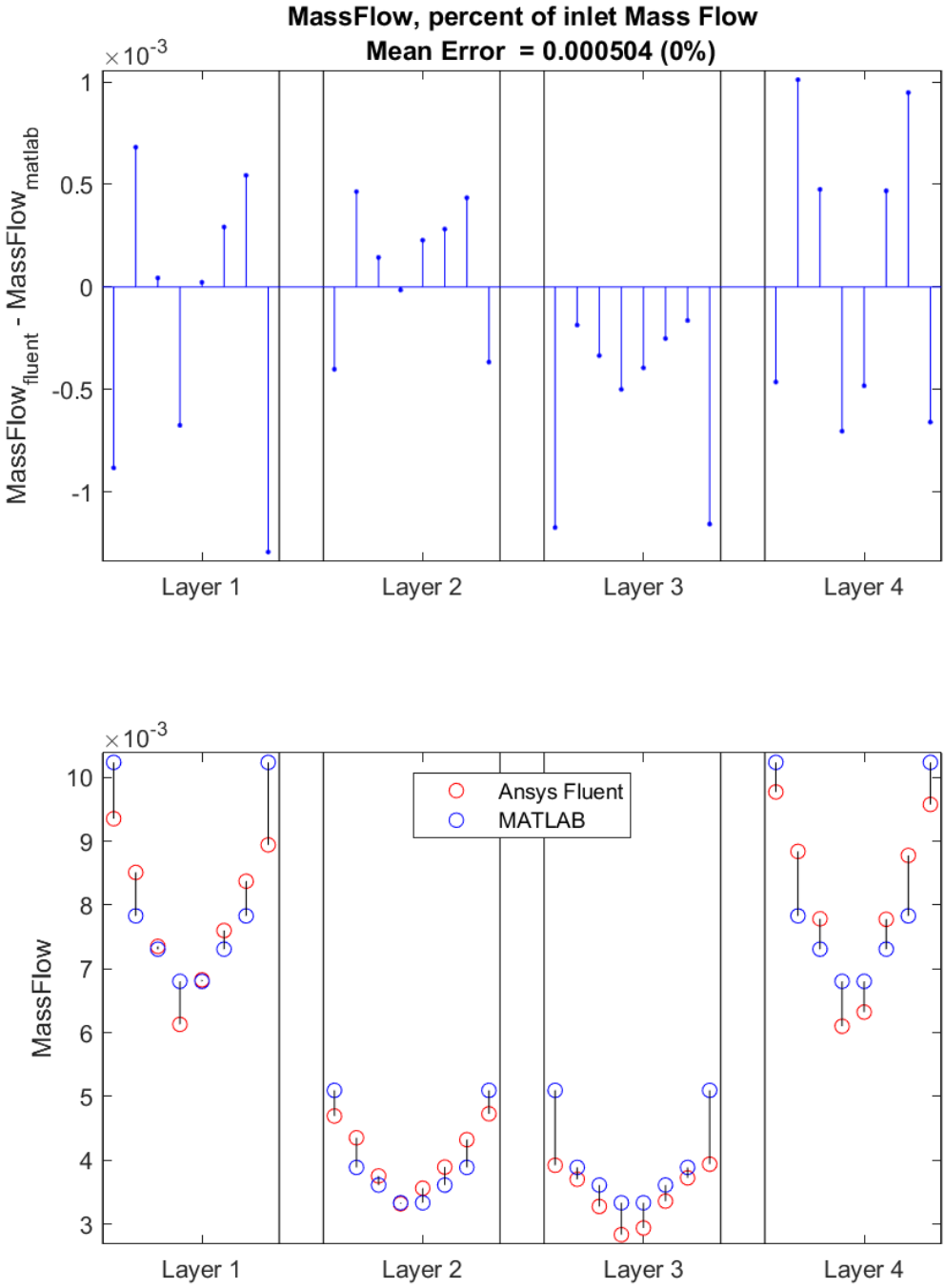

Figure A.1: Mass Flow Error Plots for case 5

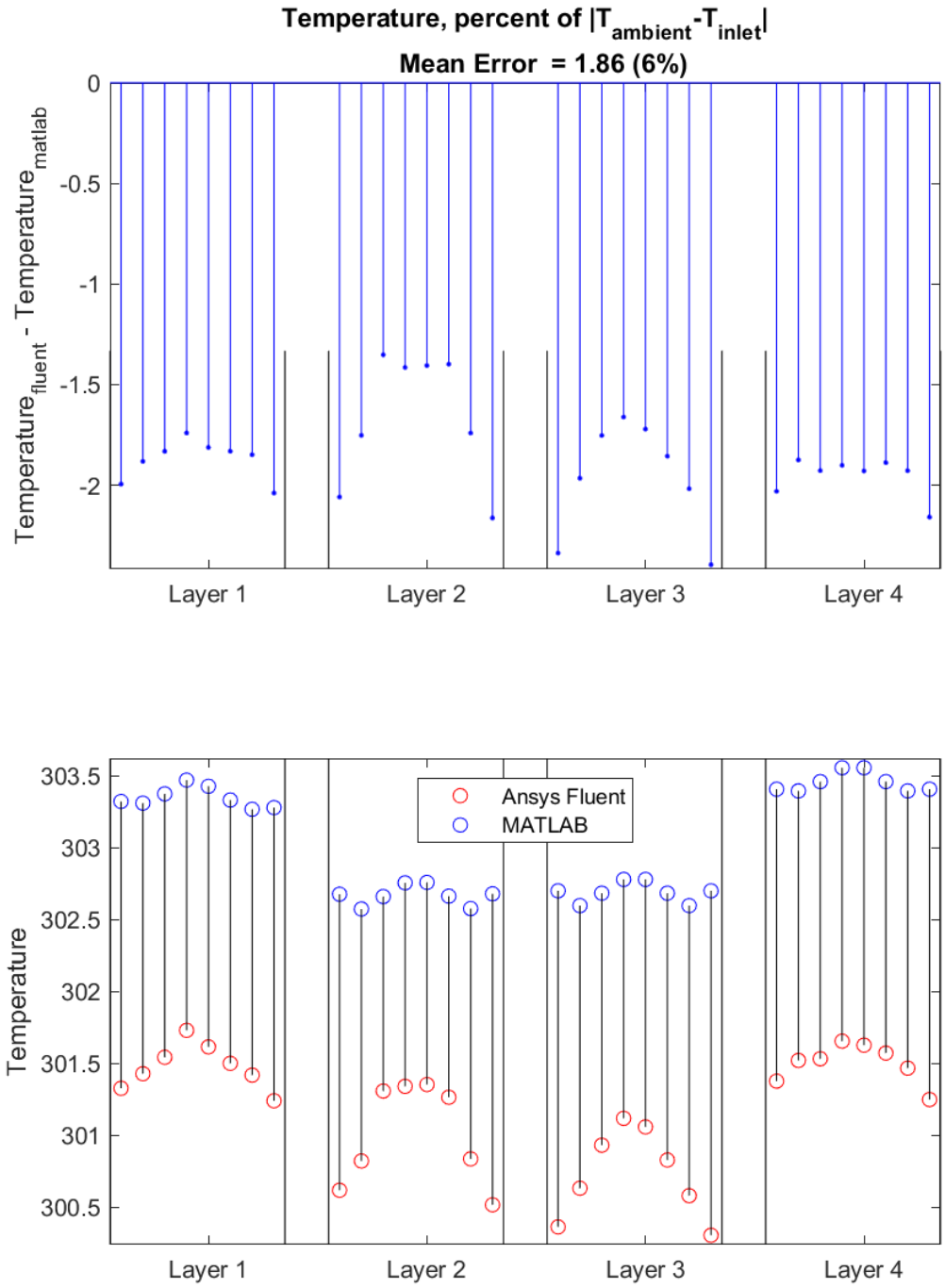

Figure A.2: Temperature Error Plots for case 5

A.1.1.2 Case 6

Figure A.3-A.4 presents the error calculations for mass flow, temperature and pressure for case 6, a medium velocity heating case with no active heat sources. The

temperature error is consistently negative here, in contrast to case 5 and case 2. Pressure error and flow error remain otherwise consistent in nature with case 2.

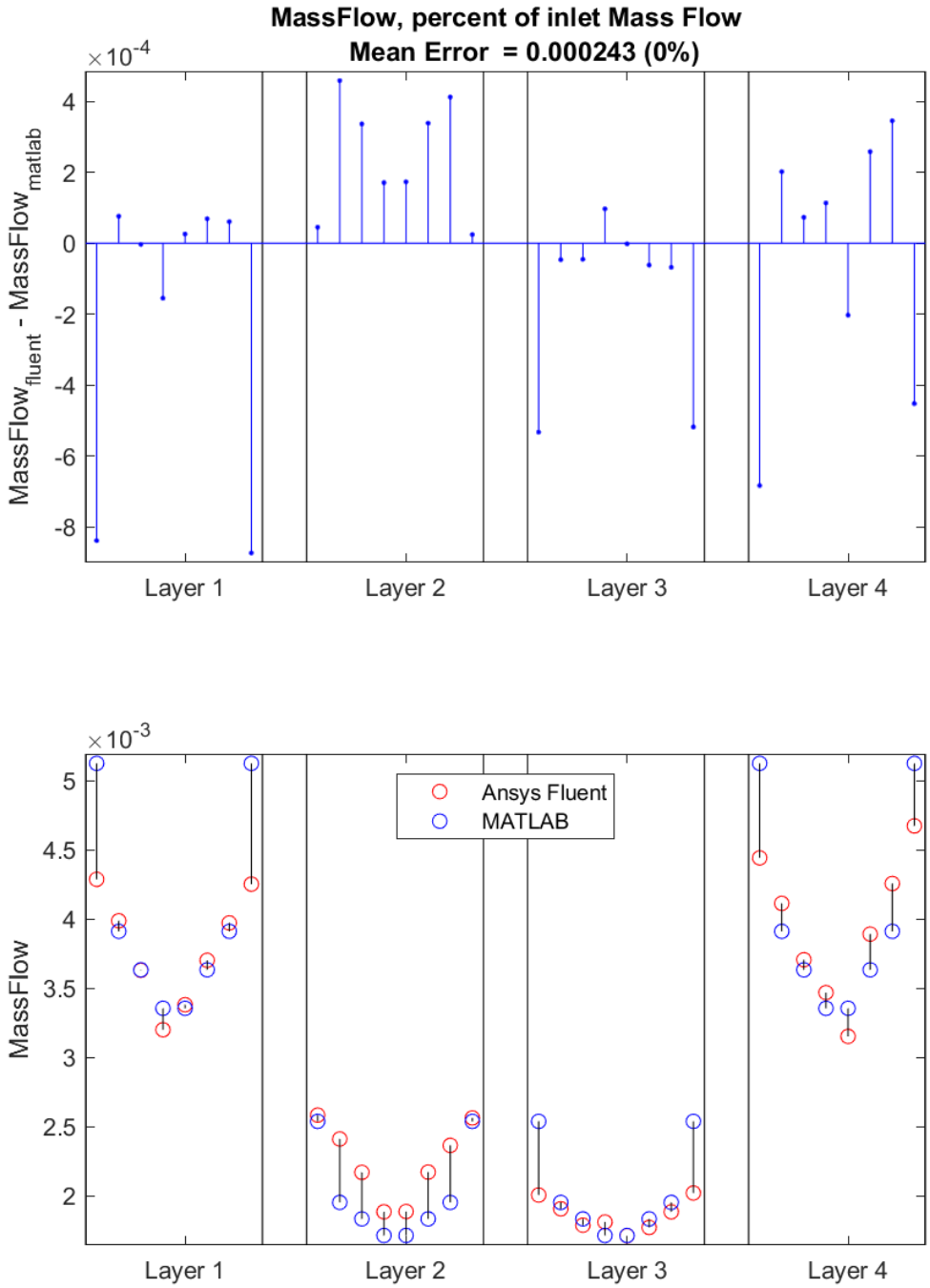

Figure A.3: Mass Flow Error Plots for case 6

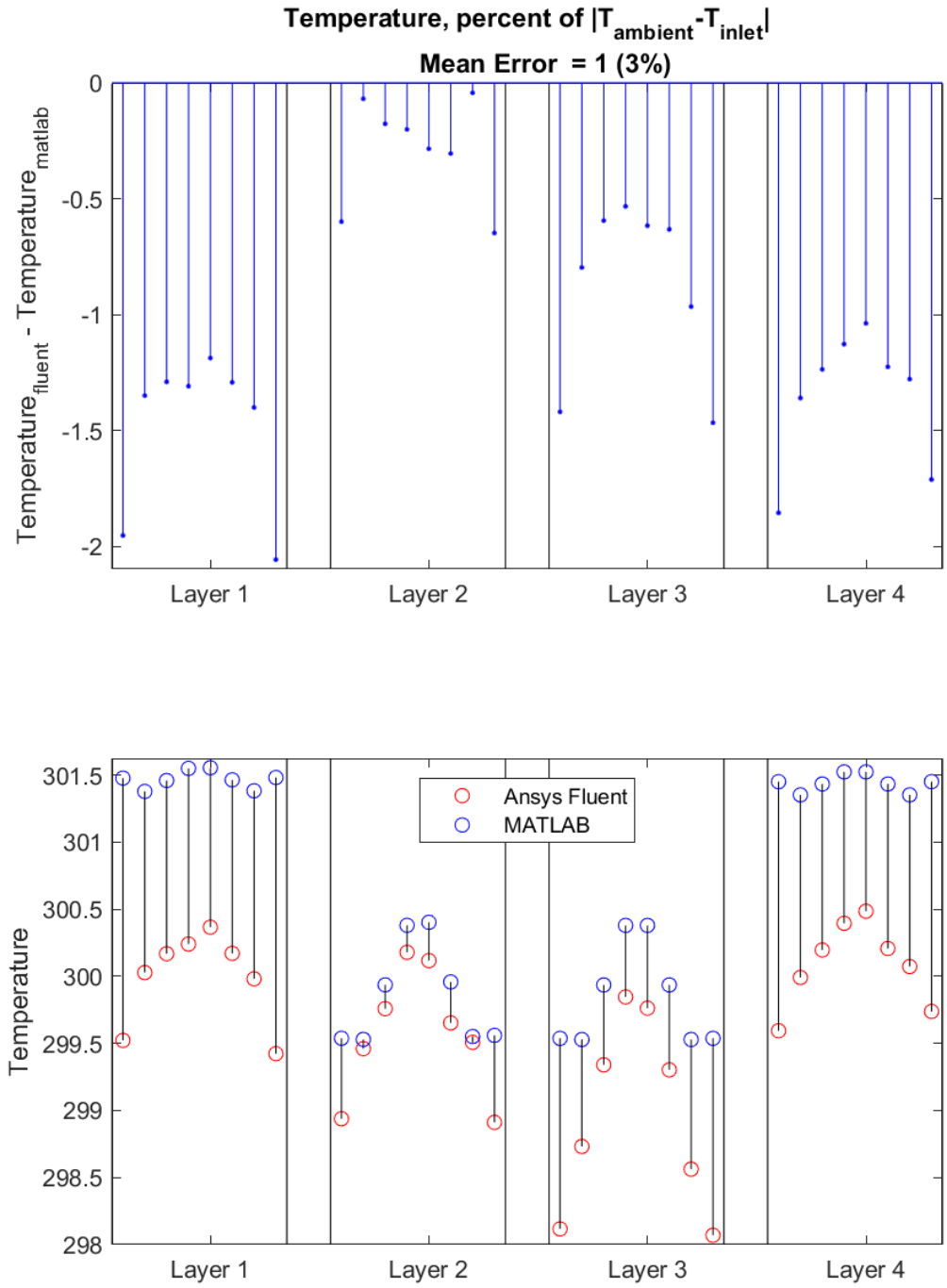

Figure A.4: Temperature Error Plots for case 6

A.1.1.3 Case 8

Figure A.5-A.6 presents the error calculations for mass flow, temperature and pressure for case 8, a low velocity heating case with no active heat sources. In contrast to

case 4, the temperature error is almost consistently negative, indicating the existence of some sort of error based on $T_{in} - T_{ambient}$ rather than $|T_{in} - T_{ambient}|$

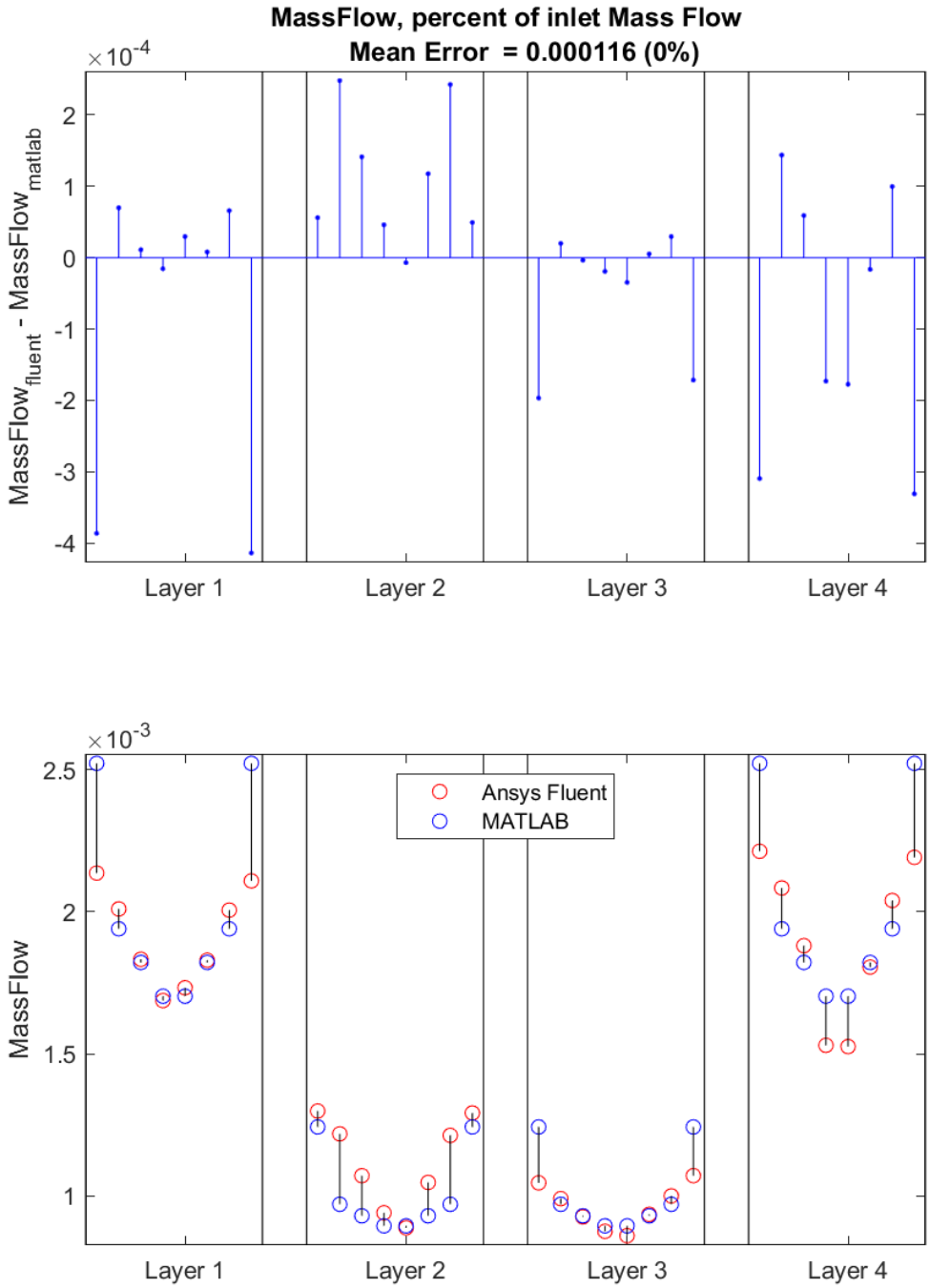

Figure A.5: Mass Flow Error Plots for case 8

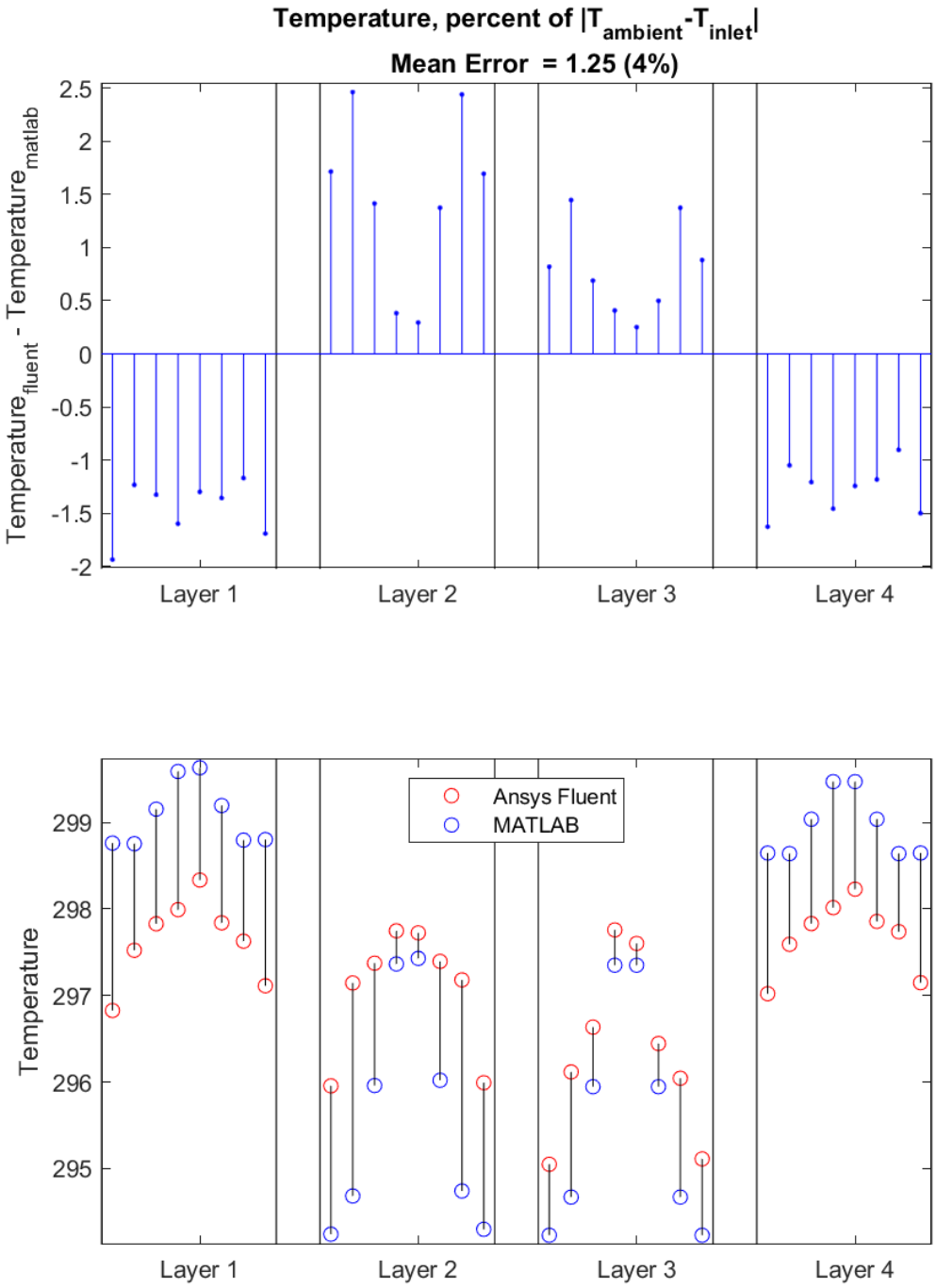

Figure A.6: Temperature Error Plots for case 8

A.1.1.4 Case 9

Figure A.7-A.8 presents the error calculations for mass flow, temperature and pressure for case 9, a high velocity heating case with high heat differential and no active

heat sources. The flow error is notably more present in layer 3 and layer 4 and notably larger than in case 1 and 5, which again hints at some asymmetry existing in the ANSYS FLUENT solution. The temperature error is also higher than in both case 1 and case 5 by roughly a factor two, indicating a linear scaling with the heat differential.

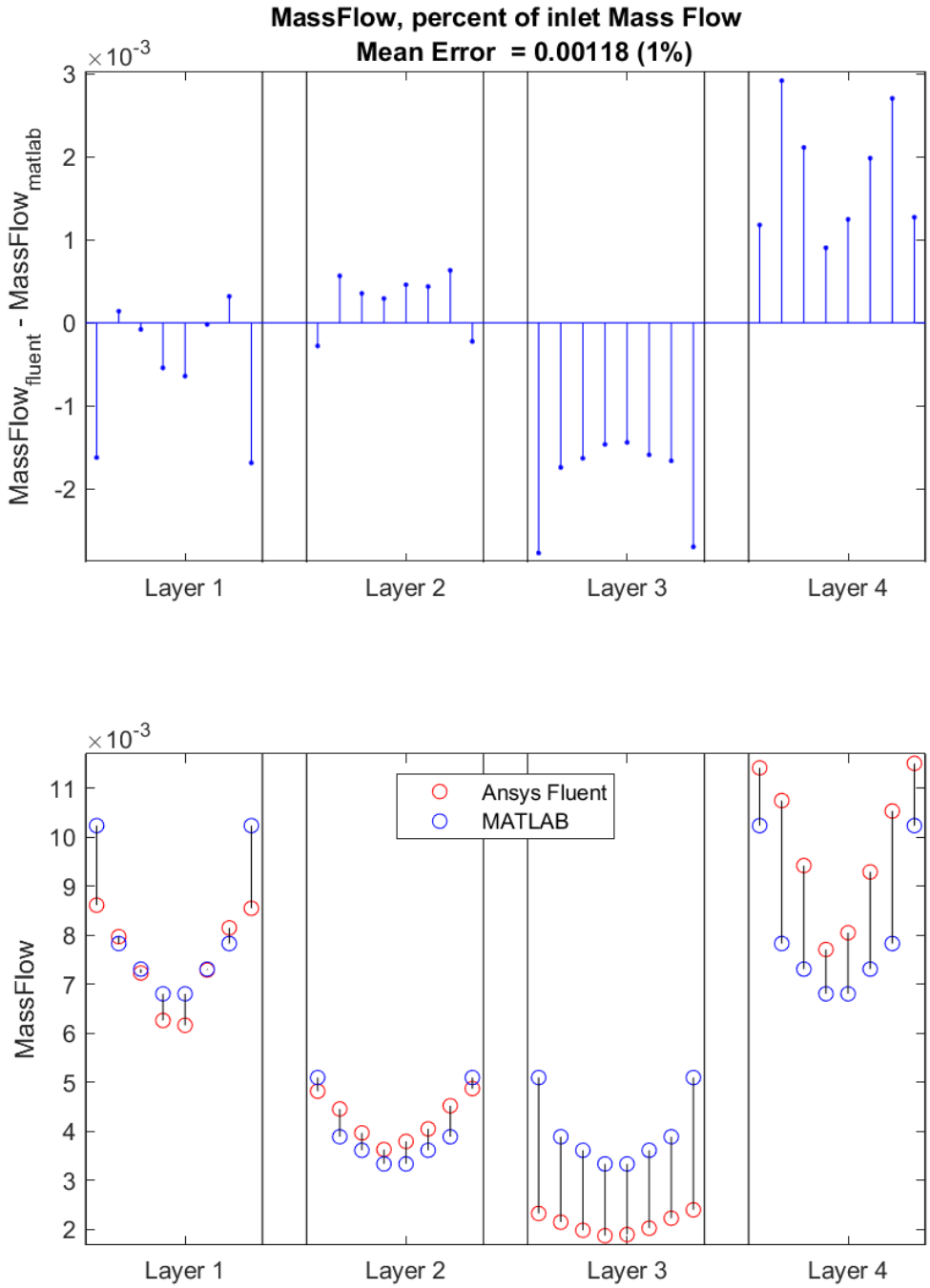

Figure A.7: Mass Flow Error Plots for case 9

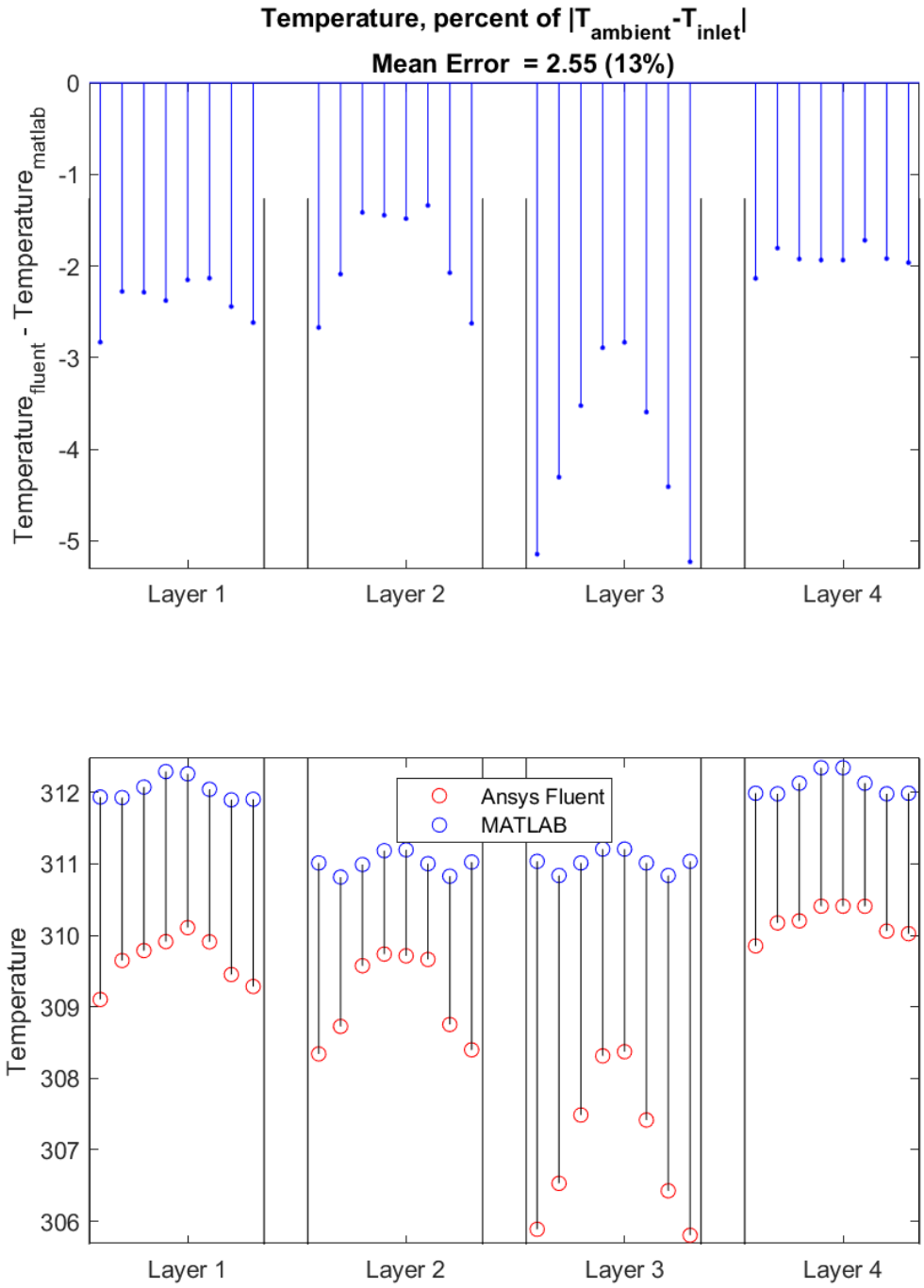

Figure A.8: Temperature Error Plots for case 9

A.1.1.5 Case 10

Figure A.9-A.10 presents the error calculations for mass flow, temperature and pressure for case 10, a medium velocity heating case with high heat differential and no

active heat sources. The flow error is no longer focused on layer 3 and 4 like in case 9, and roughly equivalent to that of case 2 and 6. The temperature error remains consistently negative and twice as large as case 2 and 6.

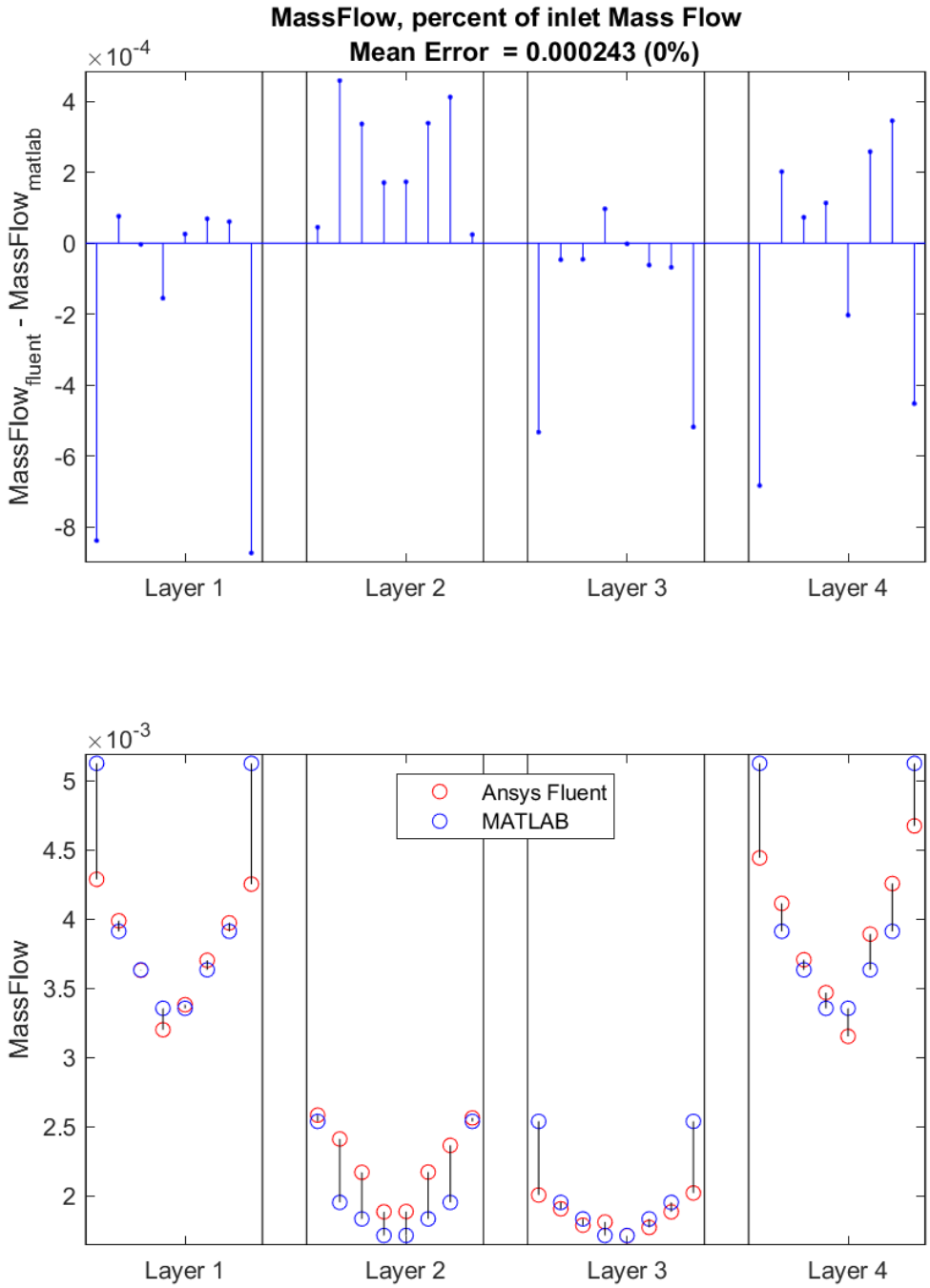

Figure A.9: Mass Flow Error Plots for case 10

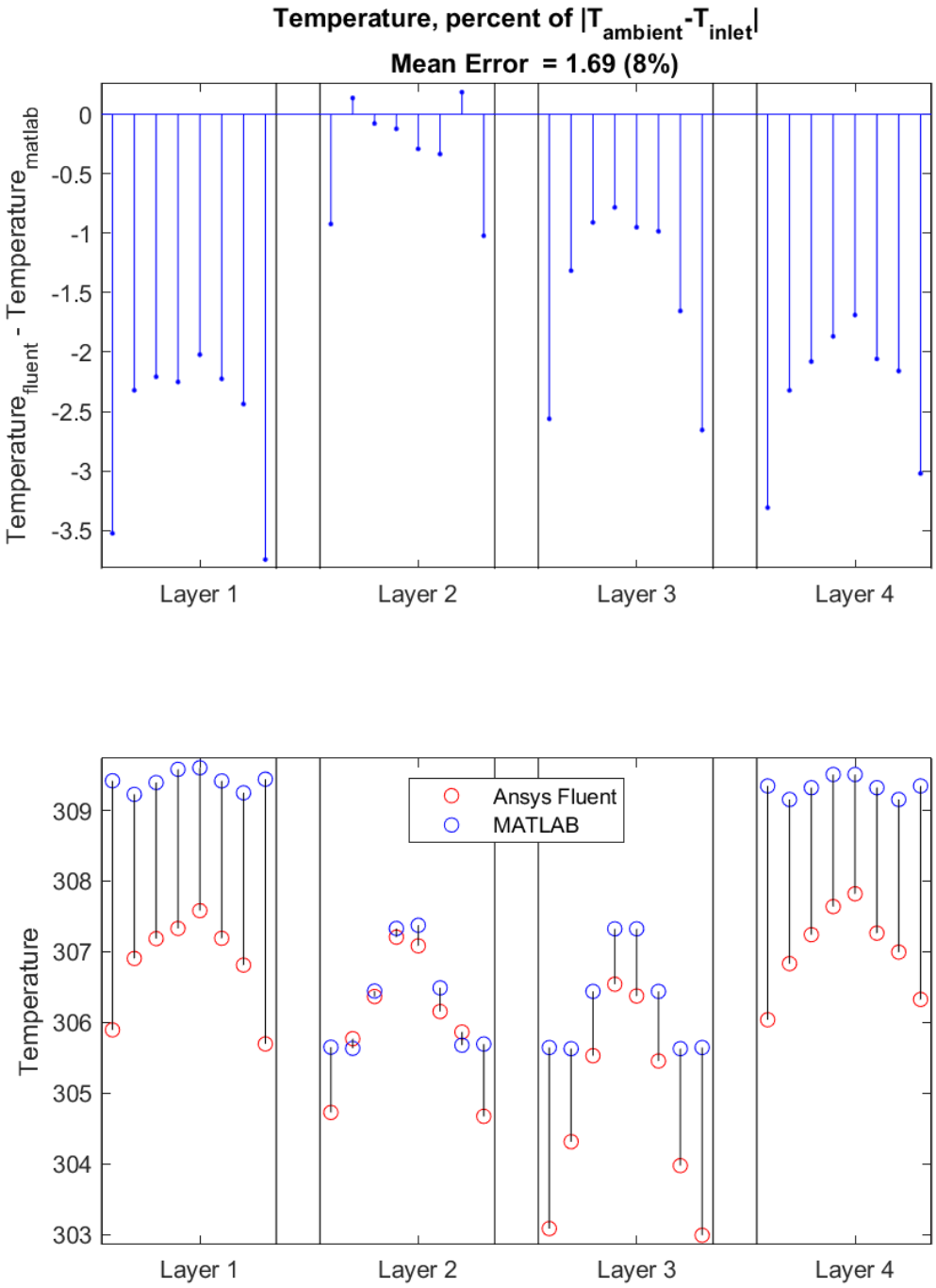

Figure A.10: Temperature Error Plots for case 10

A.1.1.6 Case 12

Finally, for the multiple layer geometry, figure A.11-A.12 presents the error calculations for mass flow, temperature and pressure for case 12, a low velocity heating case

with high heat differential and active heat sources. Like in case 8, the temperature error remains almost consistently negative, minimizing around layer 2.

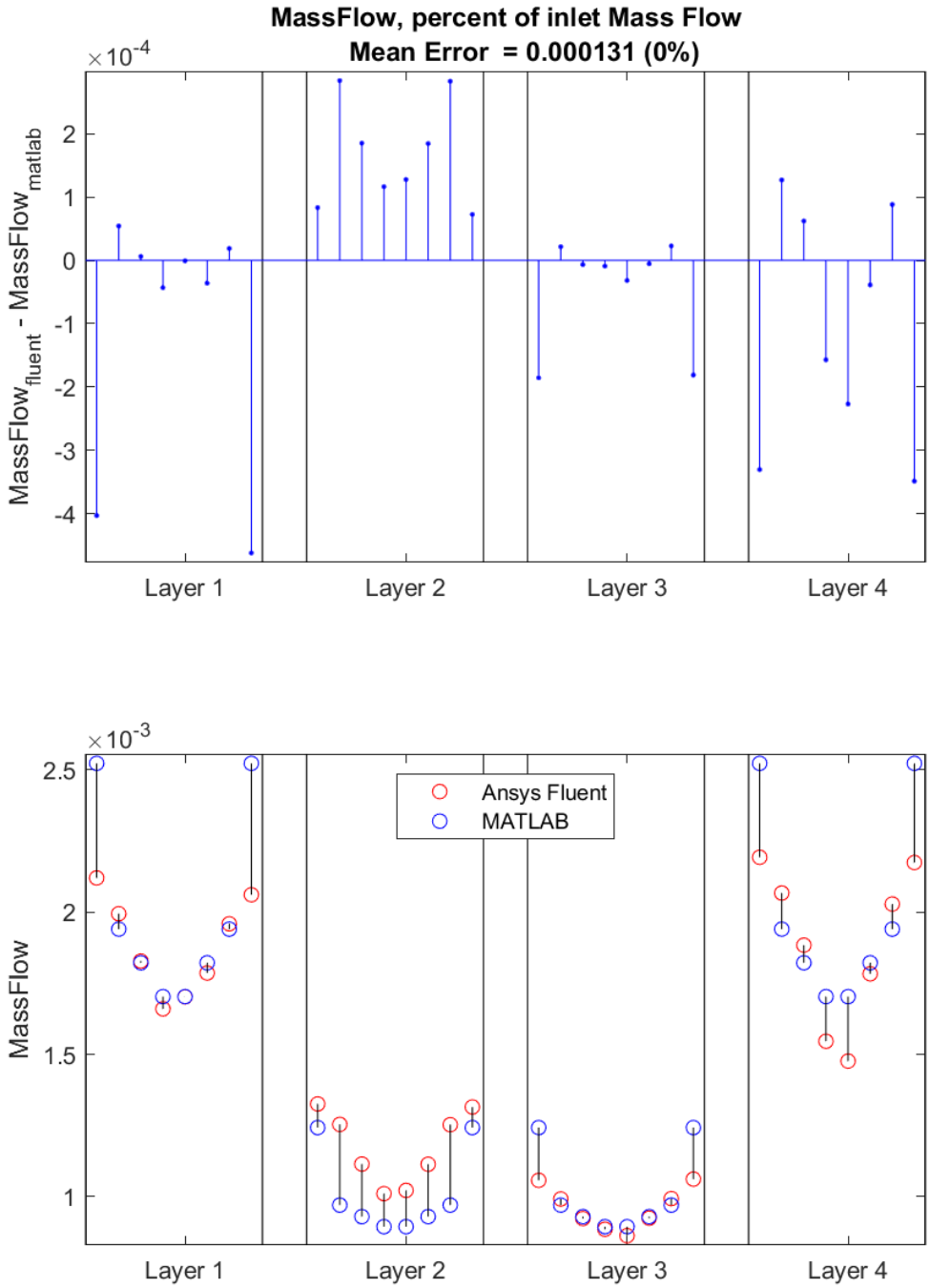

Figure A.11: Mass Flow Error Plots for case 12

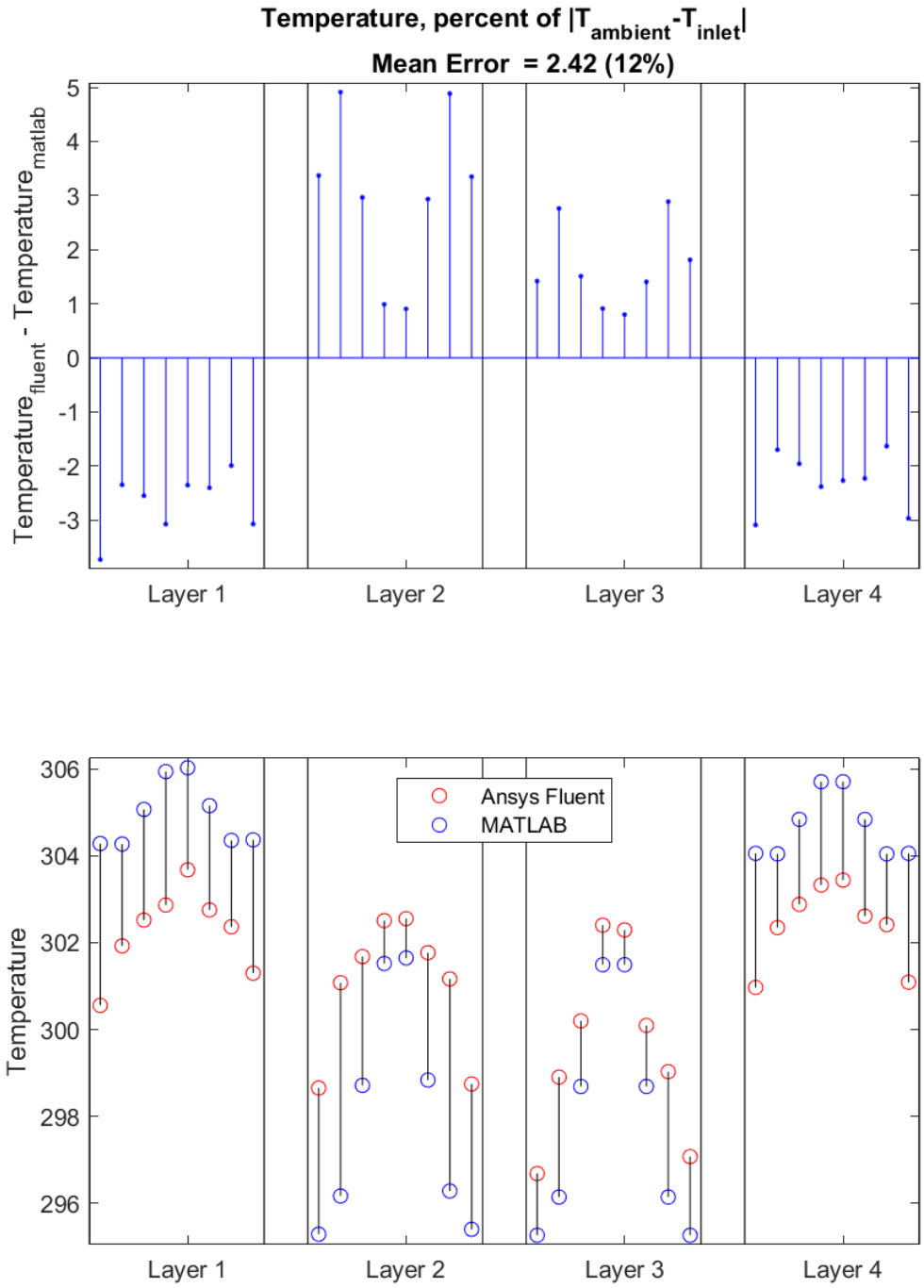

Figure A.12: Temperature Error Plots for case 12

A.1.2 Single layer geometry

A.1.2.1 Case 1

Figure A.13-A.15 presents the error calculations for mass flow, temperature and pressure for case 1 for the single layer geometry, a medium velocity cooling case without active heat sources. The flow error is noted as being present primarily at the first and third box in each arm, indicating a differing flow distribution, albeit a small one. A small asymmetry is also noted between the two arms, arising from the ANSYS FLUENT solution. The temperature error for this case mirrors roughly a negative flow error, suggesting a correlation. The pressure error is likewise omitted following this figure.

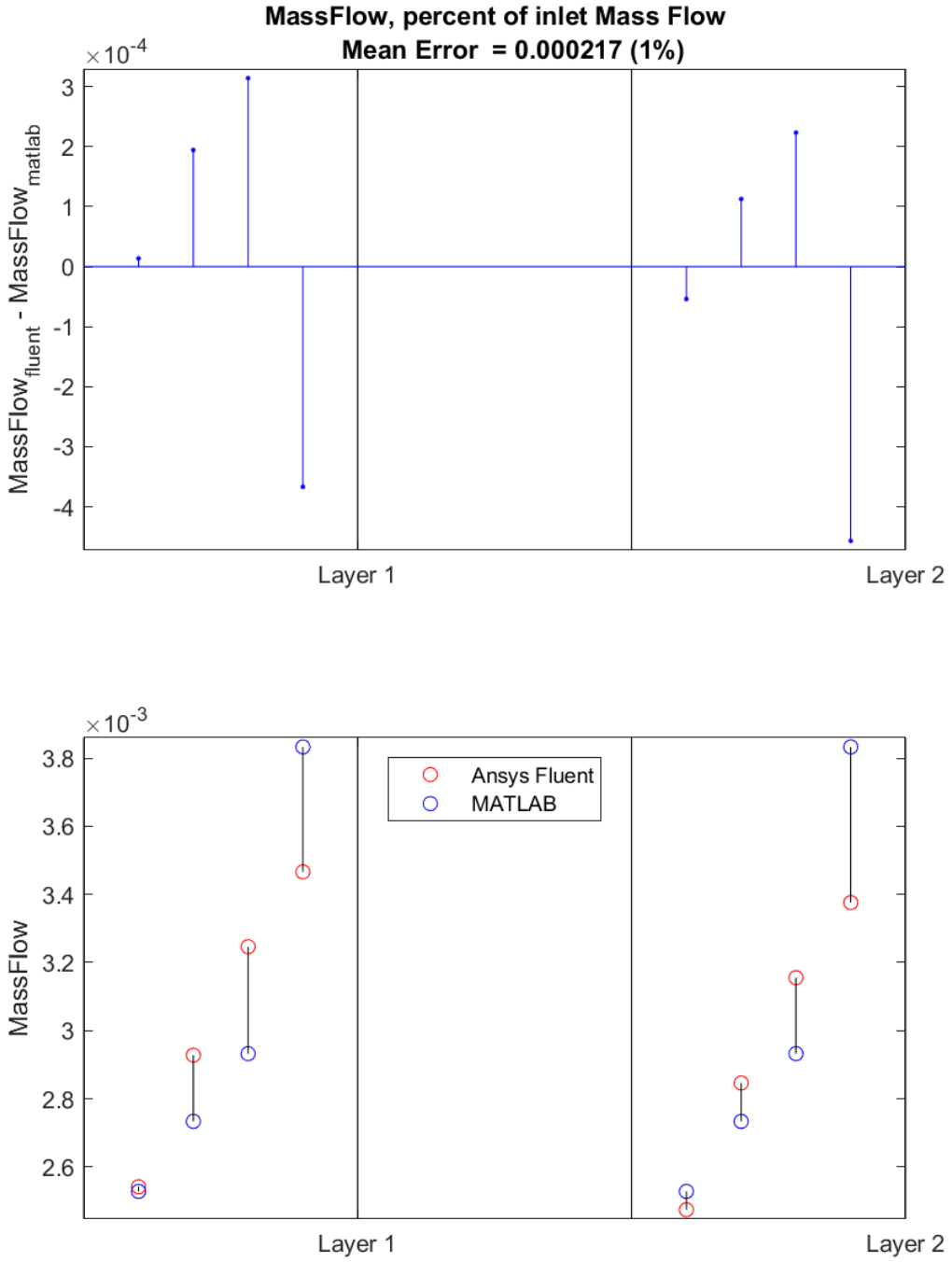

Figure A.13: Mass Flow Error Plots for case 1

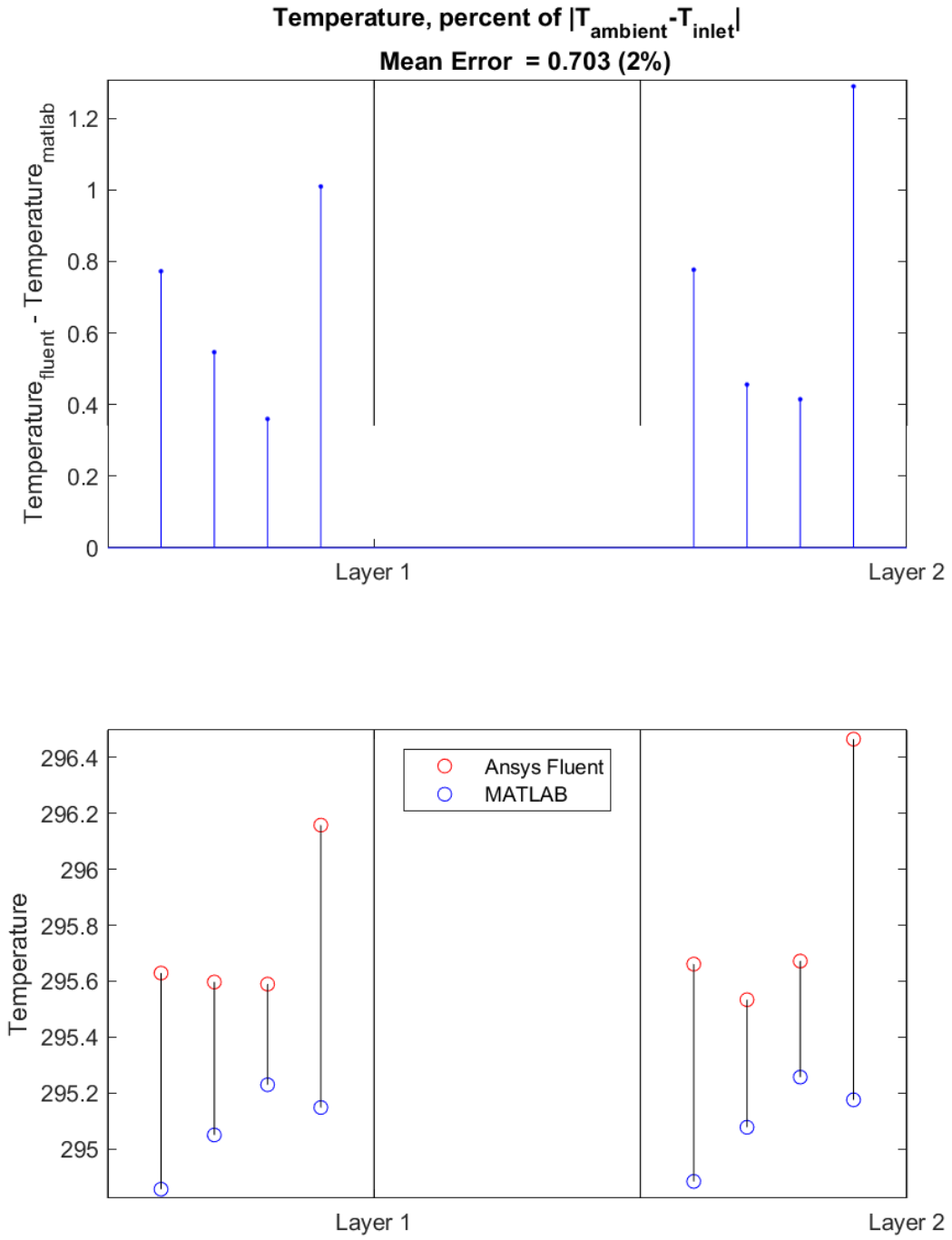

Figure A.14: Temperature Error Plots for case 1

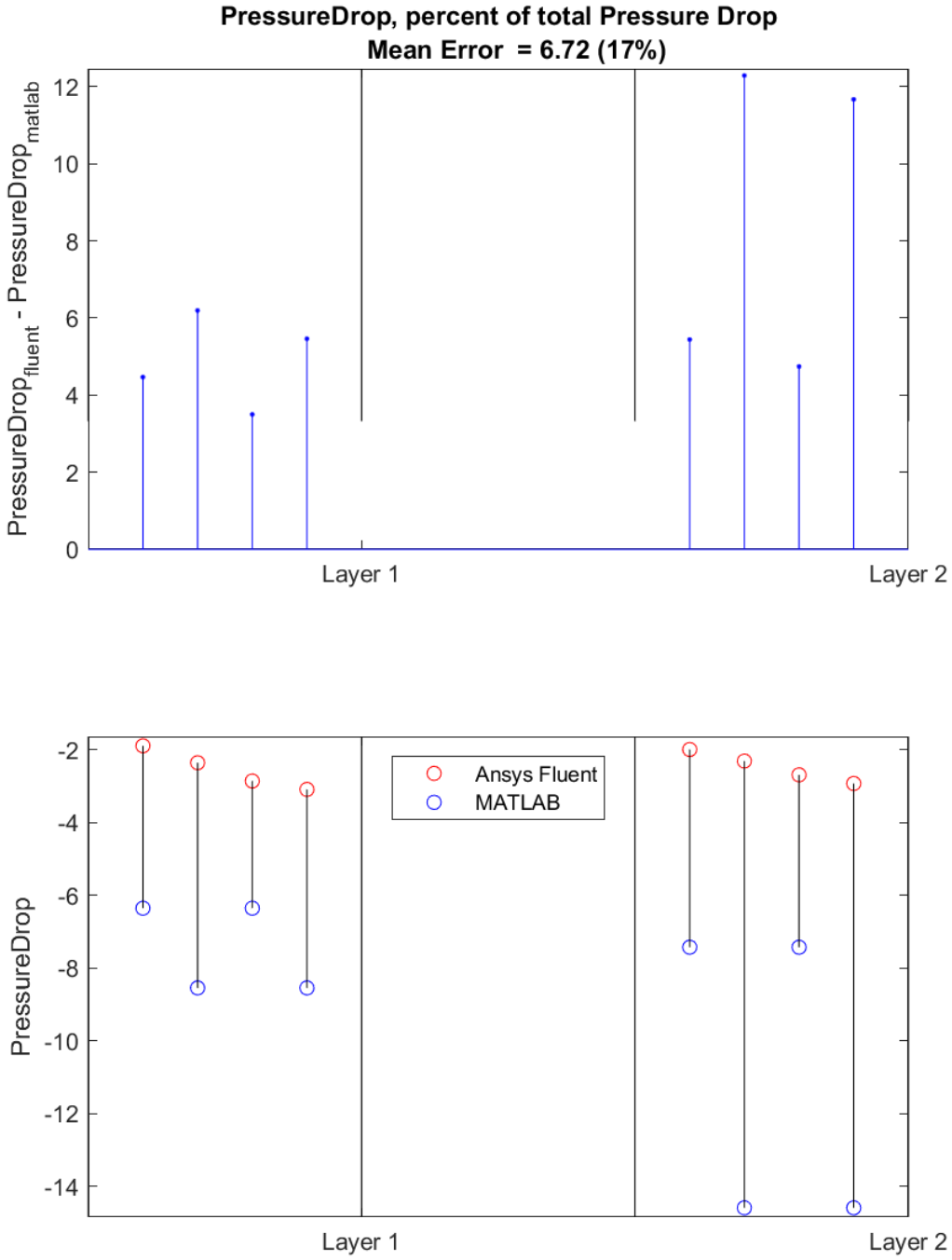

Figure A.15: Pressure Error Plots for case 1

A.1.2.2 Case 2

Figure A.16-A.17 presents the error calculations for mass flow, temperature and pressure for case 2 for the single layer geometry, a medium velocity heating case

without active heat sources. The temperature error is here instead positively correlated with the flow error, albeit with notable exceptions at the end of each arm.

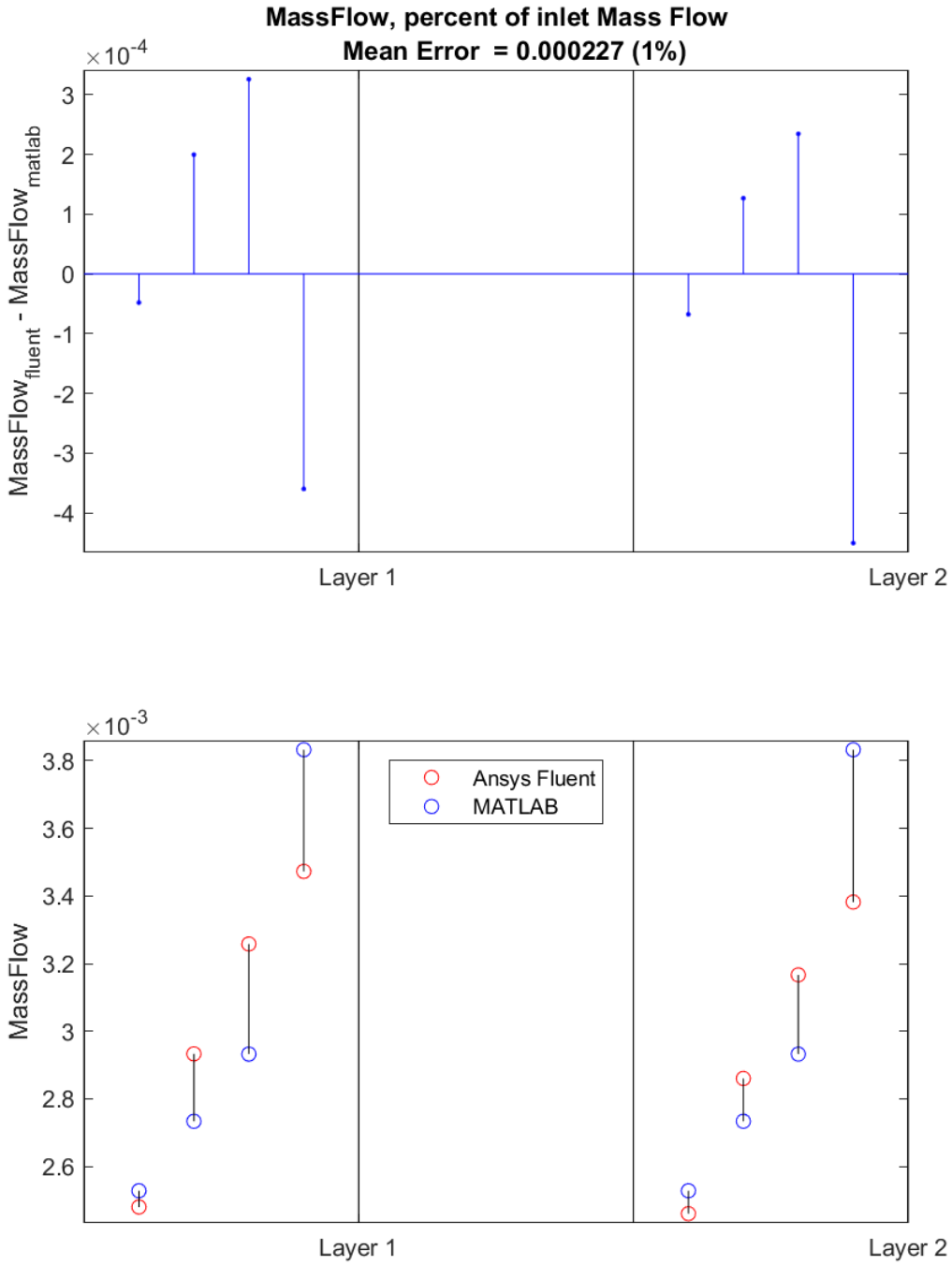

Figure A.16: Mass Flow Error Plots for case 2

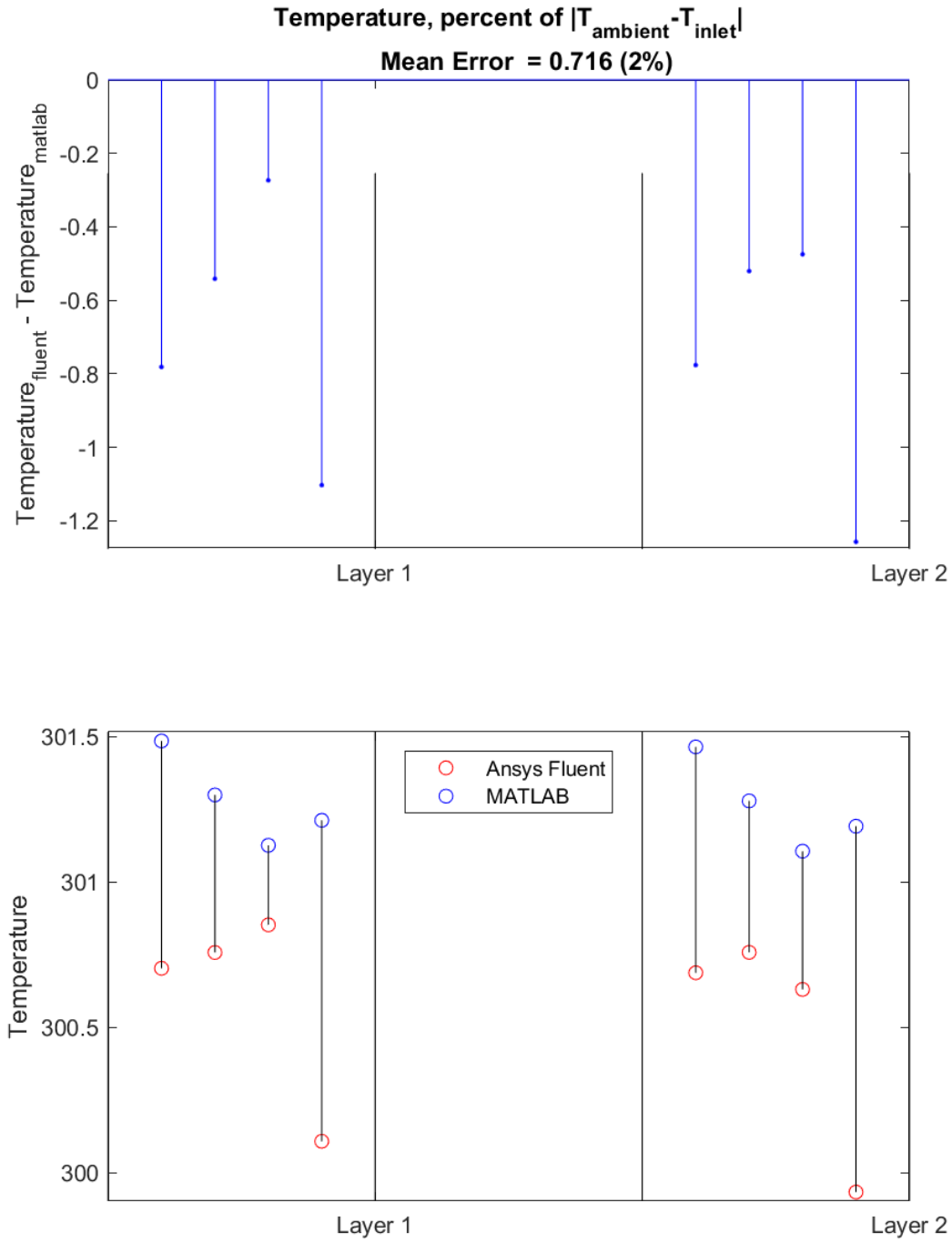

Figure A.17: Temperature Error Plots for case 2

A.1.2.3 Case 3

Figure A.18-A.19 presents the error calculations for mass flow, temperature and pressure for case 3 for the single layer geometry, a high velocity heating case without

active heat sources. Compared to case 2, the temperature error at the last box of each arm correlates more notably with the flow error, suggesting multiple sources of error. Pressure error, like in the multiple layer cases, rises by a factor 4 compared to case 1 and 2 when the velocity doubles.

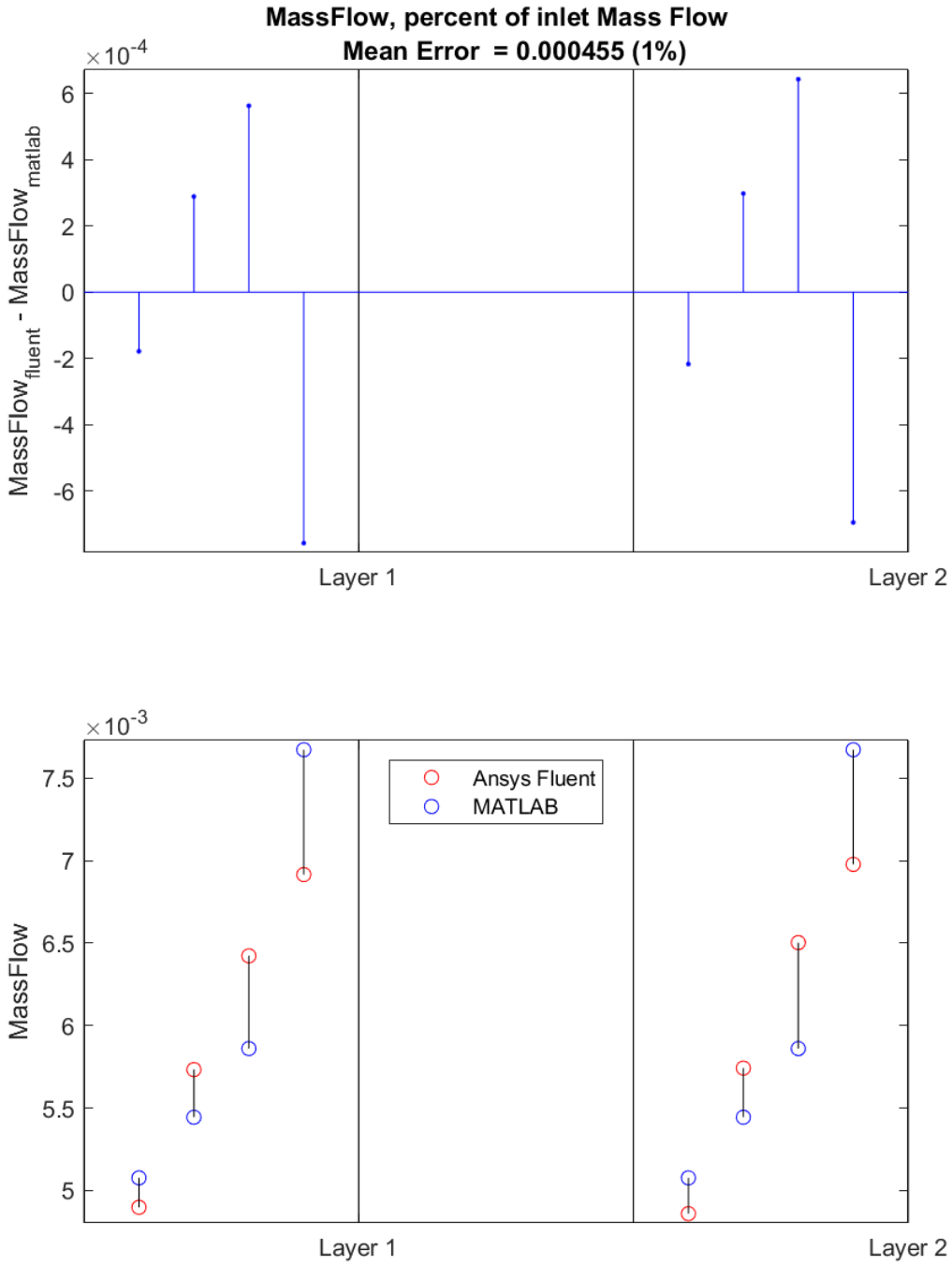

Figure A.18: Mass Flow Error Plots for case 3

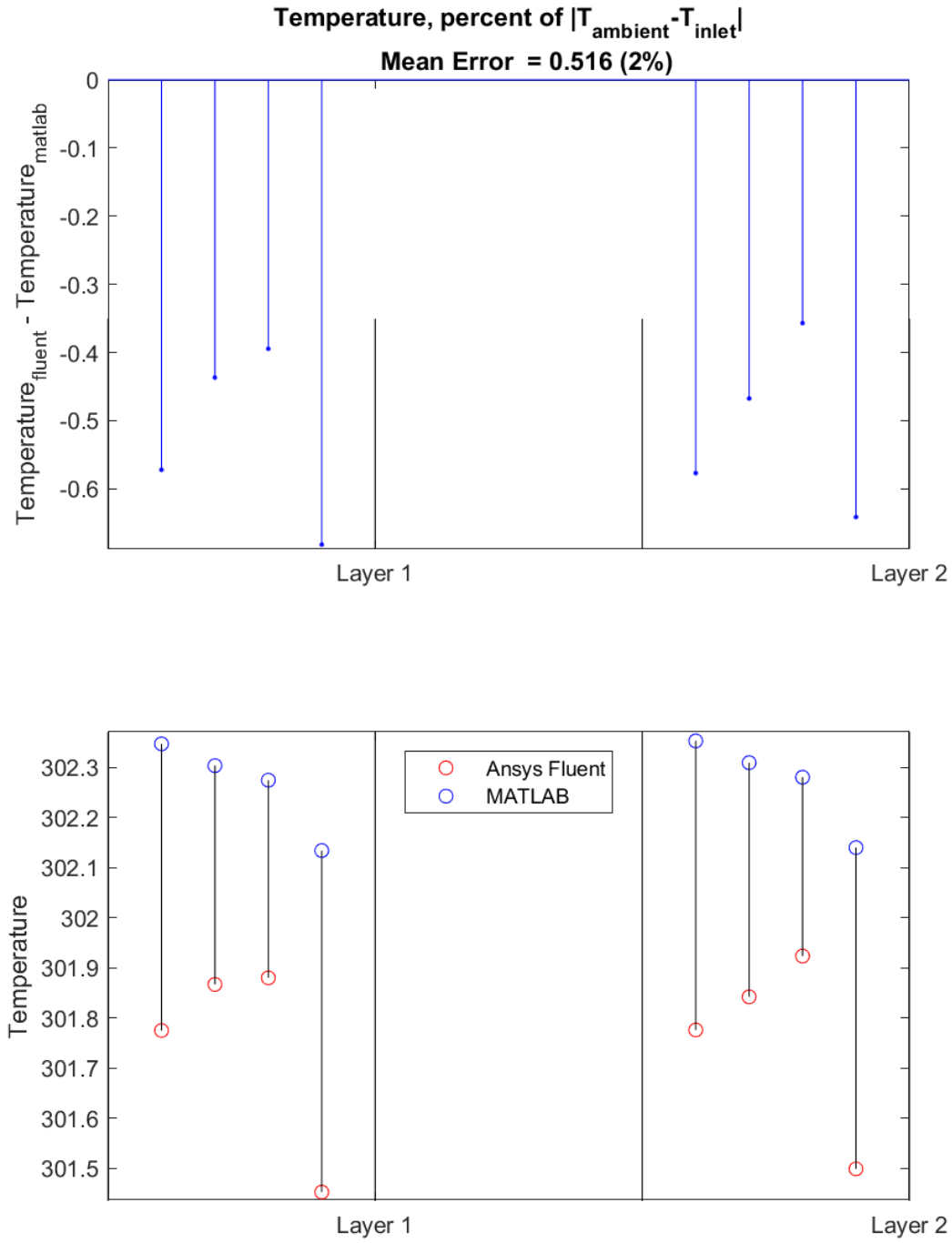

Figure A.19: Temperature Error Plots for case 3

A.1.2.4 Case 5

Figure A.20-A.21 presents the error calculations for mass flow, temperature and pressure for case 5 for the single layer geometry, a medium velocity heating case

with higher heat differential and without active heat sources. Although similar in structure to case 2 for the single layer except doubling in magnitude in response to doubled heat differential, it displays a notable asymmetry between the two arms.

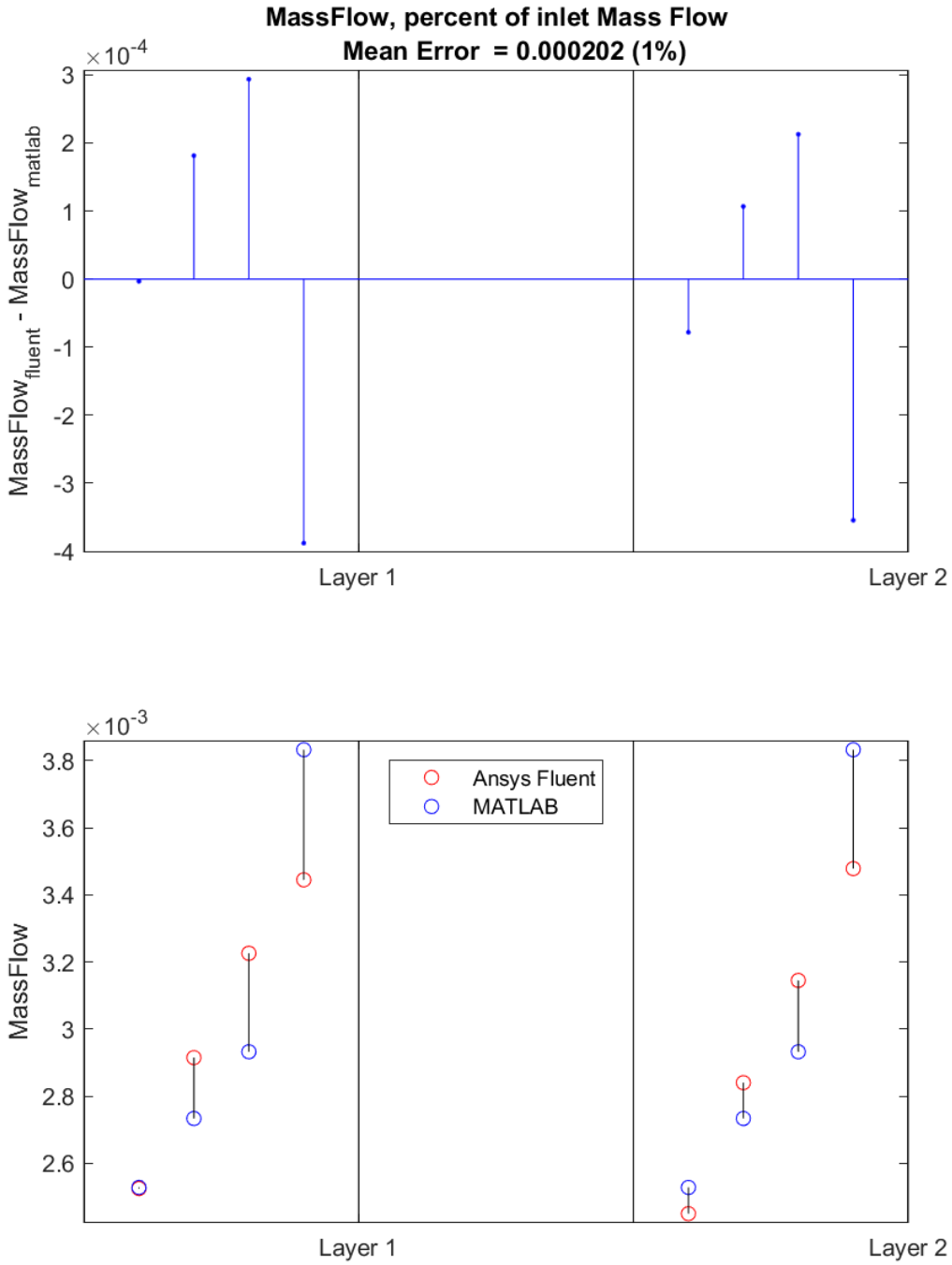

Figure A.20: Mass Flow Error Plots for case 5

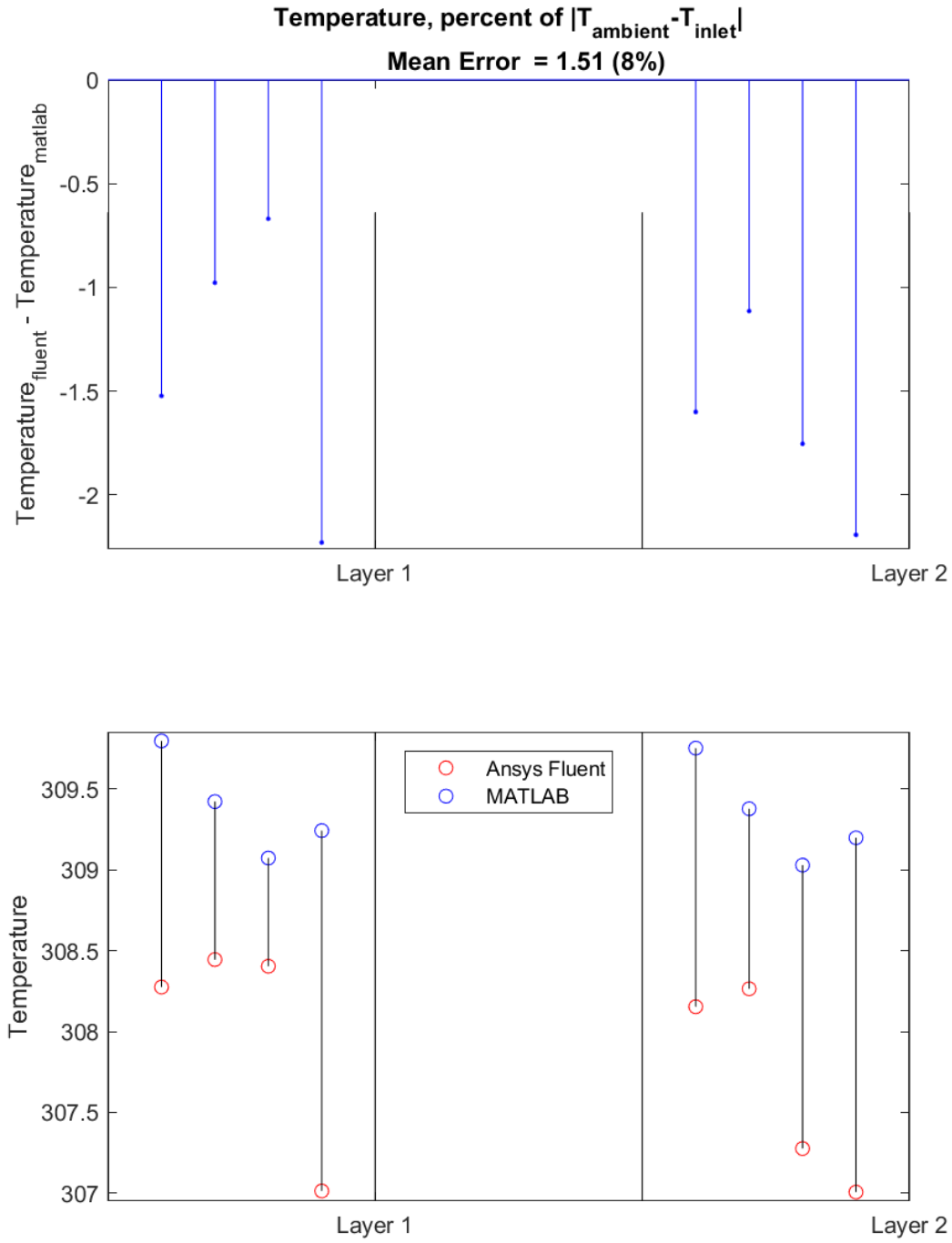

Figure A.21: Temperature Error Plots for case 5

DEPARTMENT OF MATHEMATICAL SCIENCES
CHALMERS UNIVERSITY OF TECHNOLOGY
Gothenburg, Sweden
www.chalmers.se

CHALMERS
UNIVERSITY OF TECHNOLOGY